Studies on Fundamental and Novel Functional Aspects of Metal Nanoparticles

Nabika, Hideki

(Degree)
博士（理学）

(Date of Degree)
2004-09-17

(Date of Publication)
2014-10-02

(Resource Type)
doctoral thesis

(Report Number)
乙2772

(URL)
https://hdl.handle.net/20.500.14094/D2002772

博 士 論 文

Studies on Fundamental and Novel Functional Aspects of Metal Nanoparticles

金属ナノ粒子の基礎物性および機能的特性発現に関する研究

平成 16 年 8 月

並河　英紀

(Hideki NABIKA)

博 士 論 文

Studies on Fundamental and Novel Functional Aspects of Metal Nanoparticles

金属ナノ粒子の基礎物性および機能的特性発現に関する研究

平成 16 年 8 月

Contents

Chapter 1

General Introduction

1.1 overview of nanoparticles

Interest in the research fields concerning science and technology of nanoparticle is steadily and rapidly increasing in the past decade. The term of "nanoparticle" is used for describing any kind of matter with the size of in between a few and a few hundreds nanometer, First of all, it is interesting to show one example demonstrating the growing interest in the fields of "nanoparticle" from 1977, the year I was born, to 2003 (Figure 1) [1]. Note that the number includes all articvles concerning any kinds of nanoparticles. Despite the reputation of metal nanoparticle should go back to the Middle Age or more strictly to 4th or 5th century [2], the number of papers has remarkably increased since 1990. As we will discuss later, nanoparticles possess vast potential to exhibit diverse kinds of novel characteristics that is valuable for future technologies, and this aspect has been stimulating the activity in research field concerning nanoparticles. On the other hand, we have to bear in mind that the development in analyzing tools that give us sufficient information on nanoscopic materials and in synthesis strategies to yield nanoparticles with well-defined size, shape, and composition, are also essential to bring out the best of their potential.

High-resolutional transmission electron microscope (HR-TEM) is one of powerful tools to "see" the structure of nanoparticles directly, and has yielded several precious structural information with atomic resolution. Gai et al. revealed that the (110) faces of chemically prepared rod-like gold nanoparticles (nanorods) is not atomically flat due to the presence of twin defects, and highly unstable (110) surface is stabilized by stabilizing agent [3]. These findings give us new insight into the growth mechanism of such non-spherical nanoparticles, and have important implications in the applications of nanorods in nanoelectronics and molecular electronics.

Combining HR-TEM and STM (scanning tunneling microscopy) provided information on prospective model of geometric features of metal nanoparticles stabilized by tetraalkylammonium salts [4]. In this method, the thickness of the protecting surfactant layer is determined by the difference between the mean diameter measured by STM and that obtained by TEM. The geometric difference (d_{STM}-d_{TEM}, d: observed diameter) was found to be independent on the diameter of core metal nanoparticles, whereas it was almost linearly dependent on the length of alkyl chain. These results strongly suggest that metal nanoparticles are surrounded and stabilized by the monomolecular layer of surfactant, and also that the combination of STM and HR-TEM are capable of yielding valuable information regarding geometric characteristics of nanoparticles

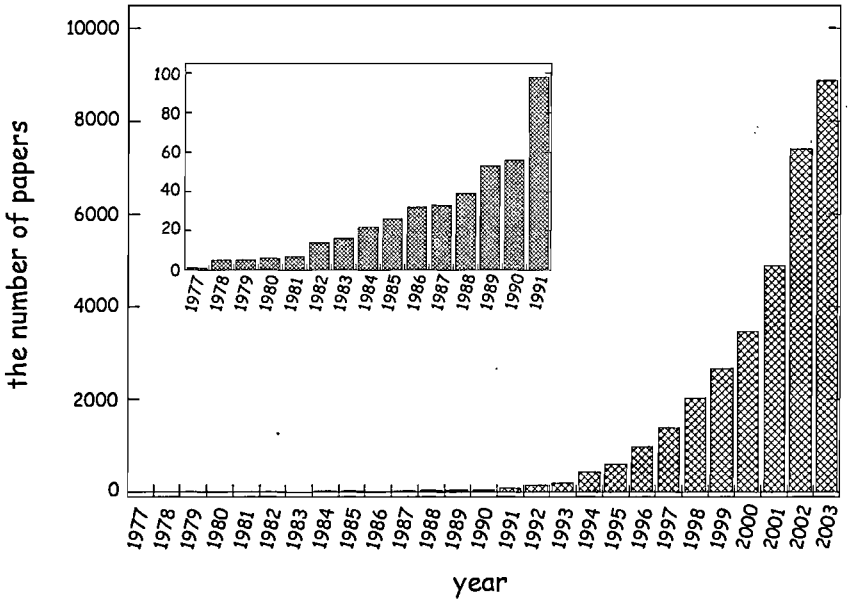

Figure 1. The annual numbers of research articles concerning "nanoparticle". A citation database service, "SciFinder Scholar", provided by Chemical Abstracts Service (CAS), was used for search through the key words of 'nanoparticle'.

coated with organic molecules that is not visible under TEM observation.

Other example that has been revealed by in-situ HR-TEM observation is "simultaneous alloying" behavior observed for several binary system such as Au-Cu [5], Au-Sn [6,7], and (Au, Cu, Al)-Sb [8-10], by which extremely rapid spontaneous dissolution takes place when solute atoms are evaporated onto pre-formed nanoparticles. This phenomenon is interpreted based on melting point depression that is characteristic for nanoscopic materials. Lowering in the melting point with decreasing particle size is thought to be due to the increase in the atomic fraction of surface atom with higher mobility (see also 1.4.2).

Besides high-resolutional imaging tools, high-sensitive spectroscopic system is also attractive to get insight into optical properties of "single" nanoparticle. With conventional optical devices targeting colloidal solutions or composite films containing large number of nanoparticles, we can get only an averaged feature of all nanoparticles present in the system. Recently, optical scattering spectra were acquired for single nanoparticle or single coupled nanoparticles [11-13], by combining optical trapping or total internal reflection microscopy with single photon counting device. As will be discussed later, because optical properties of nanoparticles are critically dependent on the particle size, shape, composition, and interparticle distance, it is the best way to investigate targeting single nanoparticle in order to know precise information on them. And the exact information concerning single nanoparticle makes it more accurate to compare between experimentally observed

results and theoretically obtained features.

In addition to the development in characterizing tools, improvement in sample preparation process has also been stimulating the research activity. There are dominantly two important factors to be controlled; size and shape, and many fabrication methods are reported such as citrate reduction [14-16], two-phase chemical reduction [17-19], reverse micelle method [20-25], seeding growth method [26-31], or sonochemical method [32-36]. Amongst of them, extended two-phase method is suitable to produce metal nanoparticles with well-defined size [19], and seeding growth method is capable of giving us non-spherical nanoparticles such as rod- [26,28] or disk-like [29] nanoparticles. Furthermore, binary nanoparticles are synthesizable by seed-growth, reverse micelle, or sonochemical method (see Table 1). Bimetallic nanoparticles are being investigated with great attention due to their possibility to exhibit unique physicochemical characteristics different from either of the constituent materials. Concerning catalytic activity, distinct ensemble effect has been evident for bimetallic alloy nanoparticles, e.g., hydrogenation of cycloocta-1,3-diene by Pd/Pt [51,52], hydrogenation of nitrobenzene by Ni/Pd [53], and visible-light induced hydrogen evolution by Au/Pt nanoparticles [54].

Constructs of binary semiconductor nanoparticle are also of topical interest. So far, several types of semiconductor nanoparticles with core-shell geometry have been synthesized and characterized concerning mainly on their emission properties. In general, semiconductor with wider band gap is used for shell material, and this wider bang gap shell serves as a passivation against the nonradiative recombination of electron-hole pair at the core surface. Resulting core-shell semiconductor nanoparticles demonstrate photoluminescence with higher quantum efficiency than that of bare semiconductor nanoparticles [45-47]. Reiss et al. prepared CdSe-core (Eg = 1.76 eV) / ZnSe-shell (Eg = 2.72 eV) binary semiconductor nanoparticles with an average diameter of about 4 nm, and obtained significantly high quantum efficiency of > 85 %, which is comparable to organic dye [46]. In addition, the enhancement in photostability has also been observed in such core-shell structure [44].

So far, we saw two important developments that stimulate recent increase in research activity concerning nanoparticles; analyzing tools and synthesis procedure. However, even with these benefits, there should be other importance for researchers to investigate "nanoparticle", and in the following sections, we will have a look on the background, recent findings and future prospects of science and technology of "nanoparticle", putting the emphasis on several topics directly connecting to this thesis.

Table 1. Core-Shell structured nanoparticles: Literature References.

core	shell	diameter / nm core	diameter / nm shell	notes	ref.
metal	***metal***				
Au	Ag	20	80	seed mediated UV-irradiation	30
Au	Pd	6.0/5.0	1.0/1.5	sonochemcial method	36
Au	Pt	3-5		reverse micelle method	24
Ag	Au	9 ± 2	1-7	seed-growth method	31
Co	Pt	4.8	1.8	magnetic property	37
metal	***oxide***				
Au	SiO_2	15	30-90	stöber method	38
Au	TiO_2	30-60	2-3	Au/ZrO_2, Ag/TiO_2, Ag/ZrO_2	39
Ag	TiO_2	10-20	5	hydrolysis of titanium alkoxide	40
Ni	NiO	5-20	2	gas-phase sequential method	41
Sn	SnO_x	7.4		reverse microemulsion	25
Sn	SiO_2	10	1-2	shell: mixture of SiO_2 and SnO_2	42
FePt	Fe_3O_4	4	0.5-3	tunable magnetic property	43
semiconductor	***semiconductor***				
CdSe	CdS	2.1	< 1	photochemical stability	44
CdSe	ZnS	4.5-5.0	< 4 ML	Q.Y.= 66 % (for shell = 1.6 ML)	45
CdSe	ZnSe	3.6	< 3ML	Q.Y.= 85 % (for shell = 2.7 ML)	46
CdTe	ZnS	2.5	1.5-2.5	CdHgTe/ZnS	47
CdSInAs	ZnSsee notes	4.6-7.9	0.3-0.5	in polymeric matrix	48
GaP	GaN	10-100	4-20	also GaN/GaP	49
InAs	see notes	1.2-3.0	< a few ML	InP, GaAs, CdSe, ZnSe, ZnS	50

1.2 Optical properties

1.2.1 Fundamental aspect

The origin that brings pronounced optical properties of metal nanoparticles is the confinement of electrons within nanoscopic space, and the electrons in such constraint cannot behave as if they are in bulk material. In interaction between metal nanoparticles and incident light, electric field of incident light displaces the electrons confined within nanoparticles relative to particle core, resulting in the collective oscillation in electron density at the metal-dielectric interface; this is so-called surface plasmon resonance (SPR). The frequency, with which the electron oscillation and incident electric field resonantly interact, is highly sensitive to particle size, shape, interparticle distance, surrounding medium, and of course the composition.

The relationship between particle size and the optical properties of metal nanoparticles is well explained on the basis of Mie theory. However, limitations are imposed in Mie theory that the particle shape should be sphere and the separation distance should be much larger than the wavelength of the incident light. In contrast, Maxwell-Garnett (MG) theory can take into account non-spherical particles and separation distance well below incident wavelength. Comparison between Mie and MG theories has been done by Foss et al. by using gold cylinder with controlled diameter and aspect ratio, and good agreement was obtained between the observed spectra and Mie theory for spherical particles and MG theory for cylinder particles with the aspect ratio larger than unity [55].

Experimentally, size- and shape-dependences of nanoparticles on the optical properties is detectable even without using any expensive and troublesome instruments; our eyes have enough sensitivity to detect. Some examples to demonstrate the size-dependent optical properties of metal nanorods are shown in Figure 2 (a) and (b). Note that the material that exhibits bright color in each photograph is same (silver for (a) and gold for (b)), and only aspect ratio is different. Other than nanorods, further examples that demonstrate drastic color change with aspect ratio have been reported for nano-disks [22,29], nano-spheroids [55,56], nano-prism [57-60], and nano-pyramids [61,62].

Figure 3 is an example that exhibit different color even with the same material (gold), same size (ca. 3.7 nm), and same shape (sphere); only the difference is the interparticle distance [63]. This phenomenon is explained with respect to the change in local volume fraction (macroscopically) or the change in interparticle distance (microscopically). The averaged optical feature of metal nanoparticles is reasonably predictable by MG theory, in which volume fraction is taken into account. In microscopic treatment, each nanoparticle is often approximated by point dipole, and the decrease in the interparticle distance induces the dipole-dipole interaction between two adjacent nanoparticles, irrespective of attractive or repulsive interactions [64], leading to changes in the

(A)

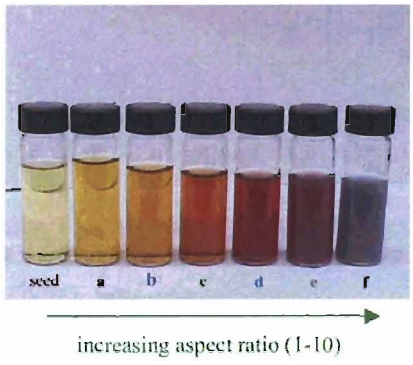

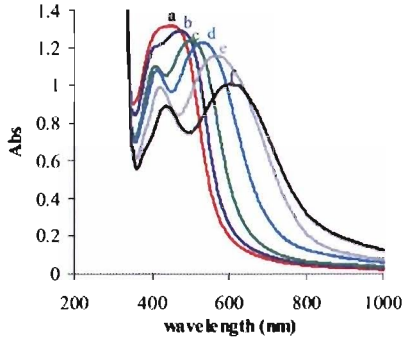

(B)

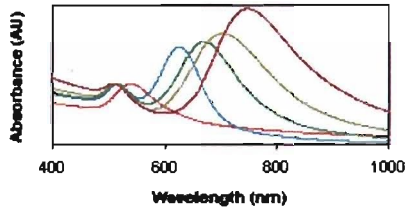

Figure 2. Photographs and optical absorption spectra of silver (A) and gold (B) nano-rod solutions. In both systems, the leftmost solutions are the samples containing only spherical nanoparticles used as seeds in subsequent rod-growth, and the aspect ratio increases from left to right .

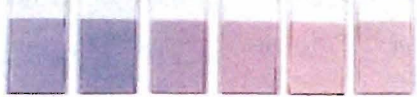

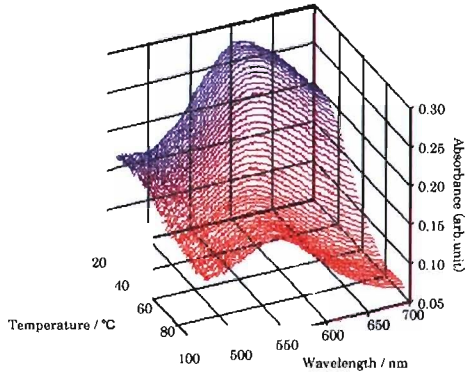

Figure 3. Photograph and optical absorption spectra of gold nanoparticles dispersed in nylon 11 thin films. The leftmost sample is a gold/nylon 11 stacked film, and heat-treatment up to 100 ℃ causes drastic color change from blue to red (from left to right). The heat-treatment is known to induce gradual penetration of gold nanoparticles into nylon 11 layer. The corresponding absorption spectra show that the absorption maximum shifts toward shorter wavelength with increasing heat-treatment temperature.

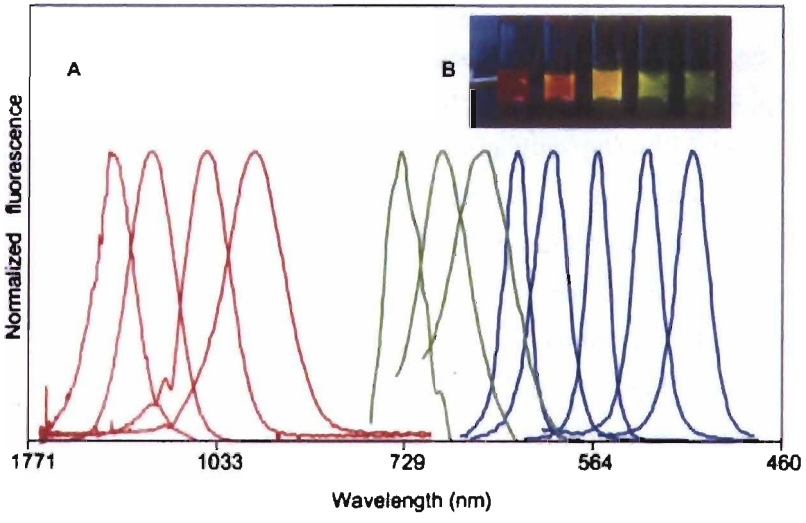

Figure 4. Size- and material-dependent emission spectra of several semiconductor nanoparticles in a variety of sizes. The blue series represents different sizes of CdSe nanoparticles with diameters of 2.1, 2.4, 3.1, 3.6, and 4.6 nm (from right to left). The green series is of InP nanoparticles with diameters of 3.0, 3.5, and 4.6 nm. The red series is of InAs nanoparticles with diameters of 2.8, 3.6, 4.6, and 6.0 nm. (**B**) A true-color image of a series of silica-coated core (CdSe)-shell (ZnS or CdS) nanoparticles probes in aqueous buffer, all illuminated simultaneously with a handheld ultraviolet lamp.[74]

resonant frequency. Both experimental [12,65,66] and theoretical [67-70] treatments support this dipole coupling approximation. Recent researches concerning resonant interaction between two adjacent nanoparticles have been contributing to acquire deeper insight into surface enhancement phenomenon [67,71-73] or optical trapping of single molecule [69].

Besides metal nanoparticles, semiconductor nanoparticles also exhibit drastic changes in optical properties according to their size, shape, and composition (Figure 4) [74-78]. Although the mechanism with which they exhibit different color according to thier size or shape is different from that of metal nanoparticle, the origin is quite similar, i.e., confinement of electrons (and holes) within spatial constraint.

1.2.2 Applications based on optical properties

Several approaches have been proposed to make the best use of optical properties of metal and semiconductor nanoparticles. One typical example is SPR sensor [61,79-83]. Although the shape of metal used for SPR sensor is generally not nanoparticle but thin film, the concept is same and based on the optical properties of low-dimensional system that is highly sensitive to the surrounding refractive index. One of the common SPR geometries is schematically illustrated in Figure 5A. Illumination of metal film (typically gold) through high-refractive-index material (glass) under total internal reflection condition allow for excitation of the surface plasmon via an evanescent wave. To fulfill the coupling condition between wavevectors of the surface plasmon (K_{sp}) and the evanescent field (K_{ev}) for incident light with a given frequency, the incident angle is limited into just one value (θ_{SPR}). Experimentally, this is observed as a dip at θ_{SPR} in a plot of reflectance versus incident angle (Figure 5B). Since K_{sp} is dependent on the refractive index around metal film (n), the resonant angle θ_{SPR} is likewise sensitive to n. On this basis, we can measure the amount of an analyte adsorbed on metal film as shift in θ_{SPR}. Recent development allows us to detect the analyte with a detection limit of sub-pg/mm^2 surface coverage or sub-ng/ml concentration [84,85].

In connection with the fact that the SPR frequency is dependent on the interparticle distance, Mirkin et al. developed elegant strategies toward highly selective colorimetric polynucleotide detection, using gold nanoparticle modified with mercaptoalkyloligonucleotide [86-90]. The concept of their strategies is shown in Figure 6 [89]. With the addition of target single-stranded oligonucleotide, hybridization takes place and induces nanoparticle aggregation. The resulted change in the interparticle distance allows us to detect the presence of analyte (complementary

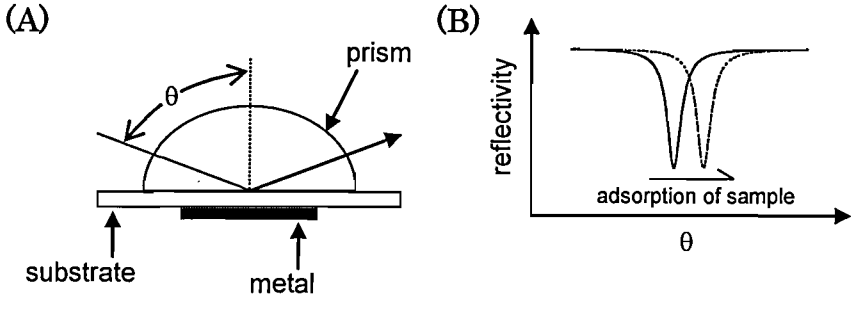

Figure 5. (A) Schematic of a typical SPR geometries and (B) typical responce in the adsorption of analyte onto the metal layer. The shift in the resonant angle indicates the change in refractive index around the metal layer.

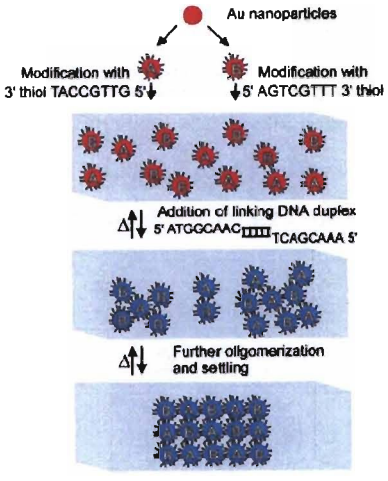

Figure 6. Schematic diagram of Mirkin's strategy. First, two sets of gold nanoparticles protected by noncomplementary oligonucleotide are synthesized separately, and the resultant two gold colloidal solutions are mixed. When the complementary oligonucleotide is added into the mixed solution containing two gold nanoparticles, the hybridization occurs and gold nanoparticles aggregate within the solution, and color of the solution changes due to the change in the interparticle distance. This strategy is recognized as a simple way to detect the presence of the target (i.e., complementary) oligonucleotide. [89]

oligonucleotide) as the changes in color. The most prominent characteristic of this method is that the change in color associated with the presence of target DNA is detectable visually, and this method is capable of detecting about 10 femtomoles of the oligonucleotide.

Final example is optical coding (barcode). The strategy is based on the most principal characteristic of metal and semiconductor nanoparticles; size and material-tunable optical properties. Consider incorporating semiconductor nanoparticles with different size in controlled ratios into polymeric microbeads, each microbeads would display different color, as displayed in

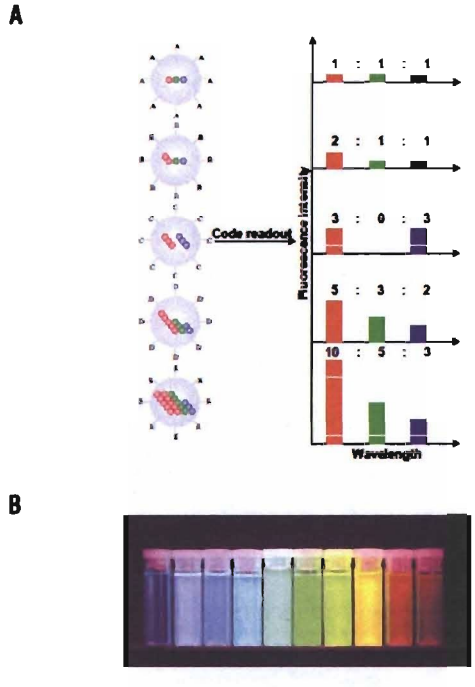

Figure 7. (A) Schematic illustration of optical coding based on wavelength and intensity multiplexing. Large spheres represent polymer microbeads, in which small colored spheres are embedded according to predetermined intensity ratios. Optical readout is accomplished by measuring the fluorescence spectra of single beads. Both absolute intensities and relative intensity ratios at different wavelengths are used for coding purposes; for example (1:1:1) (2:2:2), and (2:1:1) are distinguishable codes. (B) Ten distinguishable emission colors of ZnS-capped CdSe QDs excited with a near-UV lamp. [91]

Figure 7 [91], because semiconductor nanoparticles with different size emit photons with different energy (and thus different emission color) [92,93], as shown in Figure 4. Simple calculation indicates that 3-color/10-intensity combination yields 999 codes, and about one million codes are theoretically available using 6-color/10-intensity combination. Optical coding is also possible with metal nanoparticles, based on the difference in reflectivity at a given wavelength [94]. In addition to the usefulness of nanoparticles with single structure (size, shape, and composition) for biological assay [95], these coding materials have tremendous multiplexing capability in genomics, proteomics, and high-throughput screening.

1.2.3 surface enhancement effect

Since the first experimental observation of surface enhanced Raman scattering (SERS) from pyridine molecules adsorbed on a silver electrode [96], many experimental and theoretical treatments have been carried out to obtain deep insight into fundamental and functional aspects of surface enhancement phenomena. Recent development in the experimental setup has been stimulating the detection of Raman signal from a single molecule, and Nie [97] and Kneipp [98] has independently confirmed the enormously large enhancement factors for single molecule on the order of 10^{14}-10^{15}. By using of high sensitive SERS phenomenon, Mirkin et al. [99] have established multiplexed detection of oligonucleotide with a detection limit of 20 femtomolar. The principal origin for the surface enhancement phenomena is an excitation of surface plasmon and a resultant enhancement in the electric field around metal nanoparticles, and this is known as electromagnetic (EM) effect and a dominant effect to determine the enhancement factor. In addition to EM effect, "chemical effect" or "charge transfer effect", which is not dependent on the EM effect, is occasionally necessary to explain some features observed in single-molecule SERS [100-103], e.g., the enhancement factor over 10^{11} and an intermittent on-off blinking [104-113].

Similar to other optical properties metal nanoparticles, surface enhancement effect is also critically sensitive to the metal size, shape, or composition, and the most important aspect with respect to achieve vast enhancement is the geometry between two adjacent nanoparticles. The effectiveness of aggregations for surface enhancement effect has long been known [114,115] and theoretical information is available in several literatures [108,111,116-118]. One example showing theoretical expectation of the aggregation effect is shown in Figure 8, assuming that two silver nanoparticles with a diameter of 36 nm are placed with 2 nm-separation. In this study, two different incident wavelengths are used for the calculation; 430 nm for dipole excitation and 520 nm for quadrupole excitation, both of which are constructive coupling modes of individual plasmon excitation. Apparently, electric field is enhanced at the gap region between two silver nanoparticles, and the largest fields $|E|^2$ reaches 3500 times and 11 000 times the applied field for quadrupole

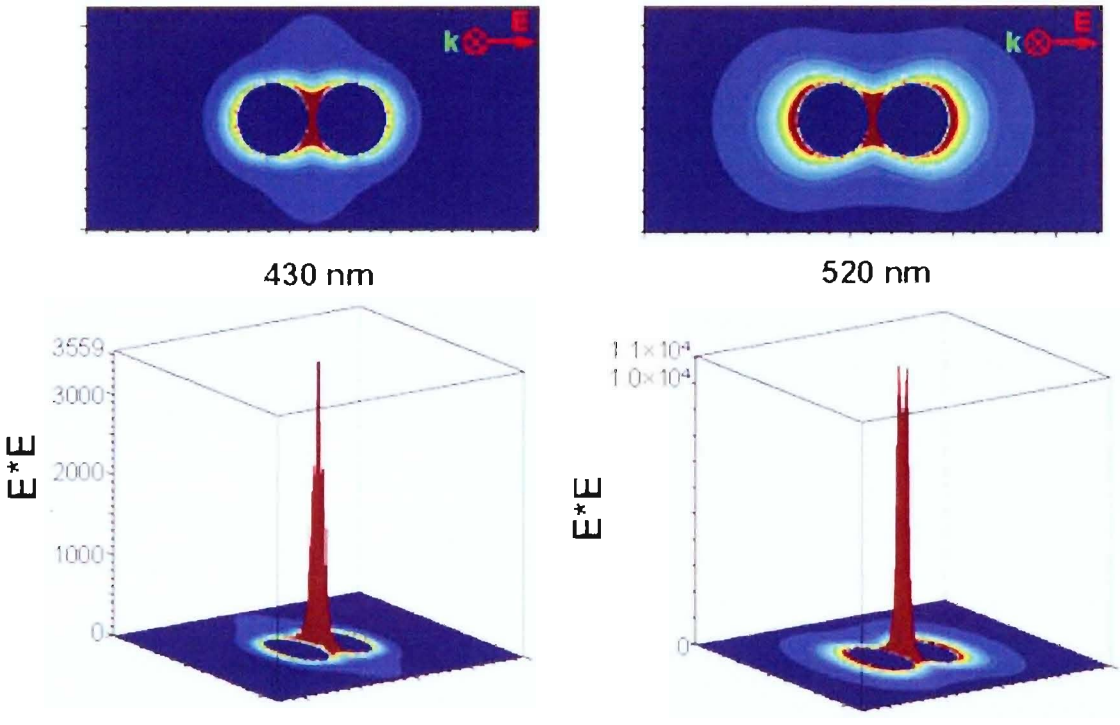

Figure 8. Electric (E) - field enhancement contours external to a dimer of Ag nanoparticles separated by 2 nm, for a plane that is along the inter-particle axis and that passes midway throng the two particles. In the 3D plots, the axis perpendicular to the selected plane represents the amount of E-field enhancement around the dimer. Left: 430 nm. Right: 520 nm. [118]

and dipole excitation, respectively. Note that the SERS enhancement factor increases nearly proportional to the square of the field ($|E|^2$) enhancement (i.e., linear to $|E|^4$), which is descrived as [119-121]

$$I_{SERS} \propto |E(\omega_I)|^2 |E(\omega_S)|^2 \quad (1)$$

where $E(\omega_I)$ and $E(\omega_S)$ are the electric field at the frequencies of incident and scattering light, respectively. This indicates that the Raman intensity would be enhanced by the order of 10^8 for this configuration. Also, non-spherical particles such as rod or spheroid [122-124] and triangle [122,125-127] nanoparticles are capable of several orders of higher enhancement effect compared with the spherical nanoparticles.

As described in equation 1, the enhancement factor for SERS is determined dominantly by the enhancement in the field around metal surface and is not dependent on the molecules if the resonant condition is same for each molecule. On the other hand, surface-enhanced fluorescence (SEF) exhibit strong dependence on the characteristics of the target molecule, and simplified equations that describe the fluorescence intensity in SEF is expressed as [119]

$$ISEF \propto \sigma_F |E(\omega_L)|^2 \frac{\gamma_F |E(\omega_S)|^2}{\gamma_F |E(\omega_S)|^2 + \Gamma_{nr}} \quad (2)$$

where σ_F is the absorption cross section, γ_F and Γ_{nr} is the radiative and nonradiative decay rate of the molecule, respectively. The difference between SERS and SEF is evident from the comparison between equations 1 and 2. When the molecule has high quantum efficiency ($\gamma_F >> \Gamma_{nr}$), the last term concerning the $|E(\omega_S)|$ enhancement in equation 2 does not show any significant enhancement effect. On the other hand, for the molecule with low quantum efficiency ($\gamma_F << \Gamma_{nr}$), the last term effectively increased with the increase in $|E(\omega_S)|$. The dependence of the enhancement in SEF on the molecule quantum efficiency has been experimental demonstrated by Lakowicz et al.[128].

The dependence of the enhancement factor on the characteristics of the target molecule is an essential point to explain fundamental difference between SERS and SEF. In addition, quenching behavior of the metal surface should be taken into account for only SEF, in which the excited energy of the molecule transfers into the metal. In the case of SERS, the maximum enhancement is achieved by directly adsorbing the target molecules onto the metal surface, while fluorescent property is almost completely quenched on the metal surface due to the quenching. Therefore, in the case of SEF, we have to take care the positioning of the target molecules; it is necessary to place them not far but not close to the metal surface. Concerning metal-fluorophore distance, several experimental and theoretical treatments have been reported. In Figure 9, typical relationships between the fluorescence intensity as a function of metal-fluorophore separation are summarized. Curve (a) is theoretically predicted picture by considering dipole-dipole energy transfer (Förster

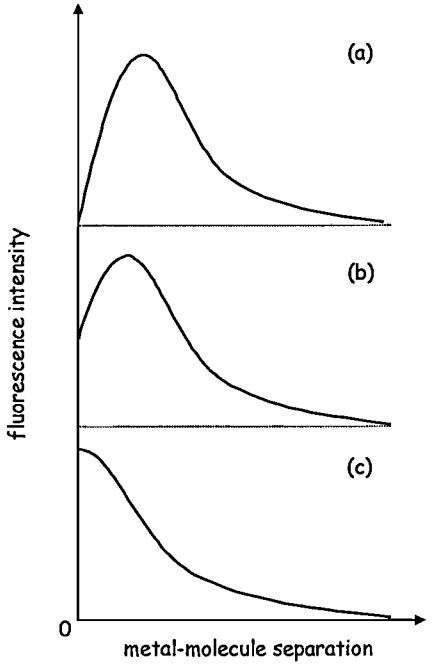

Figure 9. (a) Theoretically expected and (b), (c) experimentally observed curve descriving the relationship between the fluorescent intensity and the metal-molecule separation distance. Non-zero behavior at distance zero observed in curved (b) and (c) is attributable to the presence of the molecules that are adsorbed not on the metal surface but on the substrate that is not covered with metal

transfer) between the molecule and the metal surface, which predict an inverse cubic dependence on the metal-molecule separation; $\hat{b}_{ET} = \beta d^{-3}$, where $\hat{b}_{ET}$ is the energy transfer rate, β is the rate parameter, and d is the separation [129]. According to this relation, excited energy of the molecules that is directly adsorbed on metal surface would be dissipated irrespective of the magnitude of β. The distance at which the enhanced fluorescence reaches the maximum would be determined by the delicate balance between the energy transfer efficiency and the enhanced strength. However, in the practical case, the intensity-distance relation deviates from the theoretically expected one, and the typical curves are shown in Figure 9(b) and (c). The difference from the theoretically expected relationship is that the fluorescence is not completely quenched at the metal surface. These behaviors are observed when the molecules are adsorbed onto the substrate covered with metal island film that is prepared by vapor deposition [130-133] or by adsorbing chemically synthesized metal nanoparticles [134-136]. Non-zero behavior at distance zero is attributable to the presence of the molecules that are adsorbed not on the metal surface but on the substrate that is not covered with metal.

In addition to SERS and SEF, other optical processes are sometimes modulated by the presence of metal nanoparticles on the basis of surface enhancement effect; e.g., IR absorption [137-141], visible light absorption [142-144], intermolecular energy transfer between heteromolecules [145,146] or homomolecules [147,148], and nonlinear optical properties [149].

1.3 Electron transport properties

1.3.1 One- and zero-dimensional system

The fundamental concept of ultimate miniaturization in electronics is to manipulate "single" electron, and this would be realized by metallic architectures with nanoscopic dimension. Possible minimum constituents to achieve single electron transport are one-dimensional nanowire (e.g., Au [150-154], Ag [153-155], Cu [153,154], Pt [152,154]) and zero-dimensional nanoparticles (e.g., Au [156-167], Pd [164,168-171], Al [172], Fe [173], Co [174-176]).

In one-dimensional nanowire, the conductance G is provided from Landauer equation (eq. 3), and the net conductance is determined by the number of transport channel:

$$G = \frac{e^2}{h}\left(\sum_{i=1}^{N_\uparrow} T_{i\uparrow} + \sum_{i=1}^{N_\downarrow} T_{i\downarrow}\right) \tag{3}$$

where $T_{i\uparrow}$ and $T_{i\downarrow}$ are the transmission probability for the i^{th} channel for spin-up and spin-down

electrons, respectively. Note that for diamagnetic nanowire, transmission probability for both spin-up and spin-down electron is same due to the spin degeneration, resulting in that the conductance is quantized in units of $2e^2/h$.

Different from one-dimensional system, quantized electron transport is achieved by electron tunneling for zero-dimensional nanoparticle system. In order to achieve quantized electron transport in zero-dimensional system, the energy to charge the nanoparticle with a single electron, E_c, should be smaller than thermal energy kT (~ 26 meV at 300 K). E_c is charging energy and is provided by $e/2C$, where e is electron charge and C is nanoparticle capacitance. Tunneling probability is strongly suppressed when the bias voltage and thermal fluctuation energy are lower than E_c, and this is so-called Coulomb blockade. Likewise the size-dependent optical properties of metal nanoparticles, E_c is also sensitive to the nanoparticle diameter [157,162-164,166,176], and single electron transport phenomenon is observable even at room temperature with enough small nanoparticles (i.e., enough high E_c) [156,159,163,177,178]. Typical example demonstrating room temperature single electron tunneling (SET) and the corresponding experimental setup are shown in Figure 10. In this setup, Au nanoparticle (~ 500 atoms) was rigidly attached to the dithiol SAM in order for reproducible addressing of STM tip onto the same nanoparticle. In the semiclassical model of Coulomb blockade, two tunnel junctions are coupled in series, and each

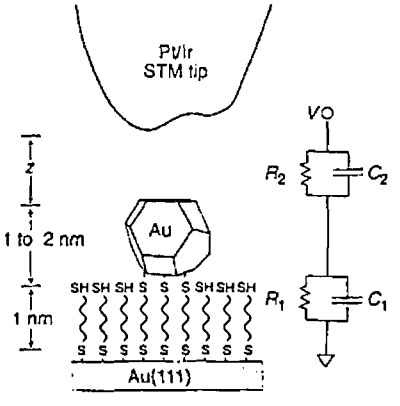

Figure 10. Dithiol SAM on Au(111) substrate with an individual crystalline Au cluster tethered to the surface of the SAM. This self-assembles nano-structure allows the measurement of I(V) data by an STM tip. The equivalent circuit can be represented in terms of a pair of tunnel capacitors (R1, C,; R2, C2) in series.[ref]

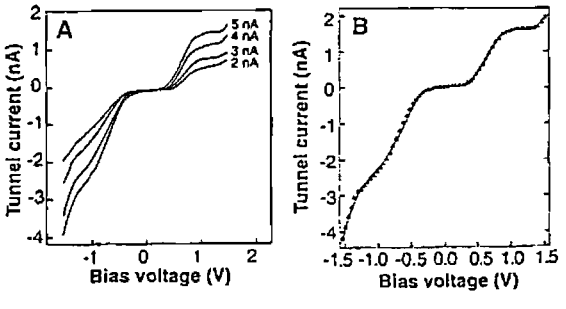

Figure 11. (A) Plot of I(V) data for a tethered 1.8 nm Au cluster obtained in Figure 10, exhibiting Coulomb staircase behavior. The I(V) curves were taken with a bias voltage set point of -1.75V and tunnel current set point of 2, 3, 4, and 5 nA. Each of the I(V) curves is an average of 100 individual voltage sweeps. (B) A typical comparison between the least squares fit from the semiclassical model of Coulomb blockade and I(V) data. [ref]

junction (capacitors) has a capacitance and effective resistance [179,180]. As clearly seen in Figure 11, Coulomb blockade and quantized electron transport (Coulomb staircase) was observed even measured at room temperature. A least square fitting yielded well-fitted curve, suggesting the effectiveness of semiclassical model for the present system.

1.3.2 Three-dimensional system

Next situation is a system consisting of a number of nanoparticles three dimensionally dispersed in insulating dielectrics such as polymer or metal oxide, in which electron transport phenomenon is rather different from the system containing single nanoparticle. The temperature dependence of electrical conductivity for such system is often characterized as

$$\sigma \sim \exp\left(-b/T^{\alpha}\right) \tag{4}$$

where σ is the conductivity and T is the temperature. The value of $\alpha = 1/4$ has been predicted by Mott using a model of hopping conductance for semiconducting glass [181,182], whereas $\alpha = 1/2$ has been observed for the system of metal nanoparticles and rationalized theoretically by taking into account both thermal fluctuation and charging energy [183,184]. Assuming that the number of thermally activated carrier follows Boltzmann distribution, the temperature dependence of electron tunneling is expressed as [184]

$$\sigma = \sigma_0 \exp\left(-2\sqrt{\frac{C}{k_B T}}\right) \tag{5}$$

where C is the tunneling activation energy, k_B Boltzman constant, and T the absolute temperature. For simplification, consider the system of metal nanoparticle with a diameter of d and inter metallic distance s, then the tunneling activation energy and the charging energy is given by

$$C = \chi s E_c, \quad \chi = \sqrt{\frac{2m\phi}{\hbar^2}} \tag{6a, b}$$

$$E_c = \frac{e^2}{d}\left[\frac{2\left(s/d\right)}{\varepsilon\left(1/2 + s/d\right)}\right] \tag{7}$$

where m is electron mass, ϕ is barrier height, and ε is dielectric constant of insulator. χ is a geometric factor that takes into account the fact that tunneling occurs across non-planar barriers and is unity for a planar barrier of uniform thickness. Each parameter is available by fitting the experimental data with equations (5)-(7) [183-185].

1.4 Other characteristics

1.4.1 Catalytic activity

In this section, we will see versatile catalytic activity of metal nanoparticles, putting our interest on gold nanoparticles supported on metal oxides or hydroxides. Despite that gold has long been regarded to be chemically inactive, vigorous investigation was stimulated by the findings of their catalytic activity for selective hydrogenation of 1,3-butadiene [186,187]. A handful of example that demonstrate the catalytic activity of metal oxide-supported gold nanoparticles are listed in Table 2, concerning CO oxidation, hydrogenation and oxidation reactions.

Now, what is the role of metal oxides? One straightforward answer is that they act as stabilizer for metal nanoparticles; otherwise they will aggregate and possibly coalesce during reaction or pre-treatment such as heating. However, more essential and critical role was suggested by Haruta et al [211,212]. They compared three catalysts consisting of gold nanoparticles and TiO_2 support prepared by different method; one is deposision-precipitation (DP) method that gives hemispherical metal nanoparticles with their flat plane strongly attached to the oxide support (Figure 12A), and the others is photodeposition (PD) and impregnation (IMP) methods, both of which yield spherical nanoparticles simply loaded on the support (Figure 12B) [211]. The catalytic activity for CO oxidation was examined for each catalyst and found that DP method gave the highest catalytic activity. On the other hand, the activity of Pt/TiO_2 catalyst toward CO oxidation was independent of the preparation method. They attributed this difference to the difference in the reaction site.

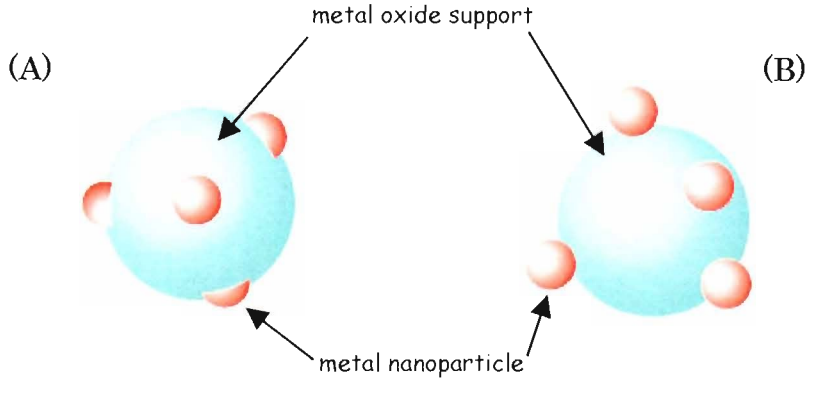

Figure 12. Geometries of metal nanoparticles/metal oxide catalysts prepared by (A) deposition-precipitation (DP) and (B) photodeposition (PD) or impregnation (IMP) methods. DP method gives hemispherical metal nanoparticles with their flat plane strongly attached to the oxide support, whereas PD and IMP methods yield spherical nanoparticles simply loaded on the support.

Table 2. Reactions catalized by supported gold nanoparticle.

reaction	support	diam.[a)]	temp.[b)]	notes	ref.
CO oxidation	TiO_2, Al_2O_3, SiO_2	3.0-8.2	200-450	effect of moisture	188-190
	TiO_2	5-20	250-373	precursor: metal/polymer composite	191
	MnO_x, CeO_x, Fe_2O_3		303-348	stability against CO_2 laser	192
				Au, Ag, Cu, Pd, Ru	
	ZrO_2, ZrO_2-Fe_2O_3	~ 20	250-350	precursor is amorphous alloy	193
	Fe oxides			Mossbauer characterization	194
	FeO, Fe_3O_4, Al_2O_3	3		role of support as O_2 adsorber	195
	carbon, FeO_x-C	2.5-50	303	activation by H_2 or H_2O vapor	196
	Fe_2O_3, FeO_x-SiO_2	4-6		morphology, electronic structure	197,198
	$M(OH)_x$	1-10	200-800	M=Mn, Co, Fe, Ni,	199,200
				Zn, Mg, Cu, Ti, Ce, La	
	activated carbon	2-10	573-773	activation with H_2	201
hydrogenation					
acetylene	Al_2O_3	2-8	523	~ 100 % selectivity to ethylene	202
acrolein	TiO_2, ZrO_2	1-10	453-593	structure, electronic state	203,204
	TiO_2, ZrO_2, SiO_2	1-6	453-593	effect of support for selectivity	205
	Al_2O_3				
1,3-butadiene, crotonaldehyde	TiO_2, Al_2O_3, SiO_2	3-5		effect of support for selectivity	206
oxidation					
benzene	V_2O_5-TiO_2,	5	313/523	$V^{5+} \rightarrow V^{3+}$ transition	207
	V_2O_5-ZrO_2				
ethylene	Al2O3, SiO2		480-540	to CO2, H2O, acetic acid, acetone	208
hydrogen	Al2O3, SiO2, TiO2	2-7	200-700	interface between metal/support	209
stylene	MgO, CaO, SrO, BaO	6-18	353	to stylene oxide (60 % for MgO)	210

a) diameter of gold nanoparticle.

b) reaction temperature

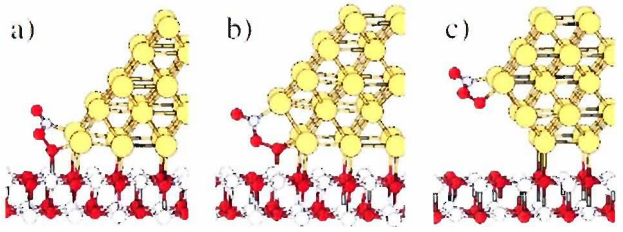

Figure 13. Three different CO - O_2 binding configurations on MgO (100). Yellow dot: Au, red: O, grey: C, white: Mg.

For Au/TiO_2 system, CO and O_2 molecules adsorb on gold and TiO_2 surface, respectively, and they diffuse toward and react at the gold-support interface. This is the reason that the catalyst prepared by DP method exhibited the highest activity, i.e., due to their large gold-support interface as shown in Figure 12A. Whereas CO oxidation proceeds on Pt surface for Pt/TiO_2 catalyst, which can explain that they were not dependent on the preparation method (i.e., independent of interface geometry). From these results, they suggested that strong synergetic effect between gold and support determined their catalytic activity.

Density functional theory (DFT) investigation done by Molina et al. supports this suggestion [213]. They considered the CO oxidation reaction at MgO supported gold nanoparticle with the configuration shown in Figure 13 (same configuration shown in Figure 12A), and found that supporting oxides took an important role in the bonding and activation of adsorbates bound to gold. On interfaces in Figure 13(a) and (b), CO-O_2 intermediate complex exists close to both gold and oxide with a bond strength of about 0.4 eV higher than the bonding of the CO molecule alone to gold surface. On contrary, configuration shown in Figure 13(c) does not give significant effectiveness for stabilization of CO-O_2 intermediate complex. From a result of DFT calculation for the reaction energy needed for CO oxidation including adsorption, formation of CO-O_2 intermediate state, and CO oxidation reaction, they concluded that the high reactivity of supported gold catalyst originates from two effects; (i) oxide support reduce the reaction energy at gold-support interface with any configuration shown in Figure 13, (ii) among of three configuration, configuration Figure 13(b) is the most reactive interface due to higher stabilizing ability for CO-O_2 intermediate complex and lower steric hindrance than in Figure 13(a).

In addition to gold and other noble metal nanoparticles, transition metal is also a promising candidate for potential catalyst for the production of carbon nanotubes. Carbon nanotubes are currently the focus of intense research due to their diverse possible applications such as field

emitters [214], chemical sensors [215], and nanoscopic transistors [216], and the mass production is required to realize these applications. For this purpose, several approaches for the production of single-walled carbon nanotubes (SWNT) have been investigated using transition metal catalysts such as Fe [217,218], Co [219], (Fe or Co)/Mo [220-222], Fe/Ni [223,224], and Ni/Y [225], and have succeeded in size-selective synthesis of SWNT [218,220,226] and double-walled carbon nanotubes (DWNT) [218,221].

1.4.2 Thermodynamic properties

We can refer melting point, crystal structure, lattice constant, or other physical properties of bulk metal on general textbooks or handbooks, e.g., those of bulk gold are 1336.15 K, face centered cubic (fcc), and 4.0785 Å, respectively [227,228]. We do not have a care to apply these parameters in discussing on bulk system. However, when the size of metal is reduced down to nanometer-scale, we must pay attention because they would be changed from those of bulk system. Diverse experimental evidences for the lowering in melting point for several kinds of metal has been reported (see Table 3). Buffat and Borel examined the melting behavior of gold nanoparticles by scanning electron diffraction technique [230]. In their system, the temperature at which the diffraction nature of metal disappears is recognized as the melting point, and they observed that the decrease in melting point became more pronounced with decreasing metal size, and that the melting point decreased down to about 300 K for ~ 2 nm gold nanoparticles. This phenomenon is attributable to the increase in the number fraction of surface atom possessing higher mobility than that of inner atom. Lowering in the melting point, in other word, softening of nanoscopic material sometimes brings about serious problem if one tries to prepare nanostructured material with sharp edge, and one should take care to suppress surface melting by coating rigid material or manipulate at low temperature. Other theoretical and experimental investigations concerning size-dependent thermodynamic properties or crystallographic nature have been investigated by several groups and listed in Table 3.

Table 3. Variable thermodynamical properties with particle diameter.

property	metal
melting point	Au[229,230], Ag[229], Sn[231], In[232,233], Pb[234], Be[235], CdS[236]
heat of fusion	Au[237], In[233]
specific heat	Pd[238], Fe, Co, Ni[239],
lattice constant	Au[240], Ag[241], Cu, Pt[242], CdS[236]
morphology	Au[243], Co[244]

1.5 Aim of the present work

As we saw in this chapter, metal nanoparticles are capable of exhibiting innovative and versatile features attractive for diverse fields of science and technology. The primal aim of the present work is to seek out novel aspect of metal nanoparticles, and the target aspect is the phenomenon or function that has not been realized but has been predicted.

In Part I, a composite cosisting of carbon thin film and gold/cobalt alloy nanoparticles was prepared, and structural and electron transport nature of gold/cobalt alloy nanoparticles were examined. This part starts with the description concerning preparation of carbon thin films embedding metal nanoparticles, using polyacrylonitrile as a carbon precursor (Chapter 2). Metal nanoparticles were deposited by vacuum evaporation on pre-deposited PAN thin film. Structural changes of PAN and the incorporation mechanism of metal nanoparticles into PAN matrix during heat-treatment were investigated with IR, Raman, X-ray photoelectron spectroscopy (XPS), and TEM observation. Heat-treatment of the metal/PAN stacking film induced the carbonization of PAN, and at the same time, the dispersion of metal nanoparticles into PAN matrix, in analogy with the protcol of RAD (relaxative-auto dispersion) process proposed by Deki's group [245-250]. In Chapter 3, crystal structure of gold/cobalt alloy nanoparticles obtained by simultaneous vacuum evaporation method was examined by using of XPS and HR-TEM observation. We will see the formation of anomalous crystal phase in these alloy nanoparticles that has never been observed in bulk gold/cobalt system. In Chapter 4, electron transport properties of gold/cobalt nanoparticles were examined. Emphasis was put on the response in tunneling probability with applied magnetic field, i.e., tunneling magnetoresistance (TMR). Especially high response was achieved for the alloy nanoparticles with the composition of Au:Co=20:80, and exceeded 80 % of TMR at room temperature.

In Part II, optical properties of metal nanoparticles were investigated. Amongst of several optical properties, surface enhancement effect on the fluorescence properties of Europium complex was examined. Chapter 5 describes first the preparation and structural and optical characterization of silver spherical and rod-shaped nanoparticles. By controlling preparation condition, polymer-protected silver nanoparticles with different size and shape were obtained. The effect of an addition of these silver nanoparticles into europium complex solution was investigated by fluorescence spectroscopy. The effect of particle size, shape, and the structure of europium complex was explored. The results clearly demonstrated the importance of the aggregation effect that is already well-known in the field of SERS, and the present work is the first report to provide the insight into the importance of aggregation effect for SEF.

References

[1] A citation database service, "SciFinder Scholar", provided by Chemical Abstracts Service (CAS), was used for search through the key words of 'nanoparticle'.

[2] for short historical review: Daniel, M.-C.; Astruc, D. Chem. Rev. 2004, 104, 293-346 and references therein.

[3] Gai, P. L.; Harmer, M. A. *Nano Lett.* **2002**, *2*, 771-774.

[4] Reetz, M. T.; Helbig, W.; Quaiser, S. A.; Stimming, U.; Breuer, N.; Vogel, R. *Nature* **1995**, *267*, 367-369.

[5] Yasuda, H.; Mori, H.; Komatsu, M.; Takeda, K. *J. Appl. Phys.* **1993**, *73*, 1100-1103.

[6] Yasuda, H.; Mitsuishi, K.; Mori, H. *Phys. Rev. B* **2001**, *64*, 094101.

[7] Mori, H.; Yasuda, H. Mater. *Sci. Eng. A* **2001**, *312*, 99-103.

[8] Yasuda, H.; Mori, H. Mater. *Sci. Eng. A* **1996**, *217/218*, 249-252.

[9] Yasuda, H.; Mori, H. *Thin Solid Films* **1997**, *298*, 143-146.

[10] Mori, H.; Yasuda, H. *Mater. Sci. Eng. A* **1996**, *217/218*, 244-248.

[11] Prikulis, J.; Svedberg, F.; Kall, M.; Enger, J.; Ramser, K.; Goksor, M.; Hanstorp, D. *Nano Lett.* **2004**, *4*, 115-118.

[12] Fromm, D. P.; Sundaramurthy, A.; Schuck, P. J.; Kino, G.; Moerner, W. E. *Nano Lett.* 2004, 4, 957-961.

[13] Tamaru, H.; Kuwata, H.; Miyazaki, H.; Miyano, K. *Appl. Phys. Lett.* **2002**, *80*, 1826-1828.

[14] Frens, G. Nature: *Phys. Sci.* **1973**, *241*. 20-22.

[15] Yonezawa, T.; Sutoh, M.; Kunitake, T. *Chem. Lett.* **1997**, 619-620.

[16] Chow, M. K.; Zukoski, C. F. J. *Colloid Interface Sci.* **1994**, *165*, 97-109.

[17] Brust, M.; Walker, M.; Bethell, D.; Schiffrin, D. J.; Whyman, R. *J. Chem. Soc., Chem. Commun.* **1994**, 801-802.

[18] Kiely, C. J.; Fink, J.; Brust, M.; Bethell, D.; Schiffrin, D. J. *Nature* **1998**, *396*, 444-446.

[19] Shimizu, T.; Teranishi, T.; Hasegawa, S.; Miyake, M.; *J, Phys. Chem. B* **2003**, *107*, 2719-2724.

[20] Wilcoxon, J. P.; Williamson, R. L.; Baughman, R.; *J. Chem. Phys.* **1993**, *98*, 9933-9950.

[21] Sangregorio, C.; Galeotti, M.; Bardi, U.; Baglioni, P. *Langmiur* **1996**, *12*, 5800-5802.

[22] Maillard, M.; Giorgo, S.; Pileni, M. P. *J. Phys. Chem. B* **2003**, *107*, 2466-2470.

[23] Pileni, M. P. *J. Phys. Chem.* **1993**, *97*, 6961-6973.

[24] Wu, M.-L.; Chen, D.-H.; Huang, T.-C. *Chem. Mater.* **2001**, *13*, 599-606.

[25] Wang, Y.; Lee, J. Y.; Deivaraj, T. C. *J. Mater. Chem.* **2004**, *14*, 362-365.

[26] Sun, Y.; Gates, B.; Mayers, B.; Xia, Y. *Nano Lett.* **2002**, *2*, 165-168.

[27] Jana, N. R.; Gearheart, L.; Murphy, C. J. *Chem. Mater.* **2001**, *13*, 2313-2322.

[28] Jana, N. R.; Gearheart, L.; Murphy, C. J. *Chem. Commun.* **2001**, 617-618.

[29] Chen, S.; Carroll, D. L. *Nano Lett.* **2002**, *2*, 1003-1007.

[30] Mallik, K.; Mandal, M.; Pradhan, N.; Pal, T. *Nano Lett.* **2001**, *1*, 319-322.

[31] Sloufova, I.; Lednicky, F.; Gemperle, A.; Gemperlova, J. *Langmuir* **2000**, *16*, 9928-9935.

[32] Nagata, Y.; Watanage, Y.; Fujita, S.; Dohmaru, T.; Taniguchi, S. *J. Chem. Soc., Chem. Commun.* **1992**, 1620-1622.

[33] Yeung, S. A.; Hobson, R.; Biggs, S.; Grieser, F. *J. Chem. Soc., Chem. Commun.* **1993**, 378-379.

[34] Mizukoshi, Y.; Okitsu, K.; Maeda, Y.; Yamamoto, T. A.; Oshima, R.; Nagata, Y. *J. Phys. Chem. B* **1997**, *101*, 7033-7037.

[35] Mizukoshi, Y.; Oshima, R.; Maeda, Y.; Nagata, Y. *Langmuir* **1999**, *15*, 2733-2737.

[36] Mizukoshi, Y.; Fujimoto, T.; Nagata, Y.; Oshima, R.; Maeda, Y. *J. Phys. Chem. B* **2000**, *104*, 6028-6032.

[37] Park, J.-I.; Cheon, *J. J. Am. Chem. Soc.* **2001**, *123*, 5743-5746.

[38] Mine, E.; Yamada, A.; Kobayashi, Y.; Konno, M.; Liz-Marzan, L. M. *J. Colloids Interface Sci.* **2003**, *264*, 385-390.

[39] Tom, R. T.; Nair, A. S.; Singh, N.; Aslasm, M.; Nagendra, C. L.; Philip, R.; Vijayamohanan, K.; Pradeep, T. *Langmuir* **2003**, *19*, 3439-3445.

[40] Santos, I.; Koktysh, D. S.; Mamedov, A. A.; Giersig, M.; Kotov, N. A.; Liz-Marzan, L. M. *Langmuir* **2000**, *16*, 2731-2735.

[41] Sakiyama, K.; Koga, K.; Seto, T.; Hirasawa, M.; Orii, T. *J. Phys. Chem. B* **2004**, *108*, 523-529.

[42] Yang, C.-S.; Liu, Q.; Kauzlarich, M.; Phillips, B. *Chem. Mater.* **2000**, *12*, 983-988.

[43] Zeng, H.; Li, J.; Wang, Z. L.; Liu, J. P. Sun, S. *Nano Lett.* **2004**, *4*, 187-190.

[44] Xu, L.; Wang, L.; Huang, X.; Zhum J.; Chen, H.; Chen, K. *Phys. E* **2000**, *8*, 129-133.

[45] Talapin, D. V.; Rogach, A. L.; Kornowski, A.; Haase, M.; Weller, H. *Nano Lett.* **2001**, *1*, 207-211.

[46] Reiss, P.; Bleuse, J.; Pron, A. *Nano Lett.* **2002**, *2*, 781-784.

[47] Tsay, J. M.; Pflughoefft, M.; Bentolila, L. A.; Weiss, S. *J. Am. Che. Soc.* **2004**, *126*, 1926-1927.

[48] Lu, S.-Y.; Wu, M.-L.; Chen, H.-L. *J. Appl. Phys.* **2003**, *93*, 5789-5793.

[49] Lin, H.-M.; Chen, Y.-L.; Yang, J.; Liu, Y.-C.; Yin, K.-M.; Kai, J.-J.; Chen, F.-R.; Chen, L.-C.; Chen, Y.-F.; Chen, C.-C. *Nano Lett.* **2003**, *3*, 537-541.

[50] Cao, Y. W.; Banin, U. *J. Am. Chem. Soc.* **2000**, *122*, 9692-9702.

[51] Toshima, N.; Kushihashi, K.; Yonezawa, T.; Hirai, H. *Chem. Lett.* **1989**, 1769-1772.

[52] Toshima, N.; Yonezawa, T.; Kushihashi, K. *J. Chem. Soc. Faraday Trans.* **1993**, *89*, 2537-2543.

[53] Lu, P.; Teranishi, T.; Asakura, K.; Miyake, M.; Toshima, N. *J. Phys. Chem. B* **1999**, *103*, 9673-9682.

[54] Yonezawa, T.; Toshima, N. *J. Mol. Catal.* **1993**, *83*, 167-181.

[55] Jana, N. R.; Gearheart, L.; Murphy, C. J. *Adv. Mater.* **2001**, *13*, 1289-1393.

[56] Jana, N. R.; Gearheart, L.; Obare, S. O.; Murphy, C. J. 2002, 18, 922-927.

[57] Machulek, A.; Moises, O.; Hueder, P.; Gehlen, A. H. *Photochem. Photobio. Sci.* **2003**, *2*, 921-925.

[58] Jin, R.; Cao, Y. C.; Hao, E.; Metraux, G. S.; Schatz, G. C.; Mirkin, C. A. *Nature* **2003**, *425*, 487-490.

[59] Jin, R.; Cao, Y.; Mirkin, C. A.; Kelly, K. L.; Schatz, G. C.; Zheng, J. G. *Science* **2001**, *294*, 1901-1903.

[60] Pastoriza-Santos, I.; Liz-Marzan, L. M. *Nano Lett.* **2002**, *2*, 903-905.

[61] Jensen, T. R.; Makinsky, M. D.; Haynes, C. L.; Van Duyne, R. P. *J. Phys. Chem. B* **2000**, *104*, 10549-10556.

[62] Jensen, T. R.; Duval, M. L.; Kelly, L.; Lazarides, A. A.; Schatz, G. C.; Van Duyne, R. P. *J. Phys. Chem. B* **1999**, *103*, 9846-9853.

[63] Akamatsu, K.; Tsuboi, N.; Hatakenaka, Y.; Deki, S. *J. Phys. Chem. B* **2000**, *104*, 10168-10173.

[64] Rechberger, W.; Hohenau, A.; Leitner, A.; Krenn, J. R.; Lamprecht, B.; Aussenegg, F. R. *Opt. Commun.* **2003**, *220*, 137-141.

[65] Haynes, C. L.; McFarland, A. D.; Zhao, L.; Van Duyne, R. P.; Schatz, G. C.; Gunnarsson, L.; Prikulis, J.; Kasemo, B.; Kall, M. *J. Phys. Chem. B* **2003**, *107*, 7377-7342.

[66] Su, K.-H.; Wei, Q.-H.; Zhang, X.; Mock, J. J.; Smith, D. R.; Schultz, S. *Nano Lett.* **2003**, *3*, 1087-1090.

[67] Futamata, M.; Maruyama, Y.; Ishikawa, M. *J. Phys. Chem. B* **2003**, *107*, 7607-7617.

[68] Felidj, N.; Aubard, J.; Levi, G. *J. Phys. Chem.* **1999**, *111*, 1195-1208.

[69] Xu, H,; Kall, M. *Phys. Rev. Lett.* **2002**, *89*, 246802.

[70] Zhao, L.; Kelly, K. L.; Schatz, G. C. *J. Phys. Chem. B* **2003**, *107*, 7343-7350.

[71] Michaels, A. M.; Jiang, J.; Brus. L. *J. Phys. Chem. B* **2000**, *104*, 11965-11971.

[72] Xu, H.; Bjerneld, E. J.; Kall, M.; Borjesson, L. *Phys. Rev. Lett.* **1999**, *83*, 4357-4360.

[73] Gunnnarsson, L.; Bjerneld, E. J.; Xu, H.; Petronis, S.; Kasemo, B.; Kall, M. *Appl. Phys. Lett.* **2001**, *78*, 802-804.

[74] Bruchez Jr, M.; Moronne, M.; Gin, P.; Weiss, S.; Alivisatos, A. P.; *Science* **1998**, *281*, 2013-2016.

[75] Li, L.-S.; Hu, J.; Yang, W.; Alivisatos, A. P. *Nano Lett.* **2001**, *1*, 349-351.

[76] Bailey, R.; Nie, S. *J. Am. Chem. Soc.* **2003**, *125*, 7100-7106.

[77] Gao, F. G.; Lu, Q.; Xie, S.; Zhao, D. *Adv. Mater.* **2002**, *14*, 1537-1540.

[78] Higginson, K. A.; Kuno, M.; Bonevich, J.; Qadri, S. B.; Yousuf, M.; Mattoussi, H. *J. Phys. Chem. B* **2002**, *106*, 9982-9985.

[79] Malinsky, M. D.; Kelly, K. L.; Schatz, G. C.; Van Duyne, R. P.; *J. Am. Chem. Soc.* **2001**, *123*, 1471-1482.

[80] Haes, A. J.; Van Duyne, R. P. *J. Am. Chem. Soc.* **2002**, *124*, 10596-10604.

[81] Riboh, J. C.; Haes, A. J.; McFarland, A. D.; Yonzon, C. R.; Van Duyne, R. P. *J. Phys. Chem. B* **2003**, *107*, 1772-1780.

[82] Malinsky, M. D.; Kelly, K. L.; Schatz, G. C.; Van Duyne, R. P. *J. Phys. Chem. B* **2001**, *105*, 2343-2350.

[83] Jensen, T. R.; Duval, M. L.; Kelly, K. L.; Lazarides, A. A.; Schatz, G. C.; Van Duyne, R. P. *J. Phys. Chem. B* **1999**, *103*, 9846-9853.

[84] Hu, W. P.; Chen, S.-J.; Huang, K.-T.; Hsu, J. H.; Chen, W. Y.; Chang, G. L.; Lai, K.-A. *Biosens. Bioelectron.* **2004**, *19*, 1465-1471.

[85] Chou, S.-F.; Hsu, W.-L.; Hwang, J.-M.; Chen, S.-Y. *Biosens. Bioelectron.* **2004**, *19*, 999-1005.

[86] Mirkin, C. A.; Letsinger, R. L.; Mucic, R. C.; Storhoff, J. J. *Nature* **1996**, *382*, 607-609.

[87] Elghanian, R.; Storhoff, J. J.; Mucic, R. C.; Letsinger, R. L.; Mirkin, C. A. *Science* **1997**, *277*, 1078-1081.

[88] Storhoff, J. J.; Lazarides, A. A.; Mucic, R. C.; Mirkin, C. A.; Letsinger, R. L.; Schatz, G. C. *J. Am Chem. Soc.* **2000**, *122*, 4640-4650.

[89] Mirkin, C. A. *Inorg. Chem.* **2000**, *39*, 2258.

[90] Jin, R. C.; Wu, G.S.; Li, Z.; Mirkin, C. A.; Schatz, G. C. *J. Am Chem. Soc.* **2003**, *125*, 1643-1654.

[91] Han, M.; Gao, X.; Su, J. Z.; Nie, S. *Nature Biotech.* **2001**, *19*, 631-635.

[92] Alivisatos, A. P.; *Science* **1996**, 271, 933-937.

[93] Vossmeyer, T.; Katsikas, L.; Giersig, M.; Popovic, I. G.; Diesner, K.; Chemseddine, A.; Eychmuller, A.; Weller, H. *J. Phys. Chem.* **1994**, *98*, 7665-7673.

[94] Nicewarner-Pena, S. R.; Freeman, R. G.; Reiss, B. D.; He, L.; Pena, D. J.; Walton, I. D.; Cromer, R.; Keating, C. D.; Natan, M. J. *Science* **2001**, *294*, 137-141.

[95] Chan, W. C. W.; Nie, S. *Science* **1998**, *281*, 2016-2018.

[96] Fleischmann, M.; Hendra, P. J.; McQuillan, A. J. Chem. Phys. Lett. 1974, 26, 163-166.

[97] Nie, S.; Emory, S. R. Science 1997, 275, 1102-1106.

[98] Kneipp, K.; Wang, Y.; Kneipp, H.; Perelman, L. T.; Itzkan, I.; Dasari, R. R.; Feld, M. S. Phys. Rev. Lett. 1997, 78, 1667-1670.

[99] Cao, Y. C.; Jin, R.; Mirkin, C. A. Science, 2002, 297, 1536-1540.

[100] Burstein, E.; Chen, Y. J.; Chen, C. Y.; Lundquist, S.; Tosatti, E. Solid State Commun. 1979, 29, 567-570.
[101] Ueda, H.; Ichimura, S. Surf. Sci. 1982, 119, 433-448.
[102] Adrian, F. J. J. Chem. Phys. 1982, 77, 5302-5314.
[103] Yamada, H.; Nagata, H.; Toba, K.; Nakao, Y. Surf. Sci. 1987, 182, 269-286.
[104] Meixner, A. J.; Vosgrone, T.; Sackrow, M. J. Lumines. 2001, 94-95, 147-152.
[105] Weiss, A.; Haran, G. J. Phys. Chem. B 2001, 105, 12348-12354.
[106] Michaels, A. M.; Nirmal, M.; Brus, L. E. J. Am. Chem. Soc. 1999, 121, 9932-9939.
[107] Michaels, A. M.; Jiang, J.; Brus, L. J. Phys. Chem. B 2000, 104, 11965-11971.
[108] Xu, H.; Bjerneld, E. J.; Kall, M.; Bprjesson, L. Phys. Rev. Lett. 1999, 83, 4357-4360.
[109] Bjerneld, E. J.; Johansson, P.; Kall, M. Single Mol. 2000, 3, 239-248.
[110] Krug II, J. T.; Wang, G. D.; Emory, S. R.; Nie, S. J. Am. Chem. Soc. 1999, 121, 9208-9214.
[111] Futamata, M.; Maruyama, Y.; Ishikawa, M. J. Phys. Chem. B 2003, 107, 7607-7617.
[112] Maruyama, Y.; Ishikawa, M.; Futamata, M. J. Phys. Chem. B 2004, 108, 673-678.
[113] Ishikawa, M.; Maruyama, Y.; Ye, J. Y.; Futamata, M. J. Lumines. 2002, 98, 81-89.
[114] Blatchford, C. G.; Campbell, J. R.; Creighton, J. A. Surf. Sci. 1982, 120, 435-455.
[115]Creighton, J. A.; Blatchford, C. G.; Albrecht, M. G. J. Chem. Soc., Faraday Trans 2 1979, 75, 790-798.
[116] Xu, H.; Aizpurua, J.; Kall, M.; Apell, P.; Phys. Rev. E. 2000, 62, 4318-4324.
[117] Gunnarsson, L.; Bjerneld, E. J.; Xu, H.; Petronis, S.; Kasemo, B.; Kall, M. Appl. Phys. Lett. 2001, 78, 802-804.
[118] Hao, E.; Schatz, G. C. J. Chem. Phys. 2004, 120, 357-366.
[119] Weitz, D. A.; Garoff, S.; Hanson, C. D.; Gramila, T. J.; Gersten, J. I. J. Lumin. 1981, 24-25, 83-86.
[120] Weitz, D. A.; Garoff, S.; Gersten, J. I.; Nitzan, A. J. Electr. Spectr. Relat. Phenom. 1983, 29, 363-370.
[121] Weitz, D. A.; Garoff, S.; Gersten, J. I.; Nitzan, A. J. Chem. Phys. 1983, 78, 5324-5338.
[122] Crozier, K. B.; Sundaramurthy, A.; Kino, G. S.; Quate, C. F. J. Appl. Phys. 2003, 94, 4632-4642.
[123] Novotny, L. N.; Bian, R. X.; Xie, S. Phys. Rev. Lett, 1997, 79, 645-648.
[124] Calander, N.; Willander, M. Phys. Rev. Lett. 2002, 89, 143603.
[125] Kottmann, J. P.; Martin, O. J. F.; Smith, D. R.; Schultz, S. Chem. Phys. Lett. 2001, 341, 1-6.
[126] Kottmann, J. P.; Martin, O. J. F.; Smith, D. R.; Schultz, J. Microsc. 2001, 202, 60-65.
[127] Kottmann, J. P.; Martin, O. J. F.; Smith, D. R.; Schultz, S. Phys. Rev. B 2001, 64, 235402.
[128] Gryczynski, I.; Malicka, J.; Shen, Y.; Gryczynski, Z.; Lakowicz, J. R. J. Phys. Chem. B

2002, 106, 2191-2195.
[129] Chance, R. R.; Prock, A.; Silbey, R. Adv. Chem. Phys. 1978, 37, 1-65.
[130] Wokaun, A.; Lutz, H. P.; King, A. P.; Wild, U. P.; Ernst, R. E. J. Chem. Phys. 1983, 79, 509-514.
[131] Aroca, R.; Kovacs, G.. J.; Jennings, C. A.; Loutfy, R. O.; Vincett, P. S. Langmuir 1988, 4, 518-521.
[132] Kummerlen, J.; Leitner, A.; Brunner, H.; Aussenegg, F. R.; Wokaun, A. Mol. Phys. 1993, 80, 1031-1046.
[134] Chumanov, G.; Sokolov, K.; Gregory, B. W.; Cotton, T. M. J. Phys. Chem. 1995, 99, 9466-9471.
[135] Sokolov, K.; Chumanov, G.; Cotton, T. M. Anal. Chem. 1998, 70, 3898-3905.
[136] Malicka, J.; Gryczynski, I.; Gryczynski, Z.; Lakowicz, J. R. Anal. Biochem. 2003, 315, 57-66.
[137] Hartstein, A.; Kirtley, J. R.; Tsang, J. C. Phys. Rev. B 1980, 45, 201-204.
[138] Hatta, A.; Suzuki, Y,; Suetaka, W. Appl. Phys. A 1984, 35, 135-140.
[139] Kamata, T.; Kato, A.; Umemura, J.; Takenaka, T. Langmuir 1987, 3, 1150-1154.
[140] Badilescu, S.; Ashrit, P. V.; Truong, V. Appl. Phys. Lett. 1988, 52, 1551-1553.
[141] Osawa, M.; Ikeda, M.; J. Phys. Chem. 1991, 95, 9914-9919.
[142] Glass, A. M.; Liao, P. F.; Bergman, J. G.; Olson, D. H. Opt. Lett. 1980, 5, 368-370.
[143] Garoff, S.; Weitz, D. A.; Gramila, T. J.; Hanson, C. D. Opt. Lett. 1981, 6, 245-247.
[144] Craighead, H. G.; Glass, A. M. Opt. Lett. 1981, 6, 248-250.
[145] Hua, X. M.; Gernsten, J. I.; Nitzan, A. J. Chem. Phys. 1985, 83, 3650-3659.
[146] Malicka, J.; Gryczynski, I.; Kusba, J.; Shen, Y.; Lakowicz, J. R. Biochem. Biophys. Res. Commun. 2002, 294, 886-892.
[147] Parfenov, A.; Gryczynski, I.; Malicka, J.; Geddes, C. D.; Lakowicz, J. R. J. Phys. Chem. B 2003, 107, 8829-8833.
[148] Lakowicz, J. R.; Malicka, J.; D'Auria, S.; Gryczynski, I. Anal. Biochem. 2003, 320, 13-20.
[149] Clark, H. A.; Campagnola, P. J.; Wuskell, J. P.; Lewis, A.; Loew, L. M. J. Am. Chem. Soc. 2000, 122, 10234-10235.

[150] Muller, C. J.; Krans, J. M.; Todorov, T. N.; Reed, M. A. *Phys. Rev. B* **1996**, *53*, 1022-1025.
[151] Sirvent, C.; Rodrigo, J. G.; Vieira, S.; Jurczyszyn, L.; Mingo, N.; Flores, F. *Phys. Rev. B* **1996**, *53*, 16086-16090.
[152] Costa-Krämer, J. L. *Phys. Rev. B* **1997**, *55*, R4875-R4878.
[153] Ludoph, G.; Ruitenbeek, J. M. *Phys. Rev. B* **2003**, *61*, 2273-2285.
[154] Agraït, N.; Yeyati, A. L.; Ruitenbeek, J. M. *Phys. Rep.* **2003**, *377*, 81-279.

[155] Rodrigues, V.; Bettini, J.; Rocha, A. R.; Rego, L. G.; Ugarte, D. *Phys. Rev. B* **2002**, *65*, 153402.

[156] Osifchin, R. G.; Reifenberger, R. *Science* **1996**, *272*, 1323-1325.

[157] Brousseau, L. C.; Zhao, Q.; Shultz, D. A.; Feldheim, D. L. *J. Am. Chem. Soc.* **1998**, *120*, 7645-7646.

[158] Chen, S.; Murray, R. W.; Feldberg, S. W. *J. Phys. Chem. B* **1998**, *102*, 9898-9907.

[159] Yau, S.-T.; Mulvany, P.; Xu, W.; Spinks, G. M. *Phys. Rev. B* **1998**, *57*, R15124-R15127.

[160] Inoue, Y.; Fujii, M.; Inata, M.; Hayashi, S.; Yamamoto, K.; Akamatsu, K.; Deki, S. *Thin Solid Films* **2000**, *372*, 169-172.

[161] Huang, S.; Tsutsui, G.; Sakaue, H.; Shingubara, S.; Takahagi, T. *J. Vac. Sci. Technol. B* **2000**, *18*, 2653-2657.

[162] Wang, B.; Xiao, X.; Huang, X.; Sheng, P. *Appl. Phys. Lett.* **2000**, *77*, 1179-1181.

[163] Thomas, P. J.; Kulkarni, G. U.; Rao, C. N. R. *Chem. Phys. Lett.* **2000**, *321*. 163-168.

[164] Ancona, M. G.; Kruppa, W. Rendell, R. W.; Snow, A. W.; Park, D.; Boos, J. B. *Phys.Rev. B* **2001**, *64*, 033408.

[165] Nagano, K.; Okuda, A.; Majima, Y. *Appl. Phys. Lett.* **2002**, *81*, 544-546.

[166] Ohgi, T.; Fujita, D. *Surf. Sci.* **2003**, *532-535*, 294-299.

[167] Xue, Y.; Ratner, M. A. *Phys. Rev. B* **2003**, *68*, 235410.

[168] Chen, S.; Huang, K.; Stearns, J. A. *Chem. Mater.* **2000**, *12*, 540-547.

[169] Wang, B.; Wang, K.; Lu, W.; Wang, H.; Li, Z.; Y, J.; Hou, J. G. *Appl. Phys. Lett.* **2003**, *82*, 3767-3769.

[170] Lu, W.; Wang, B.; Wang, K.; Wang, X.; Hou, J. G. *Langmuir* **2003**, *19*, 5887-5891.

[171] Hou, J. G.; Wang, B.; Yang, J.; Wang, K.; Lu, W.; Li, Z.; Wang, H.; Chen, D. M.; Zhu, Q. *Phys. Rev. Lett.* **2003**, *90*, 246803.

[172] Kim, T. W.; Choo, D. C.; Shim, J. H. Jung, M.; Kang, S. O.; Lee, H. S.; Lee, J. Y. *Appl. Phys. Lett.* **2001**, *79*, 120-122.

[173] Emult, F.; Yamane, K.; Mitani, S.; Yakushiji, K.; Takanashi, K.; Takahashi, Y. K.; Hono, K. *Appl. Phys. Lett.* **2004**, *84*, 3106-3108.

[174] Petit, C.; Cren, T.; Roditchev, D.; Sacks, W.; Klein, J.; Pileni, M.-P. *Adv. Mater.* **1999**, *11*, 1198-1202.

[175] Petit, C.; Pileni, M. P. *Appl. Surf. Sci.* **2000**, *162-163*, 519-528.

[176] Graf, H.; Vancea, J.; Hoffmann, H. *Appl. Phys. Lett.* **2002**, *80*, 1264-1266.

[177] Fan, F.-R. F.; Bard, A. J.; *Science* **1997**, *277*, 1791-1793.

[178] Han, M. Y.; Quek, C. H. *Langmuir* **2000**, *16*, 362-367.

[179] Amman, M.; Wilkins, R.; Ben-Jacob, E.; Maker, P. D.; Jaklevic, R. C. *Phys. Rev. B* **1991**, *43*, 1146-1149.

[180] Hanna, A. E.; Tinkham, M. *Phys. Rev. B* **1991**, *44*, 5919-5922.

[181] Mott, N. F.; *Plil. Mag.* **1969**, *19*, 835.

[182] Ambegaokar, V.; Halperin, B. I.; Langer, J. S. *Phys. Rev. B* **1971**, *4*, 2612.

[183] Sheng, P.; Abeles, B.; Arie, Y. *Phys. Rev. Lett.* **1973**, *31*, 44-47.

[184] Abeles, B.; Sheng, P.; Coutts, M. D.; Arie, Y. *Adv. Phys.* **1975**, *24*, 407-461.

[185] Helman, J. S.; Abeles, B. *Phys. Rev. Lett.* **1976**, *37*, 1429-1432.

[186] Bond, G. C.; Sermon, P. A.; Webb, G.; Buchanan, D. A.; Wells, P. B. *J. Chem. Soc., Chem. Commun.* **1973**, 444b-445.

[187] Bond, G. C.; Sermon, P. A. *Gold Bull* **1973**, *6*, 102-106.

[188] Date, M.; Okamura, M.; Tsubota, S.; Haruta, M. *Angew. Chem. Int. Ed.* **2004**, *43*, 2129-2132.

[189] Date, M.; Haruta, M. *J. Catal.* **2001**, *201*, 221-224.

[190] Date, M.; Ichihashi, Y.; Tamashita, T.; Chiorino, A.; Boccuzzi, F.; Haruta, M. *Catal. Today* **2002**, *72*, 89-94.

[191] Sayo, K.; Deki, S.; Hayashi, S. *J. Mater. Chem.* **1999**, *9*, 937-942.

[192] Gardnerm S.; Hoflund, G. B. *Langmuir*, **1991**, *7*, 2135-2139.

[193] Baiker, A.; Maciejewski, M.; Tagliaferri, S.; Hug, P. *J. Catal.* **1995**, *151*, 407-419.

[194] Wagner, F. E.; Galvagno, S.; Milone, C.; Visco, A. M.; Stievano, L.; Calogero, S. *J. Chem. Soc. Faraday Trans.* **1997**, *93*, 3403-3409.

[195] Shaikhutdinov, S. K.; Meyer, R.; Naschitzki, M.; Maumer, M.; Freund, H. J. *Catal. Lett.* **2003**, *86*, 211-219.

[196] Bulushev, D. A.; Kiwi-Minsker, L.; Yuranov, I.; Suvorova, E. I.; Buffat, P. A.; Renken, A. *J. Catal.* **2002**, *210*, 149-159.

[197] Guczi, L.; Horvath, D.; Paszti, Z, Peto, G. *Catal. Today* **2002**, *72*, 101-105.

[198] Guczi, L.; Horvath, D.; Paszti, Z,; Toth, L.; Horvath, Z. E.; Karacs, A.; Peto, G. *J. Phys. Chem. B* **2000**, *104*, 3138-3193.

[199] Kozlov, A. I.; Kozlova, A. P.; Asakura, K.; Matsui, Y.; Kogure, T.; Shido, T.; Iwasawa, Y. *J. Catal.* **2000**, *196*, 56-65.

[200] Yuan, Y.; Kozlova, A. P.; Asakura, K.; Wan, H.; Tsai, K.; Iwasawa, Y. *J. Catal.* **1997**, *170*, 191-199.

[201] Bulushev, D. A.; Yuranov, I.; Suvorova, E. I.; Buffat, P. A.; Kiwi-Minsker, L. *J. Catal.* **2004**, *224*, 8-17.

[202] Jia, J.; Haraki, K.; Kondo, J. N.; Domen, Z.; Tamaru, K. *J. Phys. Chem. B* **2000**, *104*, 11153-11156.

[203] Clause, P.; Bruckner, A.; Mohr, C.; Hofmeister, H. *J. Am. Chem. Soc.* **2000**, *122*, 11430-11439.

[204] Mohr, C.; Hofmeister, H.; Claus, P. *J. Catal.* **2003**, *213*, 86-94.

[205] Schimpf, S.; Lucas, M.; Mohr, C.; Rodemerck, U.; Bruckner, A.; Radnik, J.; Hofmeister, H.; Claus, P. *Catal. Today* **2002**, *72*, 63-78.

[206] Hayashi, T.; Tanaka, K.; Haruta, M. *J. Catal.* **1998**, *178*, 566-575.

[207] Andreeva, D.; Tabakova, T.; Ilieva, L.; Naydenov, A.; Mehanjiev, D.; Abrashev, M. V. *Appl. Catal. A* **2001**, *209*, 291-300.

[208] Cant, N. W.; Hall, W. K. *J. Phys. Chem.* **1971**, *75*, 2914-2921.

[209] Okumura, M.; Nakamura, S.; Tsubota, S.; Nakamura, T.; Azuma, M.; Haruta, M. *Catal. Lett.* **1998**, *51*, 53-58.

[210] Patil, N. S.; Uphade, B. S.; Jana, P.; Bharagava, S. K.; Choudhary, V. R. *J. Catal.* **2004**, *223*, 236-239.

[211] Bamwenda, G. R.; Tsubota, S.; Nakamura, T.; Haruta, M. *Catal. Lett.* **1997**, *44*, 83-87.

[212] Hayashi, T.; Tanaka, K.; Haruta, M. *J. Catal.* **1998**, *178*, 566-575.

[213] Molina, L. M.; Hammer, B. *Phys. Rev. Lett.* **2003**, *90*, 206102.

[214] Bonard, J. M.; Salvetat, J. P.; Stockli, T.; Forro, L.; Chatelain, A. *Appl. Phys. A* **1999**, *69*, 245-254.

[215] Kong, J.; Franklin, N. R.; Zhou, C.; Chapline, M. G.; Peng, S.; Cho, K.; Dai, H. *Science* **2000**, *287*, 622-625.

[216] Bachtold, A.; Hadley, P.; Nakanishi, T.; Dekker, C. *Science* **2001**, *294*, 1317-1320.

[217] Liao, H.; Hafner, J. H. *J. Phys. Chem. B* **2004**, *108*, 6941-6943.

[218] Cheung, C. L.; Kurtz, A.; Park, H.; Lieber, C. M. *J. Phys. Chem. B* **2002**, *106*, 2429-2433.

[219] Kiang, C. H.; Goddard III, W. A.; Beyers, R.; Salem, J. R.; Bethune, D. S. *J. Phys. Chem.* **1994**, *98*, 6612-6618.

[220] Bachilo, S. M.; Balzano, L.; Herrera, J. E.; Pompeo, F.; Resasco, D. E.; Weisman, R. B. *J. Am. Chem. Soc.* **2003**, *125*, 11186-11187.

[221] Lyu, S. C.; Liu, B. C.; Lee, C. J.; Kang, H. K.; Yang, C. W.; Park, C. Y. *Chem. Mater.* **2003**, *15*, 3951-3954.

[222] Lyu, S. C.; Liu, B. C.; Lee, S. H.; Park, C. Y.; Kang, H. K.; Yang, C. W.; Lee, C. J. *J. Phys. Chem. B* **2004**, *108*, 1613-1616.

[223] Seraphin, S.; Zhou, D. *Appl. Phys. Lett.* **1994**, *64*, 2087-2089.

[224] Saito, Y.; Koyama, T.; Kawabata, K. *Z. Phys. D* **1997**, *40*, 421-424.

[225] Journet, C.; Maser, W. K.; Bernier, P.; Loiseau, A.; Chapelle, M. L.; Lefrant, S.; Deniard, P.; Lee, R.; Fischer, J. E. *Nature* **1997**, *388*, 756-758.

[226] Seraphin, S.; Zhou, D. *Appl. Phys. Lett.* **1994**, *64*, 2087-2089.

[227] International Tables of Selected Constants; 16 Metals, Thermal and Mechanical Data, Allard, S., Pergamon, 1969

[228] A Handbook of Lattice Spacings and Structures of Metals and Alloys, Pearson. W.B., Pergamon, 1967

[229] Castro, T.; Reifenberger, R.; Choi, E.; Andres, R. P. *Phys. Rev. B* **1990**, *42*, 8548-8556.

[230] Buffat, P.; Borel, J. -P. *Phys. Rev. A* **1976**, *13*, 2287-2298.

[231] Lai, S. L. Guo, J. Y.; Petrova, V.; Ramanath, G.; Allen, L. H. *Phys. Rev. Lett.* **1996**, *77*, 99-102.

[232] Dippel, M.; Maier, A.; Gimple, V.; Wider, H.; Evenson, W. E.; Rasera, R. L.; Schatz, G. *Phys. Rev. Lett.* **2001**, *87*, 095505.

[233] Zhang, M.; Efremov, M. Y.; Schiettekatte, F.; Olson, E. A.; Kwan, A. T.; Lai, S. L.; Wisleder, T.; Greene, J. E.; Allen, L. H. *Phys. Rev. B* **2000**, *62*, 10548-10557.

[234] Peters, K.; Cohen, J. B.; Chung, Y.-W. *Phys. Rev. B* **1998**, *57*, 13430-13438.

[235] Antonelli, A.; Khanna, S. N.; Jena, P. *Phys. Rev. B* **1993**, 8263-8266.

[236] Goldstein, A. N.; Echer, C. M.; Alivisatos, A. P. *Science* **1992**, *256*, 1425.

[237] Ercolessi, F.; Andreoni, W.; Tosatti, E. *Phys. Rev. Lett.* **1991**, *66*, 911-914.

[238] Vololitin, Y.; Sinzig, J.; de Jongh, L. J.; Schmid, G.; Vargaftik, M. N.; Moiseev. *Nature* **1996**, *384*, 621-623.

[239] Gerion, D. G.; Hirt, A.; Billas, I. M. L.; Chatelain, A.; de Heer, W. A.. *Phys. Rev. B* **2000**, *62*, 7491-7501.

[240] Mays, C. W.; Vermaak, J. S.; Kuhlmann-Wilsdorf, D. *Surf. Sci.* **1968**, *12*, 134-140.

[241] Wasserman, H. J.; Vermaak, J. S. *Surf. Sci.* **1970**, *22*, 164-172.

[242] Wasserman, H. J.; Vermaak, J. S. *Surf. Sci.* **1972**, *32*, 168-174.

[243] Koga, K.; Ikeshoji, T.; Sugawara, K. *Phys. Rev. Lett.* **2004**, *92*, 115507.

[244] Kitakami, O.; Sato, H.; Shimada, Y.; Sato, F.; Tanaka, M. *Phys. Rev. B* **1997**, *56*, 13849-13854.

[245] Noguchi, T.; Gotoh, K.; Yamaguchi, Y.; Deki, S. *J. Mater. Sci. Lett.* **1991**, *10*, 648-649

[246] Noguchi, T.; Murakami, S.; Gotoh, K.; Yamaguchi, Y.; Deki, S. *J. Mater. Sci. Lett.* **1992**, *11*, 797-798.

[247] Akamatsu, K.; Deki, S. *J. Mater. Chem.* **1997**, *7*, 1773-1777.

[248] Akamatsu, K.; Deki, S. *J. Mater. Chem.* **1998**, *8*, 637-640.

[249] Akamatsu, K.; Deki, S. *J. Colloid Interface Sci.* **1999**, *214*, 353-361.

[250] Akamatsu, K.; Tsuboi, N.; Hatakenaka, Y.; Deki, S. *J. Phys. Chem. B* **2000**, *104*, 10168-10173.

PART I

New Preparation Route for Carbon Thin Films Incorporating Metal Nanoparticles

Chapter 2

Preparation of Carbon Thin Films Containing Gold Nanoparticles Using Polyacrylonitrile Thin Films as Carbon Precursors

2.1. Introduction

Since metal nanoparticle possesses high surface energy because the number of surface atoms increases rapidly with decreasing the particle size down to nanometer scale, we have to manipulate with supporting them on a certain support such as metal oxide, polymer, glass, and carbon. Amongst of these supporting materials, carbon is attractive for applicational use because of its high stability and variety of physical and chemical properties according to its crystallographic structure, ranging from amorphous carbon to highly oriented pyrolytic graphite (HOPG). Within the past few years, several researchers have succeeded in encapsulating various metal nanoparticles into carbon matrix with different morphology by gas evaporation [1], arc-discharge [2-6], co-sputtering [7], and pressure pyrolysis of organometallic polymer [8-10]. Using these methods, however, some by-products such as metal carbide or carbonaceous debris are occasionally contained in the product, which interferes the characteristics of the resultant composite film.

In this chapter, novel fabrication strategies is proposed for the preparation of metal nanoparticle/ carbon composite films by using polyacrylonitrile (PAN) as a carbon precursor. Starting materials were prepared by successive vapor deposition of PAN and metal, and the following heat-treatment induced carbonization of PAN, along with the dispersion of metal nanoparticles into matrix. Structural changes of PAN during heat-treatment have been intensively studied because of its practical importance for the production of carbon fibers [11-21]. In the present study, the structural changes of vapor deposited PAN was investigated by IR and Raman spectroscopies, and the morphology and dispersion behavior of metal nanoparticles were examined by XPS and TEM observation.

2.2. Experimental

Au/PAN stacking films were prepared by successive vacuum evaporation of PAN and gold. PAN

thin film with a thickness of 100 nm was first deposited using a resistance-heated molybdenum boat at a pressure of $< 10^{-4}$ Torr, and then Au metal (99.99 %) was deposited on pre-deposited PAN layer using an alumina-coated tungsten filament. The pressure during Au evaporation was kept at 2.0×10^{-5} Torr, and the amount of Au deposition was 11.8×10^{15} atoms/cm^2. The amount of deposition and the deposition rate (2 Å/s for PAN, 0.2 Å/s for Au) were monitored and controlled by a quartz-crystal microbalance. The vapor deposition of both PAN and Au were carried out at room temperature. The obtained Au/PAN stacking films were then heat-treated under N_2 flow at the temperature ranging from 100 ℃ to 600 ℃ for 1 h.

The particle size and size distribution of gold nanoparticles were obtained by TEM(JEM-2010; JEOL) operated at 200 kV. XRD measurement was carried out with RINT 2000 diffractometer (Rigaku), using Cu K_α(40 kV, 40 mA) as X-ray source. The diffraction intensities in the region of 2 θ from 10° to 90° were measured by step scanning at intervals of 0.1° in 2 θ with a fixed time of 10 sec. The intensities were accumulated by repeating the measurement 3 times. The structural changes of PAN film with heat treatment were examined by using FT-IR spectroscopy (FT/IR-615R; JASCO) and Raman spectroscopy (Spex 1877 Triplemate) in the region from 400 to 4000 cm^{-1} and 1100 to 1700 cm^{-1}, respectively.

2.3 Results and Discussion

2.3.1 Structure and morphology of Au nanoparticles in PAN matrix.

XRD patterns of the sample before and after the heat-treatment at different temperatures are shown in Figure 1. Five diffraction lines observed at 38, 44, 65, 78 and 81° is attributable to gold fcc structure. A broad peak at around 20° is due to scattering from a quarts glass substrate. The diffraction lines of gold become intense and sharp as the heat-treatment temperature increases, indicating the growth of gold crystallites. From the Au (111) diffraction peak, the crystallite size and the lattice constant were estimated based on Scherrer's formula (Table1). The crystallite size is almost unchanged below the heat-treatment temperature of 200 ℃, and increases gradually by the heat-treatment above 300 ℃. Although the lattice constant increases slightly by the heat treatment, the value of 4.069 Å for the sample heat-treated at 600 ℃ is still less than the bulk value (4.078 Å), indicating that the lattice contraction of Au takes place and relaxes to some extent by the heat treatment. Figure 2 shows plan-view TEM images of the sample before and after the heat treatment at various temperatures. Gold nanoparticles with ~10 nm in diameter are well isolated, even after the heat treatment at 600 ℃. The mean particle diameter and the corresponding standard deviation of the gold nanoparticles for each sample are also given in

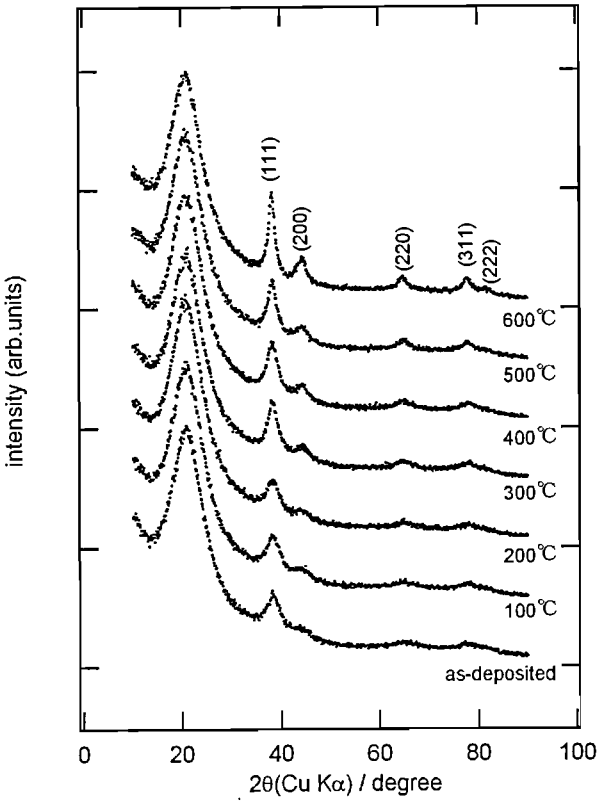

Figure 1. XRD patterns of gold/PAN composite films heated at various temperatures. A broad diffraction band centered at 20° is from quartz glass substrate. Each diffraction line assigned to fcc-gold becomes sharp with increasing the heating temperature.

Table 1. Parameters of gold nanoparticles in Au/PAN composite film.

heat-treatment temperature / ℃	crystallite size (XRD) / nm	lattice constant / Å	mean diameter[a] (TEM) / nm
as deposition	3.2	4.054	3.6 (0.7)
100	3.2	4.053	3.5 (0.8)
200	3.4	4.058	3.8 (0.9)
300	3.9	4.057	4.4 (1.4)
400	4.1	4.061	5.7 (2.4)
500	4.7	4.063	9.8 (3.3)
600	6.1	4.069	9.8 (3.5)

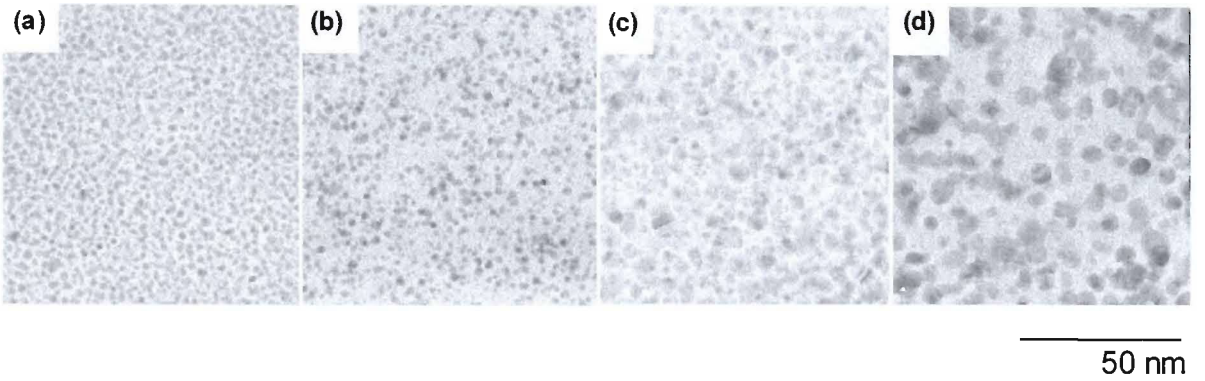

Figure 2 TEM images of Au/PAN composite films. (a) as-deposited sample (b)-(d) the sample after the heat-treatment; heat-treatment temperature is (b) 200 ℃, (c) 400 ℃, and (d) 600 ℃.

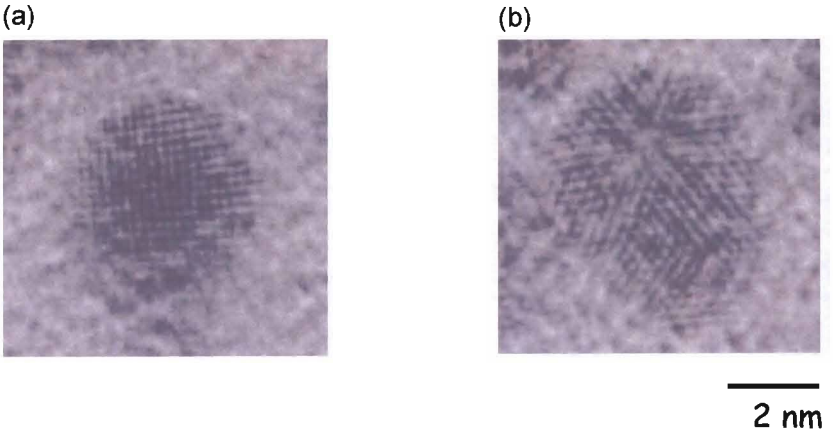

Figure 3. HR-TEM images of (a) single crystalline and (b) multi-twinned gold nanoparticles observed in Au/PAN composite films after the heat-treatment.

Table 1. The mean size was obtained by counting at least 500 particles on plan-view TEM images. The mean particle size gradually increases above 300 ℃, although there is no distinct change below 200 ℃. This tendency agrees well with the change in the crystallite size obtained by XRD measurements. However, the mean particle size obtained by TEM image is slightly larger than the corresponding crystallite size from XRD. This indicates the presence of poly-crystalline gold nanoparticles, and actually both single- and poly-crystalline gold nanoparticles were observed as shown in Figure 3.

In order to obtain the insight into the distribution profile of gold nanoparticles in the depth direction, XPS measurement was made with etching the sample surface by argon ion. The results are shown in Figure 4, in which XPS depth profiles for the sample before and after the heat-

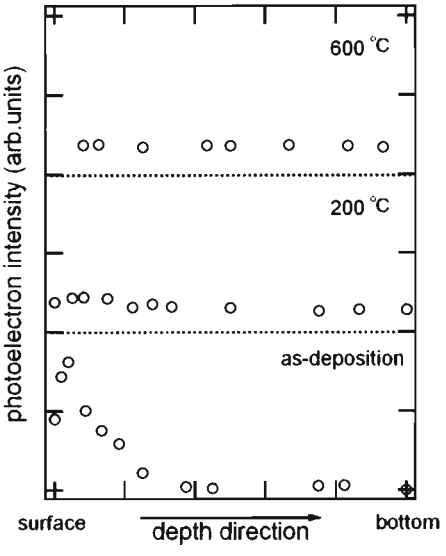

Figure 4. XPS depth profiles of Au/PAN composite films before and after the heat-treatment.

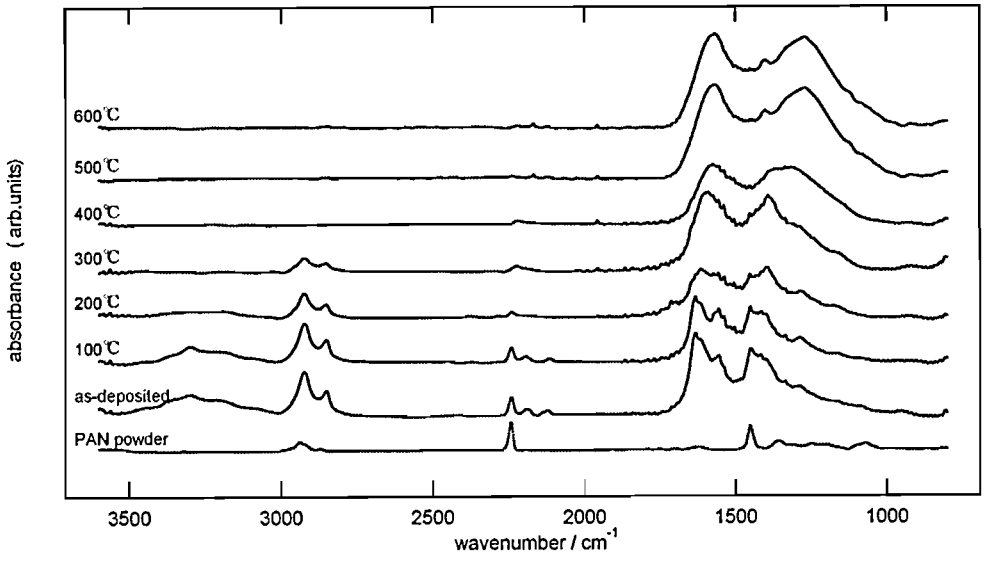

Figure 5. IR absorption spectra of PAN powder and Au/PAN composite films before and after the heat-treatment.

treatment at 200 ℃ and 600 ℃ were plotted. Gold nanoparticles that is localized at the surface in the as-deposited sample dispersed into the PAN layer after the heat-treatment at 200 ℃, and the distribution profile does not exhibit any significant change by the heat-treatment at 600 ℃.

2.3.2 Structural change of vapor deposited PAN thin films

Figure 5 shows the changes in the IR absorption spectra of Au/PAN composite films before and after the heat treatment at various temperatures. The spectrum of original PAN powder is also included. The spectrum of as-deposited PAN thin film showed some differences from that of the original PAN powder, suggesting the structural changes of PAN molecules occurred during thermal evaporation. After the vapor deposition, an intense peak assigned to stretching vibration of C-N triple bond at 2245 cm^{-1} is greatly reduced and split, and a new absorption band is observed at 2190 cm^{-1}. Structural change of PAN induced by heat-treatment has previously been investigated in detail [11-21], and it is well known that carbonization (cyclization) takes place in the course of heat treatment [11,14-20]. Grassie *et al.* reported that heat-treatment of PAN occasionally induces the formation of β-imino nitrile structure, resulting in the splitting of nitrile band and appearance of a new band at 2190 cm^{-1}, as is the case with the present study [16]. Thus, the observed changes in the nitrile region would be attributable to the formation of β-imino nitrile during the vapor deposition.

In general, a polymer degrades during vapor deposition into smaller molecules via thermal energy. The way of degradation is devided into two types: depolymerization at a chain end and random degradation. It has been reported that PAN degrades through random chain scission along a polymer chain [22]. Therefore, the formation mechanism of β-imino nitrile occurred during vapor deposition would be expressed as follows:

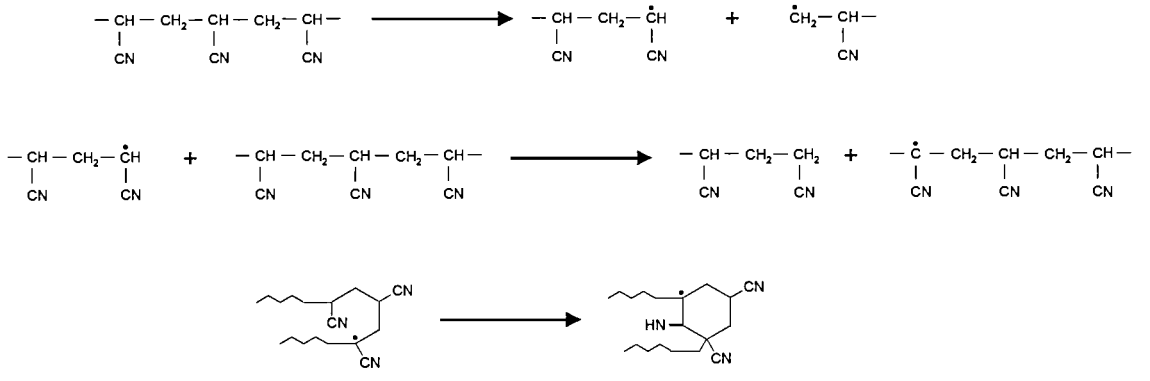

In addition, thermal decomposition possibly takes place at a side chain, resulting in the formation of C-C double bond and intermolecular linking:

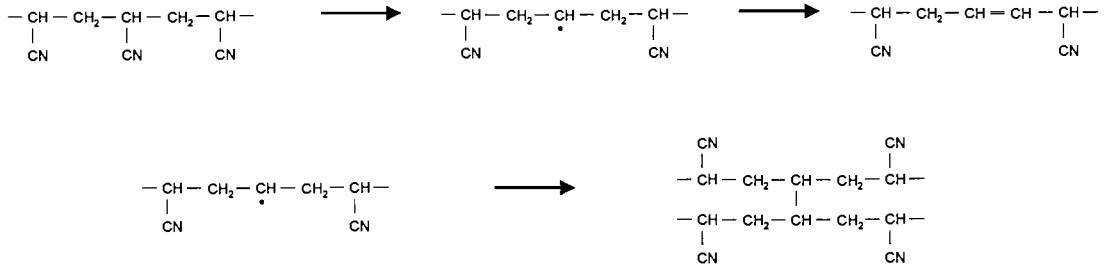

A broad absorption centered at approximately 3300 cm^{-1} observed for the as-deposited sample would be assigned to a –NH structure with intermolecular association, presumably an imine [16]. In addition, intense doublet appears at 1630 and 1580 cm^{-1} in the as-deposited sample. These bands originate from the formation of the conjugated system; $-(C=C)_x-$ or $-(C=N)_x-$. The appearance of the conjugation band strongly suggest the formation of heterocycric structures.

In the course of heat treatment from 100 ℃ to 600 ℃, significant changes in IR absorption spectrum were observed, *e.g.*, the reduction in intensities of peaks at 2240 cm^{-1} (nitrile band) and at 2800-3000 cm^{-1} (carbon-hydrogen stretching mode). C-H region contains several modes and an example of a deconvolution into some gaussian components is shown in Figure 6. The dominant absorption bands at 2850 cm^{-1} and 2925 cm^{-1} are attributable to sp^3 CH_2 vibration mode [23,24]. These peaks decreased in intensity by the heat-treatment at 200 ℃, and disappeared above 400 ℃

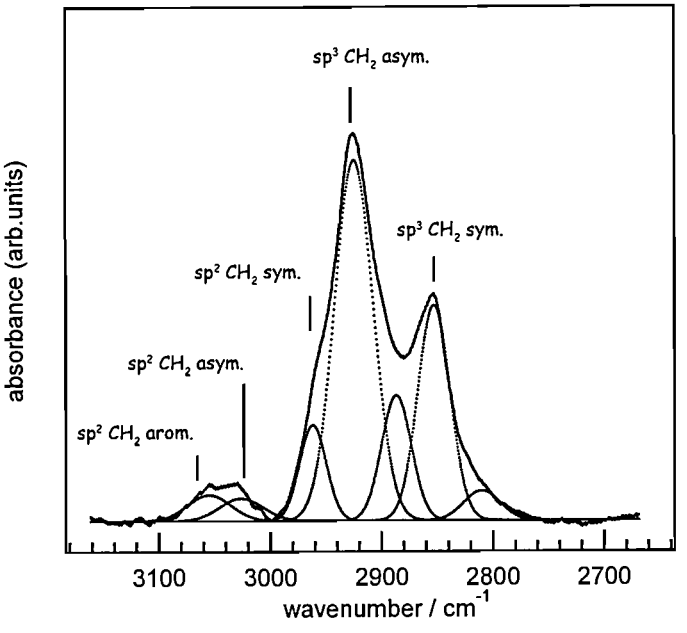

Figure 6. Typical curve-fitting result of IR spectrum (methylene region) into some Gaussian components. (heat treatment temperature : 300℃)

(Figure 5). By the heat treatment at 200 ℃ and 300 ℃, a weak shoulder at 2950 cm^{-1}, which is assigned to sp^2 CH_2 band, was also observed. The nitrile peak was also reduced in intensity at 200 ℃, and very slightly shifted to lower frequency side with the heat treatment. This shift is thought to be due to an electron resonance of a nitrile group with another part of the molecule, or imine-enamine tautomerism [25]. In addition, the broad band assigned to imine at around 3300 cm^{-1} disappeared after the heat-treatment at 300 ℃. Although there was no significant change in the band position of the conjugation band below 100 ℃, the band shifted to lower frequency side by the heat treatment above 200 ℃, indicating the progress of the formation of conjugated system.

Figuire 7 displays Raman spectra of Au/PAN composite films before and after the heat-treatment, in which two broad peaks are observed at around 1360 cm^{-1} and 1580 cm^{-1}, so-called D-line and G-line, respectively. Large single crystalline graphite and HOPG show only G-line in Raman spectrum [26], while disorder or fine graphite crystallites show both G- and D-line [27,28]. Figure 8 represents the variation in the intensity ratio of D- and G-band (I_D/I_G ratio) with the heat-treatment temperature, in which a transition from increase to decrease is observed at 300 ℃. Tuinstra and Koenig reported a linear relationship between the value of I_D/I_G ratio and the reciprocal of crystallite size [26], *i.e.*, the I_D/I_G ratio decrease with the growth of the crystalline phase. In the presemt system, first increase in I_D/I_G ratio upto 300 ℃ indicates the increase in the number of microcrystalline sp^2 carbon, and the following decrease is attributed to the increase in size of sp^2

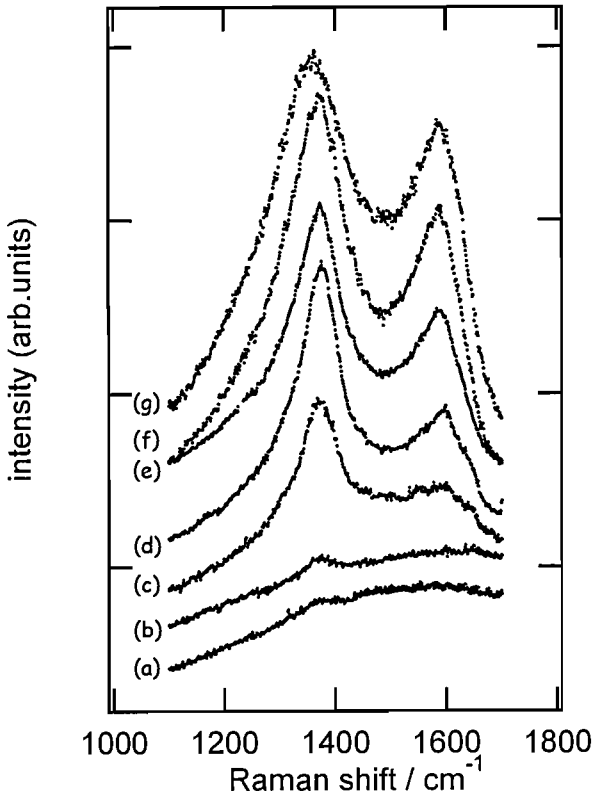

Figure 7. Raman spectra of (a) as-deposited sample and (b)-(g) samples after heat treatment; heat-treatment temperature is (b) 100℃, (c) 200 ℃, (d) 300℃, (e) 400℃, (f) 500℃, and (g) 600℃.

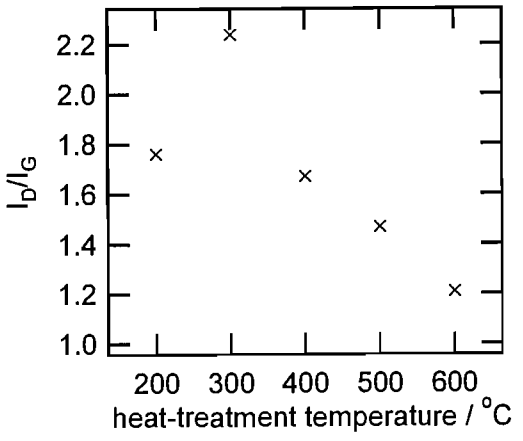

Figure 8. Variation in I_D/I_G value as a function of the heat-treatment temperature.

carbon network.

2.3.3 Surface stress imposed on gold nanoparticles

In the present study, several structural changes of PAN were observed by the heat treatment at 200 ℃, at which the gold particles penetrated into PAN layer. Therefore, it seems likely that the structural changes of PAN matrix are closely related to the dispersion of gold nanoparticles into PAN matrix. From the results of XRD measurements, the lattice contraction of gold nanoparticles was observed. According to Mays *et* al., the lattice contraction can be interpreted in terms of surface stress [29]. Assuming that the surface free energy of small particles are isotropic so that the equilibrium shape of the particle is spherical, and that the particles are crystalline having a cubic structure, the surface stress, f, can be expressed by

$$f = -\frac{3}{4}\frac{\Delta a}{a}\frac{d}{K} \qquad (1)$$

where Δa is the change in the lattice constant, a is the lattice constant of bulk gold, d is the mean particle size of gold particles, K is the bulk compressibility. By using $a = 4.0786$ Å, $K = 6.23 \times 10^{-23}$ m^2/N [30], we can calculate the value of the surface stress for the Au particles with different size. From the results of the calculations, the surface stress of gold nanoparticles in our sample was found to increase slightly from 2.5 for as-deposited sample to 2.7 N/m after the heat treatment at 600 ℃. These values are much smaller than that obtained for gold particles with 1.4-5.0 nm in diameter embedded in a silicon-containing plasma polymer matrix (6.3 ± 1 N/m) [32], and relatively larger than that of gold particles deposited on amorphous carbon film (1.2 N/m) [29] and Au/nylon11 system (1.8 N/m for as-deposited sample and 1.3 N/m for heat-treated sample at

100℃) [32]. The difference observed in these systems is presumably due to the difference in the matrix. The plasma polymer is generally rigid, and high surface stress would be imposed on the embedded gold nanoparticles. It should be also noted that the change in the surface stress with the heat-treatment were different between Au/PAN and Au/nylon11 systems; surface stress increased with the heat treatment in the present system, while it decreased in Au/nylon11 system. Glass transition temperature and melting point of vapor deposited nylon11 is approximately 40℃ and 120℃, respectively, and in this temperature region, nylon11 behave as viscous fluid. This suggest that the structural relaxation of gold nanoparticles embedded in nylon11 thin films would proceed with less stress, and as-deposited metastable gold nanoparticle can be allowed to reach their equilibrium state by the heat-treatment in nylon11 thin film. On the other hand, the situation is quite different in the present study because PAN thin film turned into more rigid state during heat-treatment due to the carbonizaion. As a result, gold nanoparticle would be subject to a strong stress induced by the structural changes of PAN into carbon, resulting in the increase in the surface stress of Au particle in Au/PAN system.

2.4. Coclusion

PAN thin films containing gold nanoparticles were successfully prepared as a precursor for gold nanoparticles/carbon composite film by the heat treatment of Au/PAN stacking film at 200 ℃, at which several structural changes of vapor deposited PAN were observed. Also, gold nanoparticles dispersed into the PAN layers at this temperature. These results suggest that the structural change of PAN induces the dispersion of gold nanoparticles into PAN layer. By the heat treatment at lower temperature (200-300 ℃), microcrystalline sp^2 carbon was formed, which was dominantly caused by the deformation from nitrile group into conjugated system. Although the growth of sp^2 carbon network proceeded by the heat-treatment at higher temperature (400-600 ℃), the matrix after the heat treatment at 600 ℃ was still amorphous. By controlling the composition of the starting materials and the heating condition, the present strategy would be capable of producing carbon thin films with well-defined sp^2/sp^3 composition containing metal nanoparticles with a controlled diameters.

References

[1]C. kaito, T. Sakamoto, D. Ban, T. Izuta, Y. Kitano and Y. Saito, *J. Crystal Growth*, **1996**, *167*, 580.

[2] J. jiao, S. Seraphin, X. Wang and C. Withers, *J. Appl. Phys.*, **1996**, *80*, 103.

[3] Y. Yoshida, *Phisica B*, **1997**, *229*, 301.

[4] Z. Q. Li, H. F. Xhang, Y. Q. Zhang and X. J. Wu, *Nanostructured Mater.*, 1998, **10**, 179.

[5] H. Zhang, J. Chen, Y. He, X. Xue and S. Peng, *Mater. Chem. Phys.*, 1998, **55**, 167.

[6] H. Zhang, *J. Phys. Chem. Solids,* 1999, **60**, 1845.

[7] D. Babonneau, T. Cabioc'h, A.Naudon, J. C. Girard, and M. F. Denanot, *Surf.Sci.*, 1998, **409**, 358.

[8] S. Hirano, T. Yogo, H. Suzuki, S. Naka, *J. Mater. Sci.*, 1983, **18**, 2811.

[9] T.Yogo, S. Naka and S. Hiorano, *J. Mater. Sci.*, 1989, **24**, 2071.

[10] S. Hirano, T. Yogo, K. Kikuta, M. Fukuda, *J. Mater. Sci.*, 1993, **28**, 4073.

[11] N. Grassie and J. H. Hay, *J. Polym. Sci.*, 1962, **56**, 189.

[12] R. T. Conley and J. H. Bieron, *J. Appl. Polym. Sci.*, 1963. **7**. 1757.

[13] N. Grassie and R. McGuchan, *Europ. Polym. J.*, 1970. **6**. 1277.

[14] A. E. Standage and R. D. Matkowsky, *Europ. Polym. J.*, 1971, **7**, 775.

[15] N. Grassie and R. McGuchan, *Europ. Polym. J.*, 1971. **7**. 1091.

[16] N. Grassie and R. McGuchan, *Europ. Polym. J.*, 1971. **7**. 1357.

[17] N. Grassie and R. McGuchan, *Europ. Polym. J.*, 1972. **8**. 257.

[18] N. Grassie and R. McGuchan, *Europ. Polym. J.*, 1972. **8**. 865.

[19] T Usami. T. Itoh, H. Ohtani and S. Tsuge, *Macromolecules*, 1990, **23**, 2460.

[20] T. J. Xue, M. A. mcKinney and C. A. *Wilkie, Polym. Degrad.Stab.*, 1997, **58**, 193.

[21] S. Dalton, F. Heatley and P.M. Budd, *Polymer*, 1999, **40**, 5531.

[22] A. Kubono and N. Okui, *Prog. Polym. Sci.*, 1994, **19**, 389.

[23] E. Sagnes, J. Szurmak, D. Manage, and S. Zukotynski, *J. Non-cryst. Solids*. 1999, **249**, 69.

[24] M. Clin, O. Durand-Drouhin, A. Zeinert, and J. C. Picot, *Diamond Relat. Mater.*, 1999, **8**, 527.

[25] M. M. Coleman and R. J. Petcavich, *J. Polym. Sci.*, 1978, **16**, 821.

[26] F. Tuinstra and J. L. Konig, *J. Chem. Phys.*, 1970, **53**, 1126.

[27] M. A. Capano, N. T. McDevitt, R. K. Singh and F. Qian, *J. Vac. Sci. Technol.*, 1996, A **14**, 431.

[28] J. Schwan, S. Ulrich, V. Batori, H. Ehrhadt, and S. R. P. Silva, *J. Appl. Phys.*, 1996, **80**, 440.

[29] C. W. Mays, J. S. Vermaak and D. Kuhlmann-Wilsdorf, *Surf. Sci.*, **1968**, *12*, 134.

[30] J. S. Vermaak and D. Kuhlmann-Wilsdorf, J. Phys. Chem. **1968**, *12*, 134.

[31] R. Lamber, S. Wetjen, G. Schulz-Ekloff and A. Baalmann, *J. Phys. Chem.*,**1995**, *99*, 13838.

[32] K. Akamatsu and S. Deki, *J. Colloid Interface Sci.*, **1999**, *214*, 353.

Chapter 3

Microstructural Characterization of Gold/Cobalt Alloy Nanoparticles Embedded in Carbon Thin Films

3.1 Introduction

Scientific and technological interests have been stimulating a research activity in the field of bimetallic nanoparticles, including both solid solution and core-shell-like segregated system, because binary system frequently exhibits novel aspects that could not be achieved in single component system. Gold-cobalt binary system is a typical phase separation system with a maximum solubility at 997 ℃ and extremely low mutual solubility at room temperature [1]. However, as already mentioned in Chapter 1, the thermodynamic properties of metal nanoparticle such as the melting temperature could be varied due to their high surface atomic ratio. For example, melting point of gold nanoparticle rapidly decreases down to a few hundreds K as the particle size decreases below 50 Å [2]. Furthermore, thermodynamically stable crystal structure of cobalt nanoparticle was found to change from hcp phase to fcc phase below 200 Å [3]. This fact implies that the phase diagram of any binary metallic system would change from the corresponding bulk system.

Gold/cobalt alloy structure (solid-solution) has previously been prepared by Tsaur et al., in which the formation of gold/cobalt solid solution was achieved by ion-beam bombardment of gold/cobalt stacked film with a thickness of ~ 650 Å [4]. However this solid solution is still thermodynamically metastable and the heat-treatment at 300 ℃ resulted in the segregation into gold and cobalt phase. On the basis of their study, the possibility of obtaining thermodynamically stable gold/cobalt alloy structure is fully expected if the dimension of gold/cobalt binary system was further reduced.

In the present chapter, gold/cobalt alloy nanoparticles with several atomic ratios were prepared by co-evaporation method. The morphology and the crystal structure of the resultant nanoparticles were investigated. Also, thermal stability of these nanoparticles was examined by heating them at 600 ℃, which is higher than the temperature that the gold/cobalt solid solution thin film decomposed.

3.2Experimental

The sample was obtained according to the protocol mentioned in Chapter 2, excepting for the

metal deposition process. Au and Co were vapor deposited on the pre-deposited PAN matrix using two independent alumina-coated tungsten filament. The amount of deposition and the deposition rate were monitored by two independent QCMs. Three samples with different atomic ratio, Au/Co=8/2, 5/5, 2/8, were prepared by controlling the deposition rate of metal. The average thickness of the metal layer was 5 nm in any sample. The binding energy of Au 4f and Co 2p electrons were examined by X-ray photoelectron spectroscopy (Shimadzu, ESCA-850), and the morphology and structural analysis were carried out by using transmission electron microscope (JEOL, JEM-2010) operated at 200 kV.

3.3 Results and discussion

3.3.1 XPS analysis for Au-Co co-deposited nanoparticles

Figure 1 shows the Au 4*f* and Co 2*p* photoelectron spectra of as-deposited sample with Au/Co=5/5, together with the sample deposited with monometallic gold or cobalt. Au 4*f* core level of co-deposited sample shifted to higher binding energy side by 0.2 eV relative to Au monometallic system, whereas Co 2*p* level showed only a slight negative shift (0.08 eV). It is well known that an alloying with two or more components results in the shift in binding energy of the constituent elements. Au is the most electronegative metallic element, and therefore, the formation of gold/cobalt alloy structure would result in an overall charge transfer from Co site to Au site. Positive

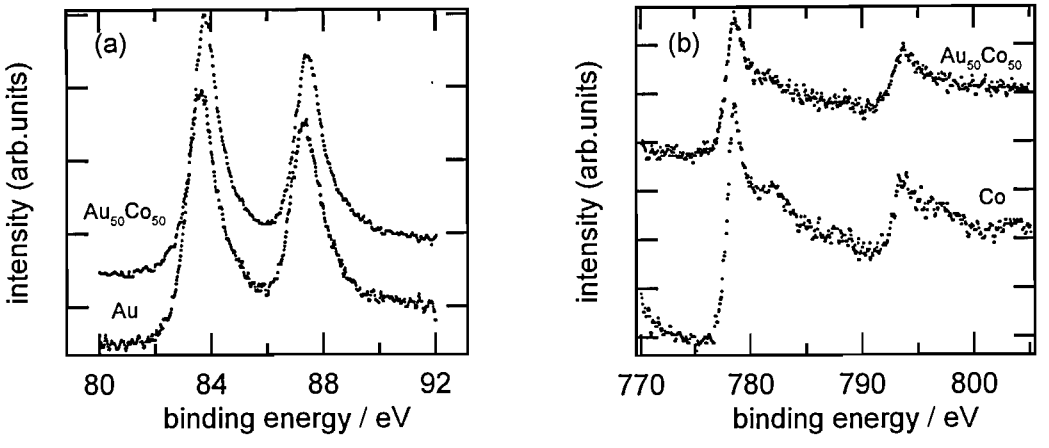

Figure 1. (a) Au 4*f* and (b) Co 2*p* X-ray photoelectron spectra of as-deposited sample prepared with the atomic ratio of Au/Co=5/5 . Spectra for the sample containing monometallic gold or cobalt nanoparticles are also shown.

binding energy shift of Au 4*f* level, however, indicates a depletion of the charge at the Au site. This inconsistent is interpreted in terms of a charge compensation model [5], in which Au loses *d* charge but is overcompensated by *s-p* charge gain, resulting in a small net charge flow from Co to Au. Similar phenomena have been reported for some gold-based bimetallic systems [6-8]. From this results, it was suggested that the as-deposited sample obtained by simultaneous evaporation of gold and cobalt would consist of gold/cobalt alloy nanoparticles, but not gold and cobalt monometallic nanoparticles.

As has been mentioned in Chapter 2, gold nanoparticles disperse into PAN layer by the heat-treatment at 200℃, and homogeneous distribution within the matrix layer was preserved even after the heat-treatment at 600 ℃. The same assessment was done for gold/cobalt bimetallic system, and the results are shown in Figure 2. The profiles exhibited almost the same change with heat-treatment with those obtained for the monometallic gold nanoparticle system. Furthermore, distribution profiles of gold and cobalt exhibited good overlapping with each other, supporting the possibility of the formation of bimetallic alloy nanoparticle; otherwise each component could show different distribution profiles.

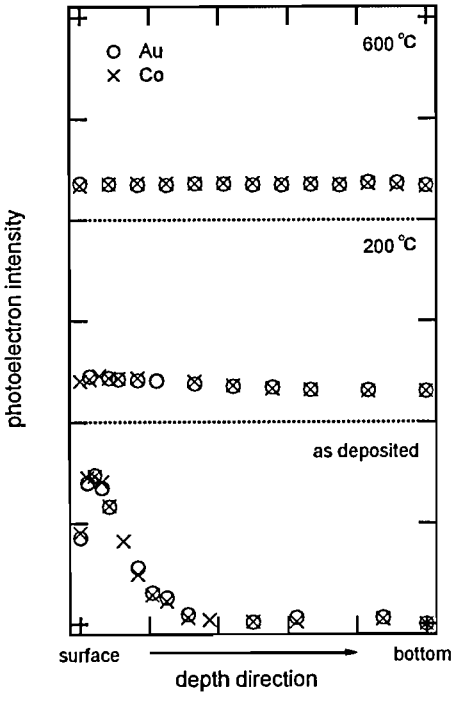

Figure 2. XPS depth profiles of gold/cobalt co-deposited PAN thin films, before and after the heat-treatment.

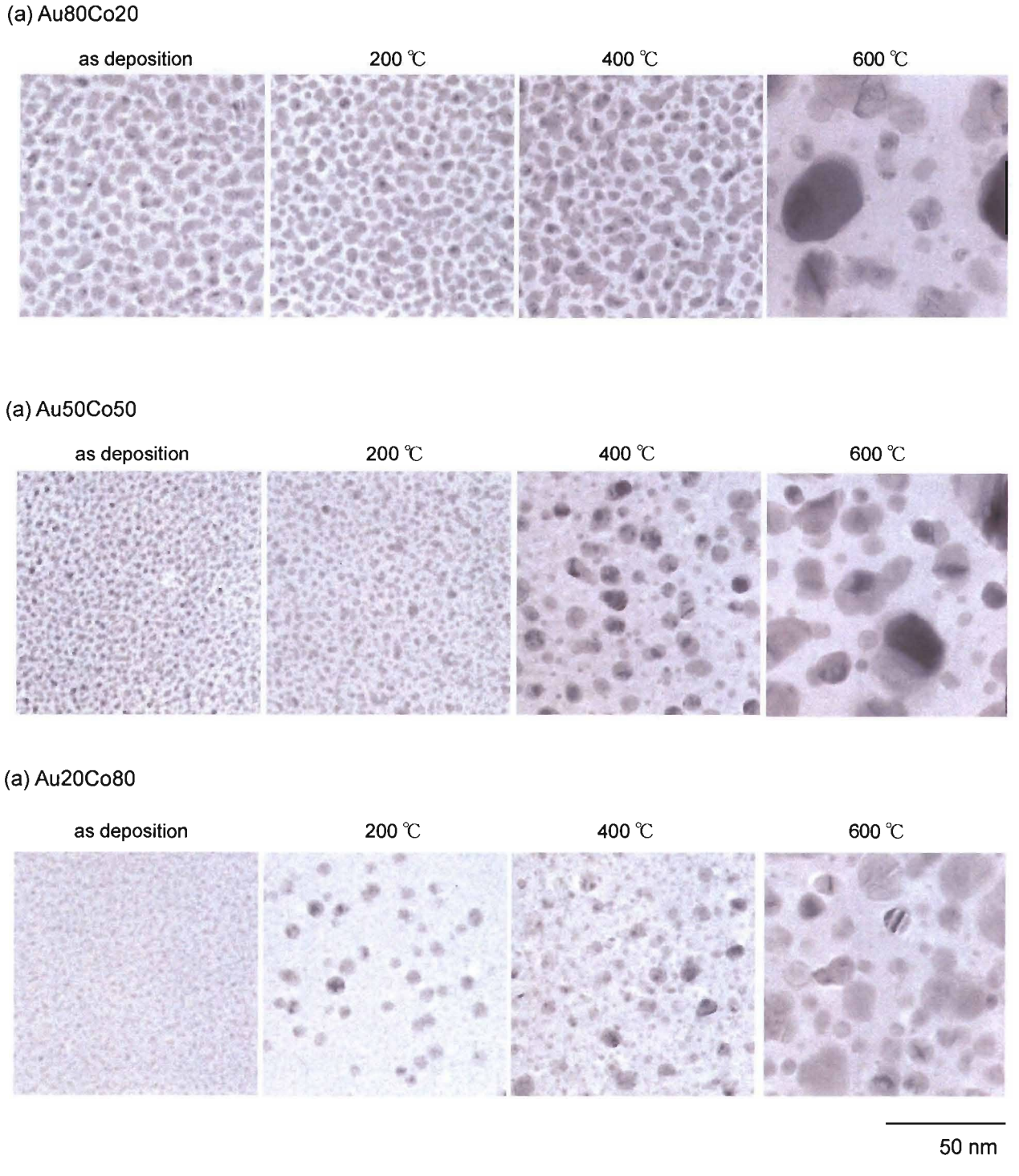

Figure 3. TEM images of gold/cobalt alloy nanoparticles with the atomic ratio Au/Co of (a) 80/20, (b) 50/50, (c) 20/80.

Table 1. Mean particle diameter of gold/cobalt alloy nanoparticles.

heat-treatment temperature/℃	mean diameter/nm			
	Au/Co ratio			
	10/0	8/2	5/5	2/8
as dep.	3.58	3.78	2.21	1.73
200	3.75	3.89	2.30	2.01
400	5.64	4.00	4.04	2.19
600	9.80	8.01	8.38	5.52

3.3.2 Morphology and crystal structure of Au/Co alloy nanoparticles

Plan view TEM images of the samples with different Au/Co atomic ratio before and after the heat-treatment at various temperatures are shown in Figure 3. The mean particle sizes of each sample were summarized in Table 1, in which the result for Au-monometallic system (Chapter 2) is also included. After the heat-treatment at 200 ℃, there was only a slight increasee in the mean particle size compared with that of the as-deposited sample for any composition. This is indicative of the ability of PAN molecule to stabilize the nanoparticles and to prevent from the particle growth or aggregation. The PAN molecule has a nitrogen atom at the side chain, and the functional group containing a nitrogen atom such as amide or nitrile group thought to be effective to interact with the surface of metal nanoparticles[9], similar to a sulfur atom in thiol used as the protective agents for the metal nanoparticles prepared by the reduction of metal ions. In the present study,

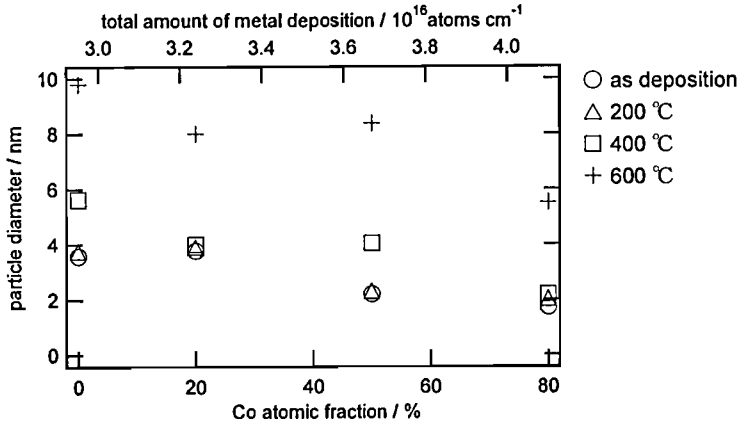

Figure 4. Variation in the mean diameter as a function of cobalt atomic fraction. Upper axis indicates the total amount of deposited metal atoms. Note that the total deposition thickness is same in each system.

the total atomic amount of deposition was different in each sample in order to have the same volume fraction of metal layer (5 vol.%). The variation of the mean particle size with the total amount of deposition is shown in Figure 4. It should be noted that the mean particle size increased with decreasing the total atomic amount of deposition. This unexpected behavior would be speculated based on the difference in the surface diffusion coefficients of gold and cobalt atoms on the PAN surface. The mobility of Au and Co adatom is different because of the difference in the interaction with the PAN molecule. If we assume that cobalt adatoms interact with PAN molecule more strongly, surface diffusion of Co adatom would be suppressed, and the particle growth cauesd by the collision between diffusing atoms or clusters.

The crystal structure of co-evaporated gold/cobalt alloy nanoparticles was examined by SAED analyis. SAED patterns of as-deposited samples were shown in Figure 5. In the present study, the *d*-spacing of crystalline gold thin film measured by electron and X-ray diffractions were used for the calibration of the diffraction patterns obtained for each sample. The SAED patterns obtained in this study were all assigned to the face-centered-cubic (fcc) crystal structure. With the increase in the atomic fraction of cobalt, the diffraction peak of $fcc_{(111)}$ plane was broadened, along with

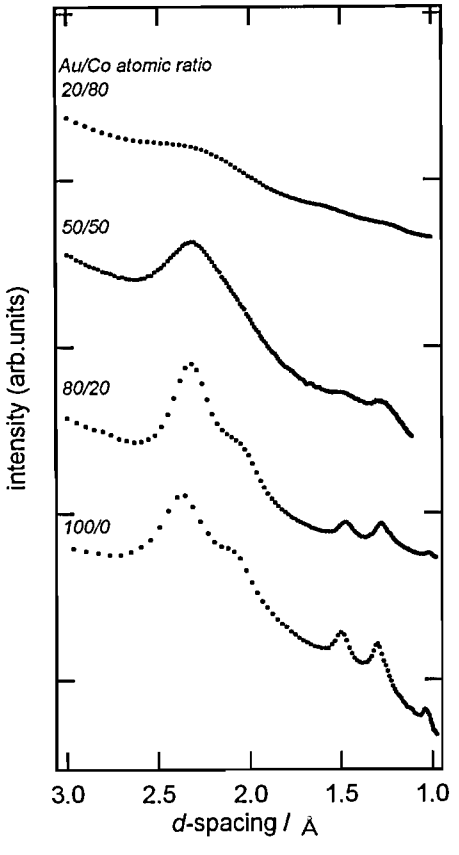

Figure 5. (b) SAED patterns of as-deposited sample containing alloy nanoparticles with different atomic ratio.

the slight shift toward small d-spacing side due to the substitution of gold atoms with smaller cobalt atoms. These results reveal that the crystal structure of gold/cobalt alloy nanoparticles is fcc even with the cobalt fraction of 80 %, despite that the crystal structure of bulk cobalt is hcp.

Changes in the SAED patterns with a heat treatment for the sample with Au/Co=5/5 are shown in Figure 6. The SAED pattern for the sample after the heat-treatment at 200 ℃ showed no significant changes compared with that of the as-deposited sample, of which the lattice constant is almost identical with that of bulk-Au. On the other hands, the peak position shifted with the heat treatment above 400 ℃ for lower *d*-spacing. The lattice parameter for binary alloys can be estimated based on the following equation, Vegard's rule, although slight deviation from the experimental data is sometimes observed [10].

$$a_{alloy} = c_1 a_1 + c_2 a_2 \qquad (1)$$

where a_{alloy} is the lattice constant for resulting alloy, c_1 and c_2 the atomic ratio for metal 1 and metal 2, and a_1, a_2 the lattice constant for pure metal 1 and metal 2. By using parameters of bulk gold (a = 4.078 Å) and fcc-cobalt (a = 3.545 Å), and the composition of c_1=c_2=0.5, we obtain the lattice parameter of the resultant solid solution of $Au_{50}Co_{50}$ 3.812 Å . Assuming that the crystal structure of gold/cobalt alloy nanoparticle was fcc, d-spacing of the (111) plane was

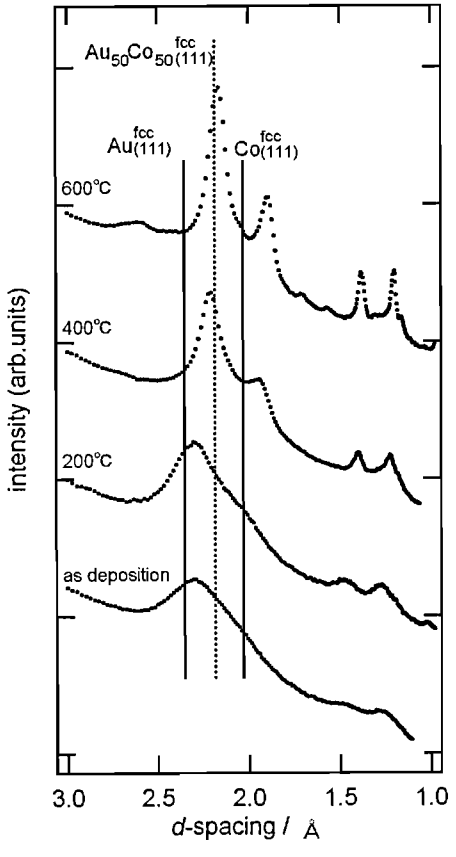

Figure 6. SAED patterns of the sample containing $Au_{50}Co_{50}$ alloy nanoparticles.

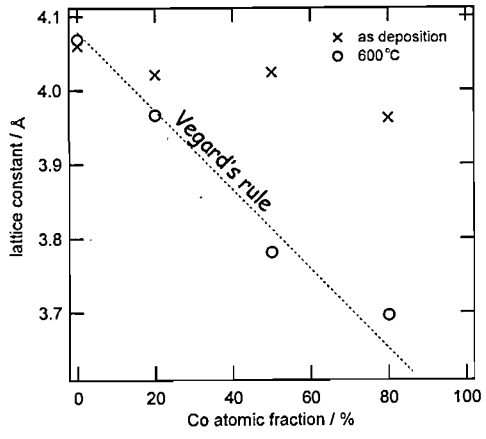

Figure 7. Variation in the lattice parameter as a function of cobalt atomic fraction. Dashed line indicates the expected lattice constant according to the Vegard's rule.

estimated as 2.201 Å from the calculated lattice constant, which is indicated by a dotted line in Figure 6. The good agreement was obtained between the peak positions of the sample after the heat-treatment at 600 ℃ and the expected position based on the Vegard's rule.

Figure 7 shows the lattice constant of as-deposited and the heat-treated sample at 600 ℃ as a function of cobalt atomic fraction, in which the expected values based on the Vegard's rule are indicated as a broken line. The lattice parameter obtained for the as-deposited sample decreases with increasing the cobalt content, indicating the substitution of smaller cobalt atom for the gold site. Nonetheless, these lattice parameters are significantly larger than the expected values. On the other hand, heat-treatment at 600 ℃ induces the modification in the crystal structure, as shown in Figure 6. By the heat-treatment at 600 ℃, the lattice parameter lowered down to the expected value for each sample with different atomic composition. It was deduced from these results that the co-evaporation of gold and cobalt produces thermodynamically metastable solid solution with fcc structure, and the following heat-treatment induces the structural relaxation and leads to their thermodynamically equilibrium state. Note that the temperature of 600 ℃ is significantly higher than the temperature that the gold/cobalt solid-solution thin film decomposes and segregates (i.e., 300 ℃). Furthermore, the diffraction lines for $L1_0$-type ordered structure were observed at 600 ℃, as indicated with arrows. Also, $L1_2$-type ordered structure was observed in the sample with Au/Co=8/2 and 2/8 after the heat-treatment at 600 ℃.

3.4Conclusion

In the present chapter, the morphology and the crystal structure of co-evaporated gold/cobalt alloy nanoparticle were investigated by using of XPS and TEM, along with SAED analysis. Co-evaporation of gold and cobalt was found to yield thermodynamically metastable solid-solution

with the crystal structure of fcc and with a particle diameter below 4 nm. Subsequent heat-treatment induces gradual structural relaxation, which results in the lowering in the lattice parameter. In addition to the disordered solid-solution, the heat-treatment at 600 ℃ induces the formation of ordered structure such as $L1_0$ and $L1_2$. All these alloy structures are not obtained in the corresponding bulk system, and these results suggest the experimental evidence that demonstrates the modification of phase diagram for the system consisting of nanometric materials.

References

[1] H. Okamoto, D. J. Chakrabarti, D. E. Laughlin, T. B. Massalski, Phase Diagrams of Binary Gold Alloys, Monograph Series on Alloy Phase Diagrams, ASM International T. M. Metals Park, Ohio, 1987.

[2] Ph. Buffat, and J.-P. Borel, *Phys. Rev. A* **1976**, *13*, 2287.

[3]O. Kitakami, H. Sato, Y. Shimada, F. Sato, and M. Tanaka, *Phys. Rev. B* **1997**, *56*, 13849.

[4] B. Y. Tsaur, S. S. Lau and J. W. Mayer, *Philo. Mag. B* **1981**, *44*, 95.

[5] R. E. Watoson, J. Hudis and M. L. Perlman, *Phys. Rev. B* **1971**, *4*, 4139.

[6] C. C. Tyson, A. Bzowski, P. Kristof, M. Kuhn, R. Sammynaiken and T. K. Sham, *Phys. Rev. B* **1992**, *45*, 8924.

[7] A. Bzowski and T. K. Sham, *J. Vac. Sci. Technol. A* **1992**, *11*, 2153

[8] M. Kuhn, R. Sammynaiken and T. K. Sham, *Physica B* **1998**, *252*,114.

[9] M. S. Kunz, K. R. Shull and A. J. Kellock, *J. Colloid Interface Sci.* **1993**, *156*, 240

[10] B. D. Cullity, Elements of X-Ray Diffraction, Addison-Welsley Publishing Company, Inc., 1978

Chapter 4

Tunneling Magnetoresistance in Gold/Cobalt alloy Nanoparticles

4.1 Introduction

Since the discovery of giant magnetresistance (GMR) in several metallic nanoarchitectures, many researches to gain insight into the fundamental and technological aspect of magnetoresistance (MR) phonemenon have been reported [1-3]. The fundamental mechanism to bring out MR effect is based on the spin-dependent transport of conduction electrons, and thus the electrical resistivity is controllable by changing the spin moment of the electrodes from and into which the conduction electron transfers. In the case of the composites consisting of insulating matrix and metal nanoparticles that is embedded in the matrix, electrons transport would be done by tunneling. If we assume that two adjacent nanoparticles possesses opposite spin moment, the tunneling probability is suppressed in comparison with the case that the spin moments are parallel; this is tunneling magnetoresistance (TMR). Several examples have been reported concerning TMR behavior in the system of Ni-Si-O [4,5], Co-Si-O [6], Fe-Hf-O [7], Fe-Mg-F [8]. In addition, TMR has been observed in the system consisting of three sandwiched structure; ferromagnetic metal / insulator / ferromagnetic metal [9-12]. For both cases, tunneling probability depends on the relative angle between two magnetization angle of the two electrodes.Theoretical treatment have been done for the first time by Maekawa and Gäfvert [9]. Their results indicate that the relative tunneling conductance ratio, which is nearly equal to the magnetoresistance ratio, can be expressed as:

$$R_{MR} = \frac{G_{AP}^{-1} - G_{P}^{-1}}{G_{AP}^{-1}} = \frac{2P_A P_B}{1 + P_A P_B}$$

$$P_\xi = \frac{D_{\xi\uparrow} - D_{\xi\downarrow}}{D_{\xi\uparrow} + D_{\xi\downarrow}}, \quad (\xi = A, B)$$

where R_{MR} is the MR ratio, G the conductance, the subscript P and AP indicate the parallel and anti-parallel arrangement of the magnetization vectors for the magnetic layers or granules, P_ξ the polarizability, $D_{\xi\uparrow}$ and $D_{\xi\downarrow}$ are the density of states of the majority and minority spin electrons of metallic layers or nanoparticles A (B) at the Fermi surface.

In the previous chapter, it was found that the co-evaporation of gold and cobalt yielded alloy nanoparticles with fcc structure. Since the particle diameter was below 10 nm, each nanoparticle exhibits superparamagnetic nature, and thus it would be possible to manipulate the magnetic

moment of each nanoparticle by applying the magnetic field. In the present chapter, the MR behavior of as-deposited gold/cobalt alloy nanoparticles was examined. Of course this is the first report on the TMR nature of gold/cobalt alloy nanoparticles, and the composition dependence were also explored.

4.2Experimental

PAN and metal layer were vapor deposited onto a glass substrate pre-deposited with an aluminum electrode with a gap of 0.1 mm and a thickness of 150 nm. The deposition procedure and the following heat-treatment were carried out in the same protocol in the previous Chapters. The dc current-voltage (I-V) measurements were carried out in a two terminal configuration by using Advantest TR8652 digital electrometer at room temperature. Temperature dependence of the electrical resistivity was examined with closed-cycle type He cryostat (Iwatani Cryomini) in the temperature range of 300 to 75 K. To investigate the MR characteristic, hand-made cell was used to be inserted into electromagnets.

4.3Results and Discussion

4.3.1 Temperature dependence of the electrical resistivity

The I-V characteristics for the films with Au/Co=5/5 are shown in Figure 1. The sample heat-treated at higher temperature exhibited lower electrical resistivity, which is due to the structural change of the matrix from polymeric PAN into carbon with the heat-treatment. Figure 1(b) displays the I-V curve for the sample after the heat-treatment at 400 ℃ plotted with normal axis, and the curve clearly deviates from the ohmic linear relation. This deviation indicates that the continuous conduction path has been broken down by the existence of the insulating layer between the alloy nanoparticles and that the electron tunneling or hopping are the possible transport mechanism. In order to gain insight in the the conduction mechanism, several plots were examined; $\log\rho$ versus $T^{-1/4}$, $\log\rho$ versus $T^{-1/2}$, and $\log\rho$ versus T^{-1}, which represent the variable range hopping conductance in amorphous semiconductors [13], tunneling conductance in insulating granular system, and semiconductor-type conductance in crystalline semiconductors, respectively. The most favorable linear relation was obtained for $\log\rho$ versus $T^{-1/2}$ plot, and the result was shown in Figure 2.

The relation of $\log\rho$ versus $T^{-1/2}$ was first derived by Sheng et al. by taking into account the tunneling and thermal avtivation process for electrical conductance in the insulating granular system [14,15]. In this system, the tunnel conductance is proportional to $\exp\{-2(2\pi/h)(2m\phi)^{1/2}s\}$, where h is the Plank constant, m the effective electron mass, ϕ the effective barrier height, and s

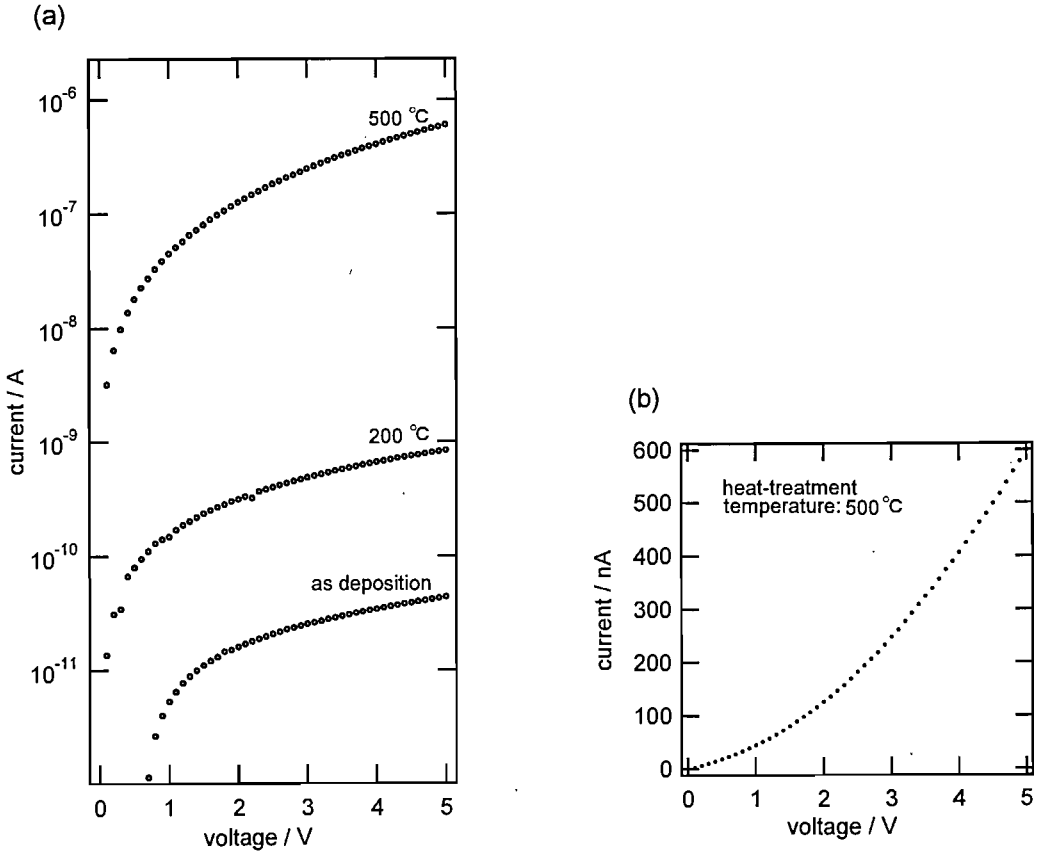

Figure 1. (a) I-V plots for the sample containing $Au_{50}Co_{50}$ nanoparticles before and after the heat-treatment. (b) I-V plot for the sample after the heat-treatment at 500 ℃ with normal axis.

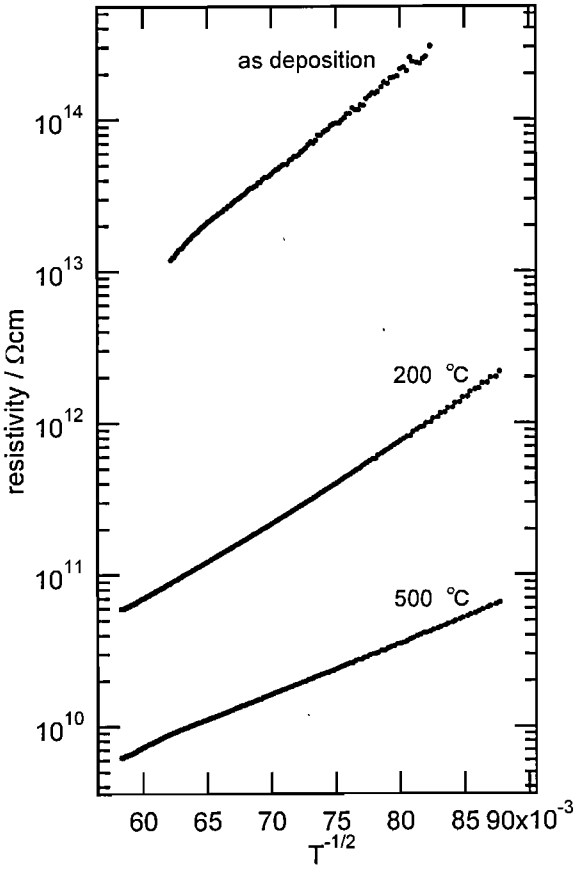

Figure 2. Temperature dependence of the electrical resistivity for the sample containing gold/cobalt alloy nanoparticles with the atomic ratio of Au/Co=5/5.

the barrier width. In addition, the breakdown of charge neutrality in the alloy nanoparticles associated with tunneling should be taken into account. The tunneling of the electrons from particle to particle leads to breakdown of the charge neutrality of the particle, resulting in an increase in the Coulomb energies of the particles of interest. Sheng et al. assumed that the probability associated with this process is proportional to $\exp\{E_c/2k_BT\}$, where E_c is the Coulomb energy increased by tunneling, k_B the Boltzmann constant, T the absolute temperature, and calculated the electrical resistivity by taking into account these two mechanisms represented in the following formula:

$$\rho = \rho \exp\{2(C/k_B)^{1/2}T^{1/2}\} \qquad (1)$$

where C is the tunnel activation energy ($=(2\pi/h)(2m\phi)^{1/2}sE_c$). This formula can be rewritten as

$$\log \rho = 2(C/k_B)^{1/2}T^{1/2} + \text{const.} \qquad (2)$$

This formula explains the linear relationship in Figure 2, in which the tunneling activation energy can be obtained from the gradient, and the results are shown in Table 1. The tunnel activation energy decreased from 0.508 eV for as-deposited sample down to 0.133 eV for the sample after the heat-traetment at 400 ℃. The variables in the tunnel activation energy are the effective barrier height, the barrier width and the Coulomb energy. Although the exact magnitude of the effective barrier height is unknown, it would be reduced due to the structural change from PAN to carbon. On the other hand, the effective barrier width would increase by the heat-treatment due to the dispersion of the alloy nanoparticles into the matrix layer, resulting in the increase in the inter-partice distance. Coulomb energy, which is reciprocally proportional to the particle diameter, would decrease with the heat-treatment because of the particle growth. Among these parameter, the factor that reduces the activation energy would be the effective barrier height and the Coulomb energy.

Table 1. Variation in the tunneling activation energy with heat-treatment.

temperature / ℃	activation energy/ eV
———	0.508
200	0.316
400	0.133

3.3.2 Applied magnetic field dependence of the electrical resistivity

The magnetic field dependences up to 1000 mT were shown in Figure 3, in which the measurement was done only for the as-deposited sample. Here, MR ratio is defined as follow:

$$MR = \frac{\rho(\mu_0 H) - \rho(\mu_0 H = 0)}{\rho(\mu_0 H = 0)} \times 100 \quad (3)$$

$\rho(\mu_0 H)$ and $\rho(\mu_0 H = 0)$ are resistivities with and without the applied magnetic field, respectively. The resistivity changed by only a few percents under the applied magnetic field, excepting for the sample with the atomic fraction of Au/Co=2/8. For the sample with Au/Co=8/2 and 10/0 did not show any dependence on the applied magnetic field, indicating that the averaged magnetic moment per atom was almost zero, which is consisted with the report by McGuire et. al [16]. The highest MR ratio observed in this study is ca. 80% at room temperature for the sample with Au/Co=2/8.

For tunnel-type MR, the tunnel conductance depends on the relative angle between the magnetization vectors of the magnetic particles. In a sandwich-type tunnel junction, the change in

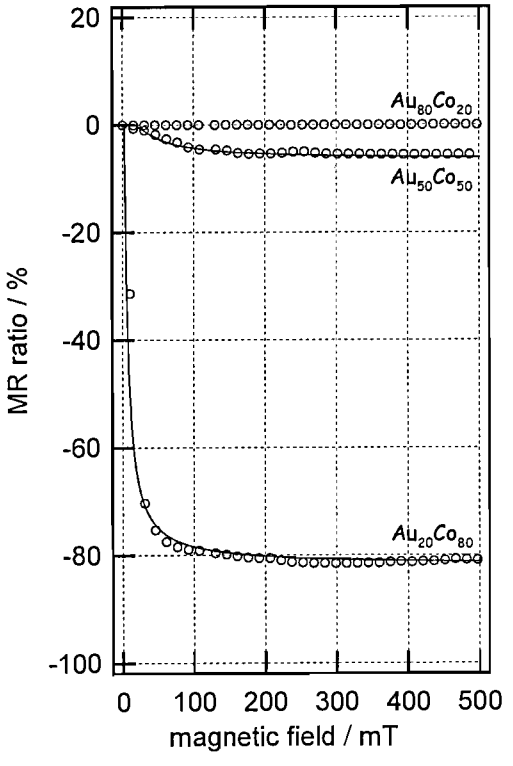

Figure 3. Variation i n the resistivity as a function of the applied magnetic field, MR ratio, for as-deposited sample containing gold/cobalt alloy nanoparticles with different atomic ratio.

the resistivity by the applied magnetic field is expressed by the relative angle (θ_{12}) between the magnetization vectors as

$$(\rho - \rho_s) \propto (1-\cos\theta_{12}) \qquad (4)$$

where, θ_{12} is a function of the applied field and ρ_s is ρ at $\theta_{12} = 0$ [9,10]. In the case for an assembly of nano-sized sandwich-type tunnel junctions, similar calculation by accounting for all combination of local junctions can be done as:

$$\begin{aligned}(\rho-\rho_S) &\propto (1-\cos\theta_{ij}) \\ &= \langle 1-\cos(\theta_i-\theta_j)\rangle_{ij} \\ &= 1-\langle\cos\theta_i\rangle_i^2 \\ &= 1-\left(M/M_S\right)^2 \qquad (5)\end{aligned}$$

where ρ_s is ρ in the nearly parallel arrangement of magnetization vectors, θ_{ij} is the relative angle of magnetization vectors between the nearest *i*th and *j*th nanoparticles, and θ_i and θ_j the direction of the magnetization vectors for the *i*th and *j*th magnetic nanoparticles. $<>_{ij}$ indicates the average for all of the nearest neighbor *i-j* pairs. For the superparamagnetic materials, the magnetization obeys Langevin function, L(*x*), which is

$$L(x) = \coth(x) - 1/x \qquad (6)$$

If the number of the magnetic particles with magnetic moment *m* was N in a unit volume, the magnetization can be expressed for the superparamagnetic materials as:

$$M = NmL(mH/k_BT) \qquad (7)$$

where *H* is the applied magnetic field, k_B the Boltzmann constant, *T* absolute temperature. Using equations (6) and (7), the relative magnetization M/M_s is written as:

$$M/M_s = L(mH/k_BT) / L(mH_s/k_BT) \quad (8)$$

H_s is the applied magnetic field where all of the magnetic vectors arrange parallel. From equations (5) and (8), the tunnel-type MR ratio can be expressed as a function of applied magnetic field,

$$\begin{aligned}\text{MR ratio} &\propto -(M/M_s) \\ &= -L(mH/k_BT) / L(mH_s/k_BT) \qquad (9)\end{aligned}$$

Satisfactory fits of this relationship to the experimental results were obtained as shown in Figure 3 as solid lines for the sample with the composition of $Au_{50}Co_{50}$ and $Au_{20}Co_{80}$, suggesting that the alloy nanoparticles present in the sample is superparamagnetic, which has already been expected based on the size of these nanoparticles (< 10 nm).

4.4Conclusion

The mechanism for the electrical conductance was confirmed to be governed by the electron tunneling between the alloy nanoparticles from the results of temperature dependence of the electrical resistivity. From the magnetic field dependence on the electrical resistivity, alloy nanoparticles with the cobalt fraction above 50 % were found to be capable of exhibiting spin-selective tunneling, and the highest selectivity was obtained for the sample containing $Au_{20}Co_{80}$. Based on the theoretical calculation, the alloy nanoparticles that exhibit TMR were superparamagnetic, which was also supported from the size of these nanoparticles.

References

[1] P. Grünberg, R. Schreiber, Y. Pang, M. B. Brodsky and C. H. Sowers, *Phys. Rev. Lett.* **1986**, *57*, 2442.

[2] M. N. Baibich, J. M. Broto, A. Fert, F. Nguyen Van Dau, F. Petroff, P. Eitenne, G. Creuzet, A. Friederich and J. Chazelas, *Phys. Rev. Lett.* **1988**, *61*, 2472.

[3] P. M. Levy, *Solid State Phys.* **1994**, *47*, 367.

[4] J. I. Gittleman, T. Goldstain and S. Bozowski, *Phys. Rev. B* **1971**, *5*, 3609.

[5] J. S. Helman and B. Abeles, *Phys. Rev. Lett.* **1976**, *37*, 1429.

[6] S. Barzilai, Y. Goldstein, I. Balberg and J. S. Helman, *Phys. Rev. B.* **1981**, *23*, 1809.

[7] Y. Hayakawa, N. Hasegawa, A. Makino, S. Mitani and H. Fujimori, *J. Magn. Magn. Mater.* **1996**, *154*, 175.

[8] T. Furubayashi and I. Nakatani, *J. Appl. Phys.* **1996**, *79*, 6258.

[9] S. Maekawa and U. Gäfvert, *IEEE Trans. Magn.* **1982**, *18*, 707.

[10] J. C. Slonczewski, *Phys. Rev. B.* **1989**, *39*, 6995.

[11] T. Miyazaki and N. Tezuka, *J. Magn. Magn. Mater.* **1995**, *139*, L231.

[12] J. S. Moodera, L. R. Kinder, T. M. Wong and R. Meservey, *Phys. Rev. Lett.* **1995**, *74*, 3273.

[13] S. N. Mott, Conductance in Non-Crystalline Materials, Clarendon, Oxford, **1987**, p. 27.

[14] P. Sheng, B. Abeles and Y. Arie, *Phys. Rev. Lett.* **1973**, *31*, 44.

[15] B. Abeles, P. Sheng, M. D. Coutts and Y. Arie, *Adv. Phys.* **1975**, *24*, 407.

[16] T. R. McGuire, J. A. Aboaf and E. Klolholm, *J. Appl. Phys.* **1981**, *52*, 2205.

PART II

Enhancing and Quenching Functions of Silver Nanoparticles

Chapter 5

Enhancing and Quenching Functions of Silver Nanoparticles for the Luminescent Properties of Europium Complex

5.1. Introduction

Photoactive lanthanide complexes are of both fundamental and technological interest because of their large Stokes shifts, narrow emission band widths and long emission lifetimes. Due to these characteristics, they are suitable candidates for applications as light-emitting diode (LED) [1], laser materials [2,3] and fluoroimmunoassay [4-7]. Selvin and co-workers reported that luminescent (or lanthanide-based) resonant energy transfer (LRET) can be a novel tool for measuring nanometer scale distances, both *in vitro* and *in vivo*, in which LRET relies on energy transfer from a donor lanthanide complex to an acceptor organic dye *via* a nonradiative dipole-dipole (Förster-type) interaction [8-10]. A major problem concerning the use of lanthanide complex for fluoroimmunoassay is the quenching due to a coupling with vibration modes of solvent molecules. To avoid this quenching effect, several kinds of chelating agents have been synthesized [6,11,12]. On the other hand, nanostructured metallic surfaces would be promising materials to enhance the luminescence of these lanthanide complexes. Metallic nanostructures have demonstrated a drastic increase in the intensity of Raman scattering or luminescence of ions or molecules in close proximity of the metallic surface [13]. Recent investigations of the surface enhancement effect have opened up a new methodology for high-sensitive detection such as single-molecule surface-enhanced Raman spectroscopy (SM-SERS) [14-16]. Lakowicz et al. reported the effects of silver island films on fluorescence properties of DNA, with a quantum yield of 10^{-4} to 10^{-5}, and they observed an intrinsic fluorescence from DNA without any additional label used for the conventional DNA detection method [17]. These remarkable enhancement phenomena stems from a resonant excitation of surface plasmon polaritons confined within a metallic nanostructure and a consequent enhancement in the induced dipole moment of the target molecules.

Pioneering experiments on the luminescence properties of Eu(III) ion located in close proximity to a metallic surface has been made by Drexhage [18,19] and recently by Barnes [20,21]. All these experiments were carried out by depositing Eu(III) complex onto the metallic thin films covered with an organic spacer. Nevertheless, lanthanide complexes are frequently required to be used in solution phase as luminescent labels for biological applications. In this regard, the use of metallic nanostructures in solution phase as surface-enhancers is an attractive challenge, and nano-sized metallic particles are promising candidate for this purpose. In this work, we report on

the fundamental aspects of the role of metal nanoparticles on the luminescent properties of europium complexes in solution phase using silver nanoparticles of different sizes and shapes.

5.2 Experimental

Spherical silver nanoparticles of different sizes were synthesized by reducing $AgNO_3$ with N,N-dimethylformamide (DMF) [22]. Poly(vinylpyrrolidone) (PVP) aqueous solution (10ml, 10 wt.%) was added to DMF (80ml), followed by an addition of $AgNO_3$ aqueous solution (10 ml). The mean particle diameter was tuned by changing the reaction temperature (90 ~ 110 ℃) and the concentration of $AgNO_3$ solution (0.125 ~ 0.250 M). The reaction was kept for 3 hours and the obtained dark-brownish solution was purified by centrifugation.

Preparation of rod-shaped silver nanoparticles was made according to the previously reported seed-mediated method [23]. The obtained ruby-red solution containing silver nano-rods was centrifuged and precipitates were dissolved to PVP aqueous solution (10 wt.%), and kept at 30 ℃ for 1 hour. This solution was again centrifuged, precipitates were dissolved into a PVP-DMF solution (10 wt.%) and kept at 30 ℃ for 1 hour. To remove excess PVP molecules, purification was made by centrifugation.

The morphology and size distribution of silver nanoparticles were obtained by transmission electron microscope (TEM, JEOL JEM-2010, 200 keV). Optical absorption spectra were measured with a U-3300 spectrophotometer (HITACHI) by using of 10 mm optical path length quartz cuvette. Ag nanoparticle concentration was estimated by using Ag atomic concentration in the sample solution (obtained by ICP-AES, Seiko Instruments Inc., SRS 1500VR), the average diameter of each sample (from TEM observation, see Figure 2) and the bulk density of silver (10.50 g/cm3). Luminescence measurements were performed using a FP-6500 spectrofluorometer (JASCO) with 90° configuration. The samples for the optical measurements were prepared by mixing the complex solution and the particle solution with keeping the final concentration of Eu(III) ion at 250 μM.

5.3 Results and discussion

5.3.1 morphology and optical properties of spherical and rod-shaped silver nanoparticles

Figure 1 shows typical time sequence of TEM images of silver nanoparticls with different heating duration, and the corresponding diameter distributions are displayed in Figure 2. Even after 1 min, small silver nanoparticles with a diameter below 10 nm were already formed. They grow in size with increasing the heating time and reaches their equilibrium diameter at around 180 min.

Along with the growth in the particle size, optical absorption spectrum changes with time

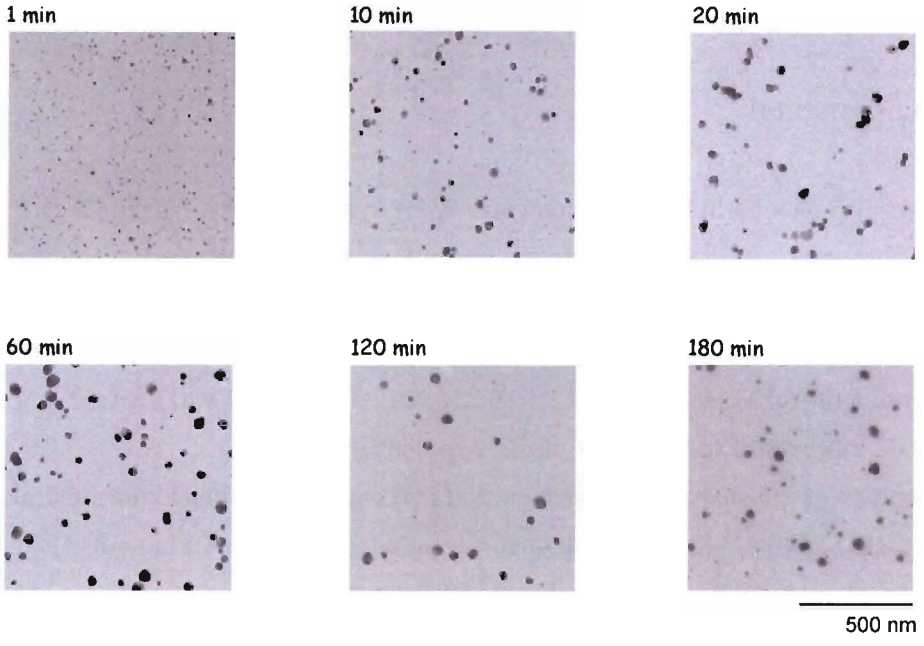

Figure 1. Typical time sequence of the molphology of silver nanoparticles prepared by DMF reduction of silver nitrate in the presence of PVP.

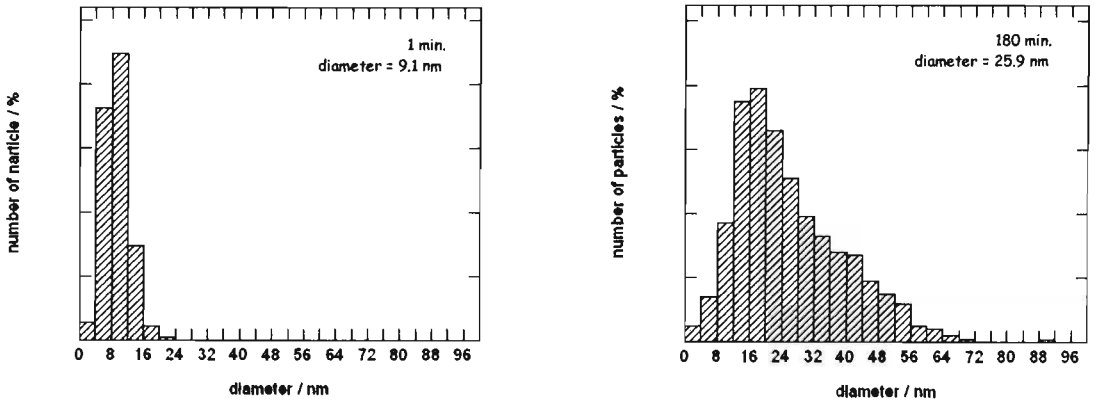

Figure 2. Particle size distribution histograms of silver nanoparticles after the reaction of 1 min and 180 min.

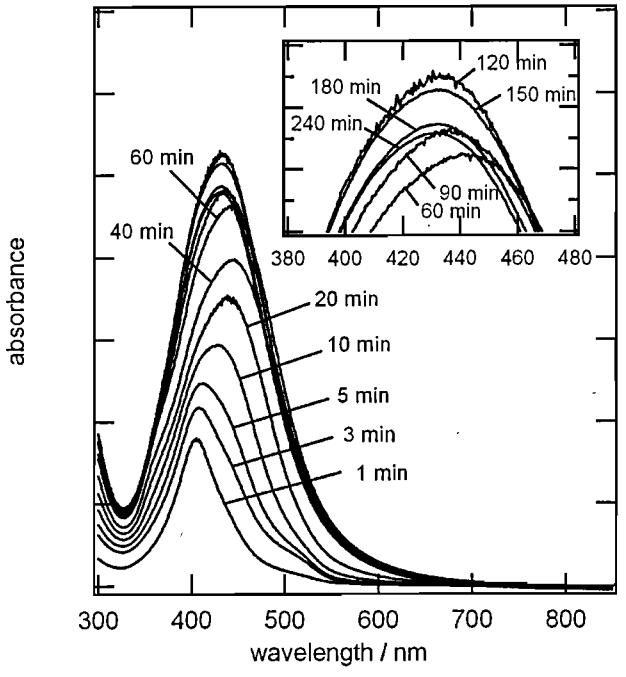

Figure 3. Variation in the optical absorption spectrum during the reduction reaction. (inset) The enlargement in the region containing the absorption peak region from 60 min to 240 min.

(Figure 3). The continuous increase in absorbance with time would indicate the increase in both the number and the diameter of silver nanoparticles and the slight shift in the peak wavelength would correspond to the change in their diameter. A small shoulder around 520 nm that is observed only for the sample after 3 and 5 min suggests the formation of the nanoparticle aggregation, which was disappeared with time possibly due to the coalescence. Unexpectedly, both absorbance and the peak wavelength does not show monotonous changes, i.e., absorbance increased from 1 min to 120 min and then decreased, and peak wavelength shifted forward first longer wavelength and then blue-shifted. These variations with time are plotted as a function of the heating time in Figure 4 along with the change in the diameter. It was found that the change in the peak wavelength synchronized with the change in the particle diameter, and not correlated with the change in the absorbance. Although the reason for that these parameters exhibited such complicated behavior is still unclear, the sample heated for 180 min was used for the following experiment, because further heating does not bring any distinct changes in these parameters.

The diameter of the spherical silver nanoparticle was found to be tunable by changing the heating temperature and the concentration of the seeding silver nitrate solution, and three samples with different diameter were prepared (Figure 5A-C). With increasing the particle diameter, the corresponding size distribution profile and the optical absorption spectrum broadened. Especially for the sample with the largest diameter, bimodal distribution profile and the optical absorption spectrum were observed. In addition to spherical silver nanoparticles, morphology, corresponding

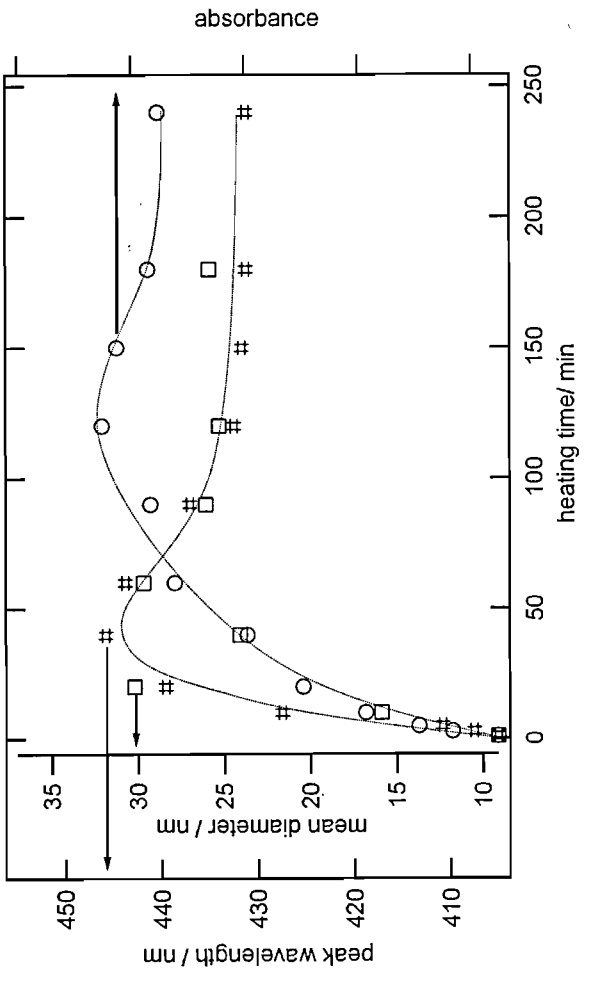

Figure 4. Variations in the absorption peak wavelength, particle mean diameter, and absorbance at the peak wavelength as a function of the heating time.

(A) TEM image

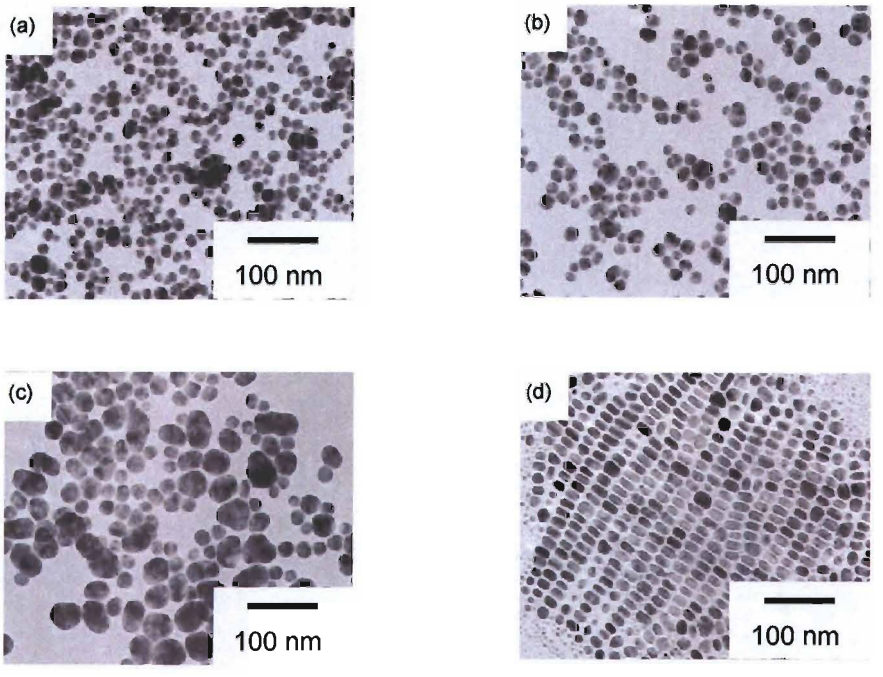

(B) size distribution

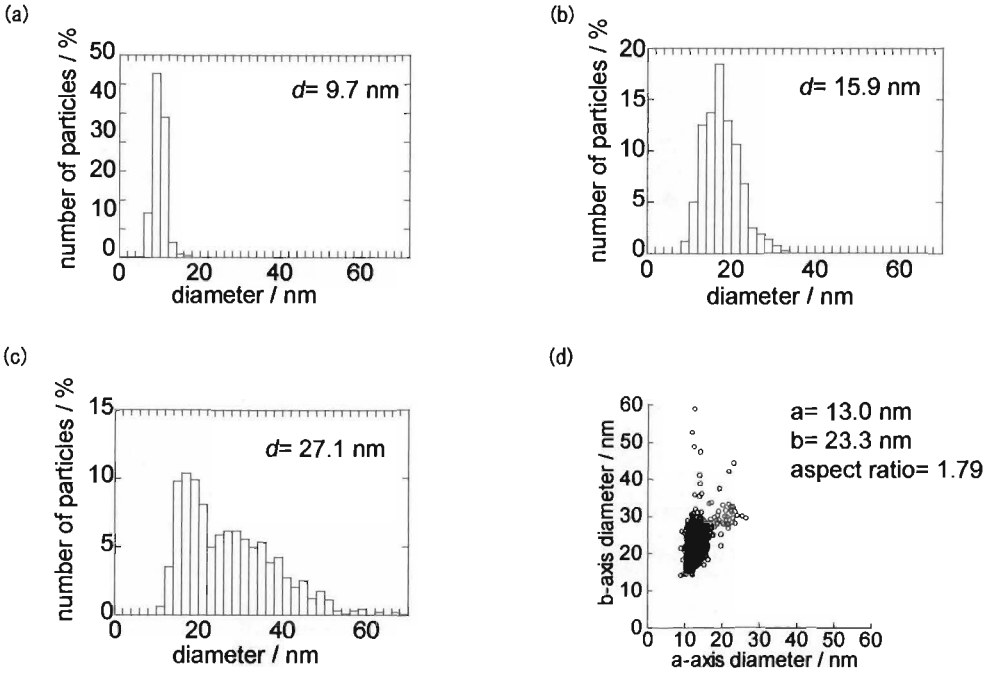

Figure 5. (A) TEM images, (B) size distributions, and (C) optical absorption spectra of (a)-(c) shperical and (d) rod-shaped silvre nanopaticles. a-axis and b-axis in the distribution histogram of rod-shaped sample indicate short-axis and long-axis of the nano-rod, respectively. Heating temperature and the concentration of the seeding silver nitrate solution are (a) 90℃, 0.125 M; (b) 90℃, 0.250 M; (c)110℃, 0.250 M.

(C) optical absorption spectrum

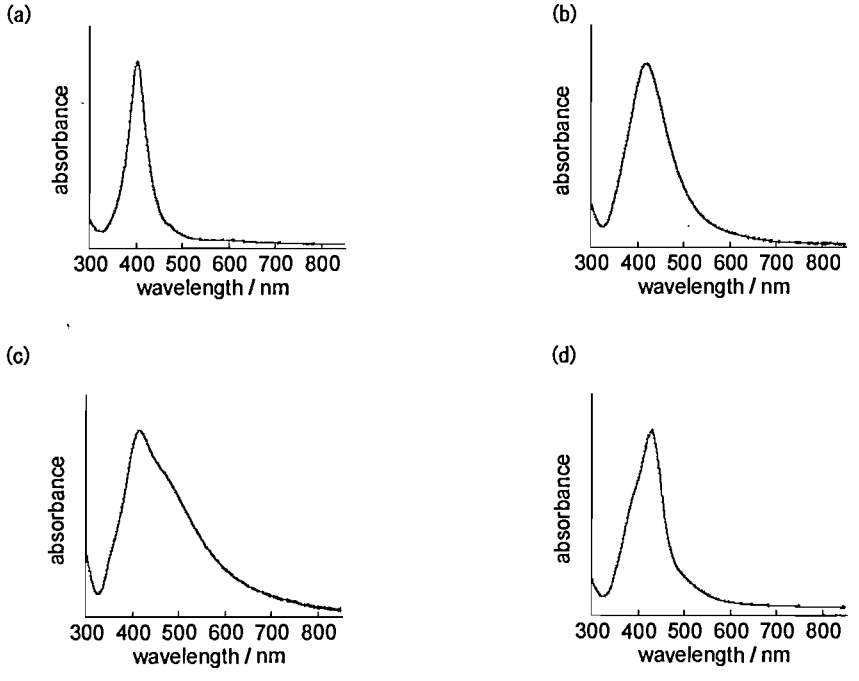

Figure 5. (continued).

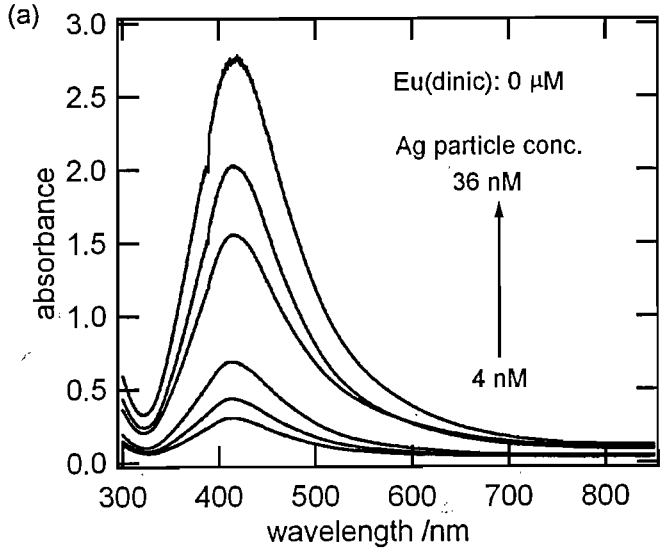

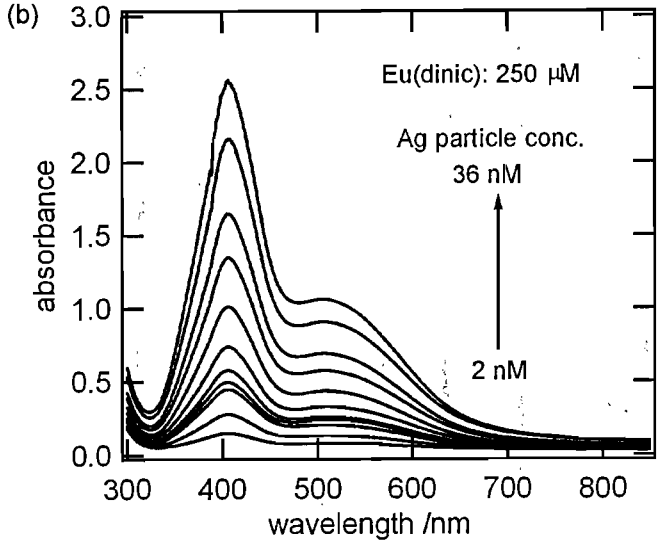

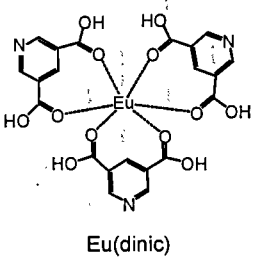

Eu(dinic)

Figure 6. Optical absorption spectra of DMF solution containing silver spherical nanoparticle with the diameter of 15.9 nm (a) without and (b) with Eu(dinic) complex. Only the solution containing Eu(dinic) complex exhibited an additional absorption band at around 550 nm.

size distribution, and optical absorption spectrum of rod-shaped silver nanoparticles are also included in Figure 5D. Silver nano-rod prepared in the present study has an average short-axis diameter of 13.0 nm and long-axis diameter of 23.3 nm; the aspect ratio is 1.79. Rod-shaped nanoparticles are known to exhibit two distinct absorption maxima corresponding to transverse and longitudinal modes of a localized surface plasmon resonance [24]. However, the absorption spectrum of the rod-shaped sample shows a single peak at 428 nm, along with a small shoulder around 400 nm because of the small aspect ratio. Upon mixing with the europium complex Eu(dinic) solution, the color of the solution immediately changed to pinkish red, accompanying the appearance of a new absorption or scattering band around 500-550 nm (Figure 6). The appearance of the new band at longer wavelength region indicates the formation of particle aggregates in the solution [25]. No color or spectral change was observed when only either dinic ligands or europium ions were added into the particle solution, indicating the function of Eu(dinic) complexes as linker molecules, and the complexes are expected to be incorporated in the particle aggregates. Figure 7 displays the change in the absorption spectrum of silver nanoparticle solution with the addition of the different concentration of the complex solution. With increasing the complex concentration, the main absorption band at 300-500 nm dicreased and at the same time the aggregation band at 500-600 nm became evident.Changes in the absorbance at each band as a function of the complex concentration are plotted in the inset. Although the peak position of the

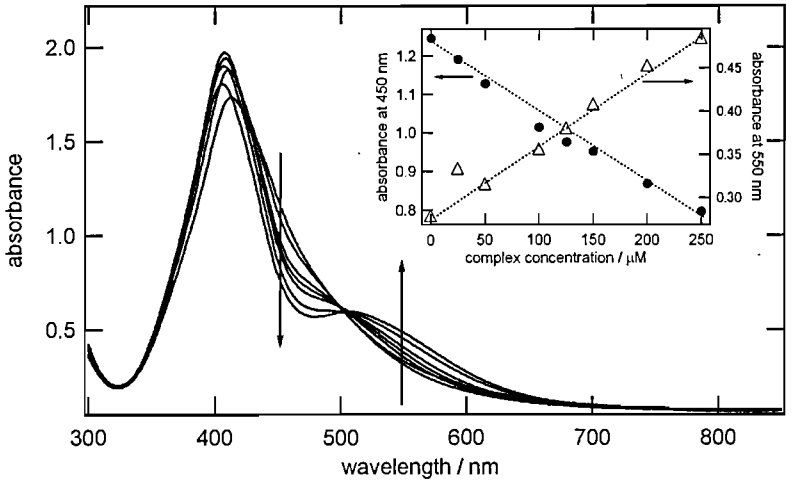

Figure 7. Changes in the absorption spectrum of silver nanoparticle solution with the addition of Eu(dinic) solution. The concentration of silver nanoparticle is 25 nM, and Eu(dinic) concentration increases from 0 to 250 μM. (inset) Plot of absorbance at main plasmon band and aggregation band as a function of Eu(dinic) concentration.

main plasmon band is not stable, the presence of the isosbestic point at 500 nm support the existence of two species in the solution that is distinguishable in the absorption spectrum, i.e., the presence of free nanoparticles and the aggregated nanoparticles.

5.3.2 luminescent properties of Eu(dinic) complex

Figure 8 displays optical properties of dinic and europium ion separately dissolved in DMF. The DMF solution containing only dinic shows broad emission band centered at 370 nm and the corresponding excitation maximum at 276 nm. The excitation spectrum of europium (III) ion dissolved in DMF was obtained by monitoring $^5D_0 \rightarrow {}^7F_2$ transition at 616 nm, in which several sharp bands characteristic of the *f-f* transitions of europium (III) ion were observed and the most intense excitation band at 394 nm was assigned to $^7F_0 \rightarrow {}^5L_6$ transition. From dinic emission and europim (III) ion excitation spectra, an overlap between them in the wavelength region from 350 nm to 400 nm is evident. There are two possible mechanism that allow the energy transfer from ligand to the central metal ion; Dexter resonant exchange mechanism [26] and Förster model [27]. In the former mechanism assume the energy transfer from the excited triplet state of the ligand to the metal ion, and in this case the triplet state of the ligand should be energetically higher than the resonant state of the europium ion by several thousands cm^{-1} in order to achieve an effective irreversible energy transfer form the ligand to the metal ion. On the other hand, Förster model suggests that the overlap between emission of ligand and absorption of Eu (III) ion is enough to induce energy transfer between them, suggesting that the energy transfer from dinic to

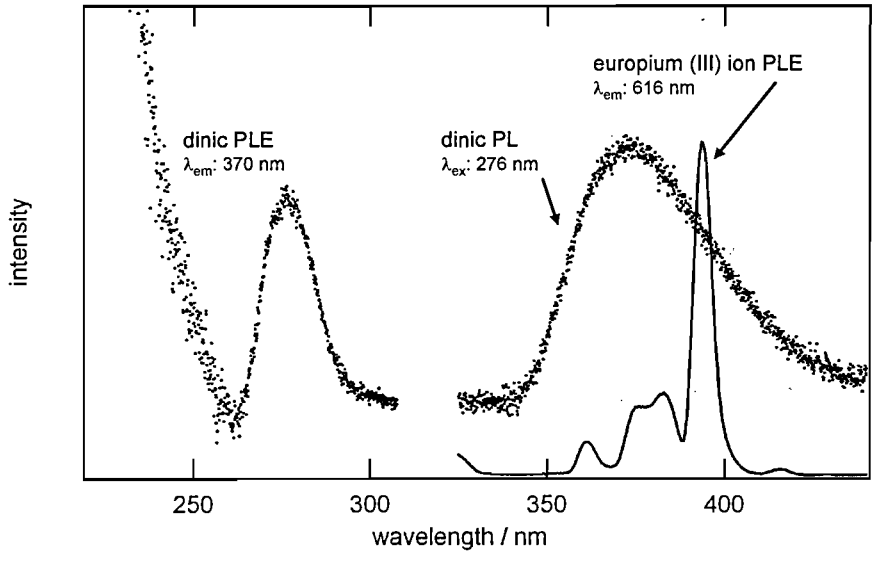

Figure 8. Photoluminescence (PL) and excitation (PLE) spectra of dinic and europium (III) ion separately dissolved in DMF.

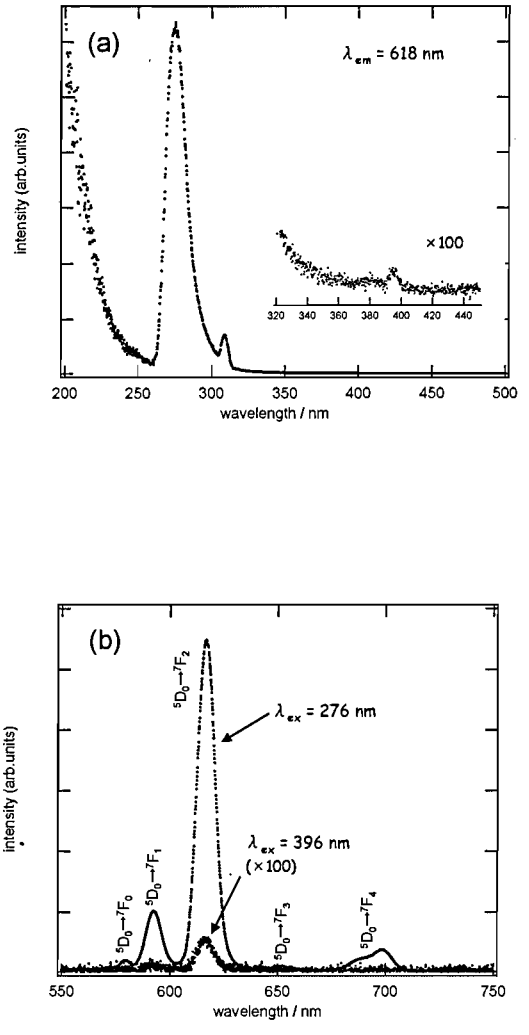

Figure 9. (a) Excitation and (b) emission spectra of Eu(dinic) complex dissolved in DMF. Notations for each peak in (b) denote the assignment of the electronic transition of europium (III) ion.

europium ion is expected in the present system. The excitation spectrum of Eu(dinic) complex dissolved in DMF was also obtained by monitoring $^5D_0 \rightarrow {}^7F_2$ transition at 616 nm (Figure 9a), in which an asymmetric peak at around 275 nm and small peak at 394 nm ($^7F_0 \rightarrow {}^5L_6$ transition) were observed. The asymmetric peak observed at 275 nm is attributable to the excitation of dinic ligand. From these results, an effective energy transfer from dinic ligand to the central europium (III) ion is evident, and actually, higher emission intensity was observed by 276 nm excitation than by 396 nm excitation (Figure 9b).

5.3.3 Effect of silver nanoparticles on the luminescent properties of europium complex

The particle concentration dependence on the emission intensity of the complexes is illustrated in Figure 10, in which the intensity is normalized with the intensity in the absence of Ag nanoparticles (0 nM). Luminescent intensity first increases and then decreases with increasing the particle concentration, and each sample show different maximum enhancement factor and the particle concentration at which the intensity reaches the maximum. It can be deduced from this concentration dependence that the silver nanoparticles act as both an enhancer and a quencher for europium luminescence, because the luminescent intensity should decrease monotonously when the metal nanoparticles serve as only the quencher [28]. The obtained maximum enhancement factor for each sample is thus regarded as the result of a delicate balance between the enhancement and the quenching effect. The enhancement effect is known to be strongly affected by the size and symmetry of the metallic nanostructure [29], and a comprehensive expression considering both the enhancing and the quenching effects will give detailed information for the particle concentration dependence, including the quantitative treatment for the enhancement factor and the concentration

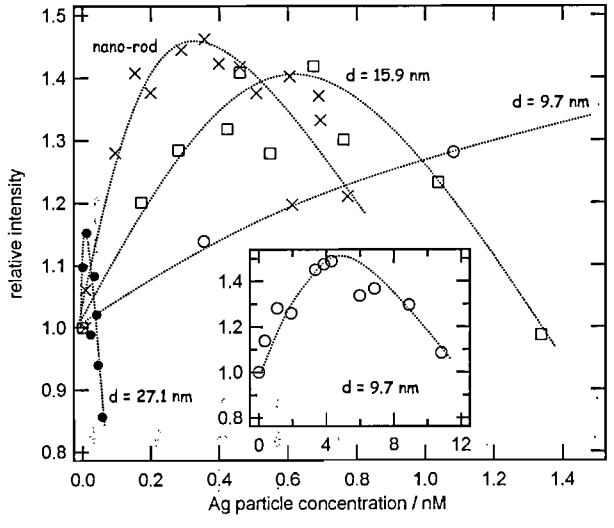

Figure 10. Silver nanoparticle concentration dependence of the luminescent intensity of Eu(dinic), in which the intensity is normalized with the intensity in the absence of silver nanoparticles (0 nM).

that exhibits the maximum enhancement of each sample.

In addition to the changes in the luminescent intensity with the particle addition, we found another effect arising from the addition of Ag nanoparticles. Figure 11 shows the variation in asymmetric ratio (AS) with the particle concentration, where AS is defined as the integrated emission intensity ratio between $^5D_0 \rightarrow {}^7F_1$ (magnetic dipole transition) and $^5D_0 \rightarrow {}^7F_2$ (electric dipole transition) transitions, $AS = \int I_{^5D_0 \rightarrow {}^7F_2}(\omega)d\omega \Big/ \int I_{^5D_0 \rightarrow {}^7F_1}(\omega)d\omega$. A variation in the AS value describes two effects of the nanoparticle addition, that is, modifications of ligand field and refractive index around europium ions. The increasing tendency in AS values with the particle addition indicates the increase in the distortion of the ligand field arising from the interaction with silver nanoparticles during the aggregate formation [30]. The effect of refractive index modification is explained on the basis of the local field effect, which gives the refractive index dependence of the electric dipole transition rate [31-33]. The macroscopic variation in the refractive index upon particle addition is almost negligible according to the Maxwell-Garnett (MG) effective medium expression, because of quite a low volume fraction of Ag nanoparticles (~ 10^{-6}). [34] However, considering that the Eu(dinic) complexes exist in close proximity of Ag nanoparticles, the local refractive index around Eu(dinic) complexes would be altered different from that of bare Eu(dinic) dissolved in DMF [35,36], resulting in the modification of the electric dipole transition rate and thus the change in the AS value. It is also notable that the AS value increased monotonously with the particle concentration, unlike luminescent intensity. The monotonous increase in AS value indicates that the number of Eu(dinic) complex interacting with Ag nanoparticles is not saturated under this concentration condition, which is reasonable because the complex concentration (250 μM) is markedly higher than that of Ag nanoparticles (<10 nM).

In contrast to the present study, only the quenching effect of metal nanoparticles has been

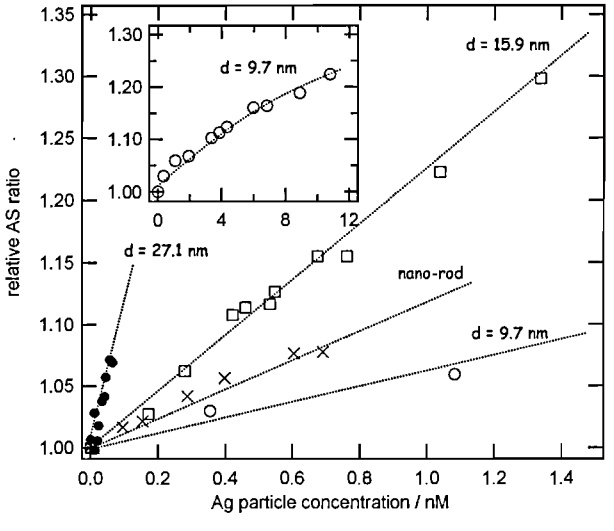

Figure 11. Silver nanoparticle concentration dependence of asymmetric ratio (AS), in which the AS value is normalized with that in the absence of silver nanoparticles (0 nM).

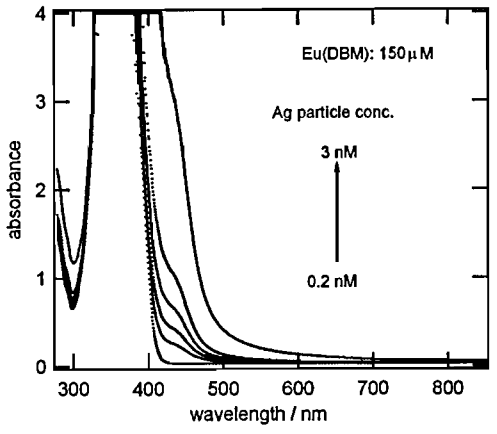

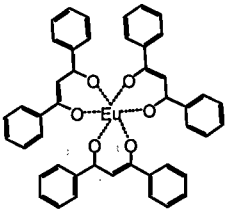

Eu(DBM)

Figure 12. Optical absorption spectra of DMF solution containing both Eu(DBM) complex and silver spherical nanoparticle with the diameter of 15.9 nm.

observed in the solution system where gold nanoparticles and semiconductor nanoparticles [37] or organic fluorophores [28] were co-dissolved. The origin of this difference is attributable to the aggregates formation ability and the difference in the metal used. The enhancement field around metallic nanostructures is strongly enhanced when two or more particles come into close proximity with each other, and the aggregate effect concerning Raman scattering has been already reported [25]. As mentioned above, Eu(dinic) complexes are expected to be incorporated into particle aggregates, and thus the fluorescent intensity was effectively enhanced in the present system. Moreover, silver is a well-established material to exhibit remarkable enhancement ability for Raman and fluorescent intensity of molecules. The effectiveness of silver for enhancement phenomenon is widely known and Lakowicz et al. observed enhanced luminescence from $[Ru(bpy)_3]^{2+}$ complexes [38], where bpy is 2,2'-bipyridyl, in the presence of silver particle islands, whereas Au nanoparticles quench the fluorescence of $[Ru(bpy)_3]^{2+}$ following the Stern-Volmer relation [39].

In order to examine the effectiveness of the aggregate formation for SEF, the control experiment was carried out, by using of Eu(DBM) complex bearing benzene ring in the ligand moiety in place of Eu(dinic) that has pyridine ring. As clearly shown in Figure 12, the addition on spherical silver nanoparticles with the average diameter of 15.9 nm into DMF solution containing Eu(DBM) complex does not result in the formation of nanoparticle aggregation, which is evident from the lack of the aggregation band. The difference in the aggregate formation ability is attributable to the ligand structure, and the plausible mechanism of the aggregate formation is illustrated in Scheme 1. The most prominent difference between two ligands is the structure of the aromatic ring placed at the outermost position of the complex, and nitrogen atom, which is present only in

Scheme 1. Chemical structures of two complexes and schematic diagram showing the possible formation mechanism of nanoparticle aggregates in nanoparticle/Eu(dinic) system. The presence of nitrogen atoms at the outermost position of the complex is important to induce the aggregate formation.

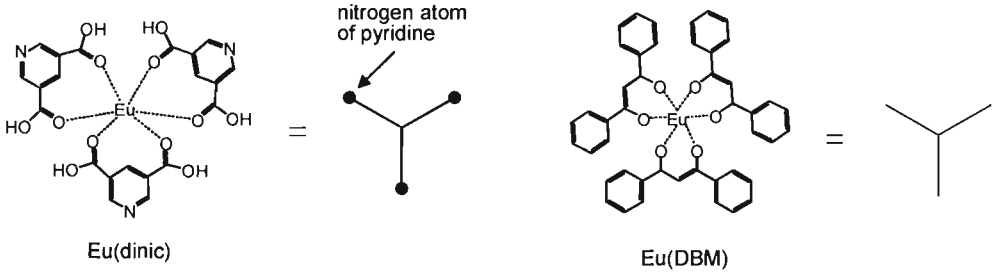

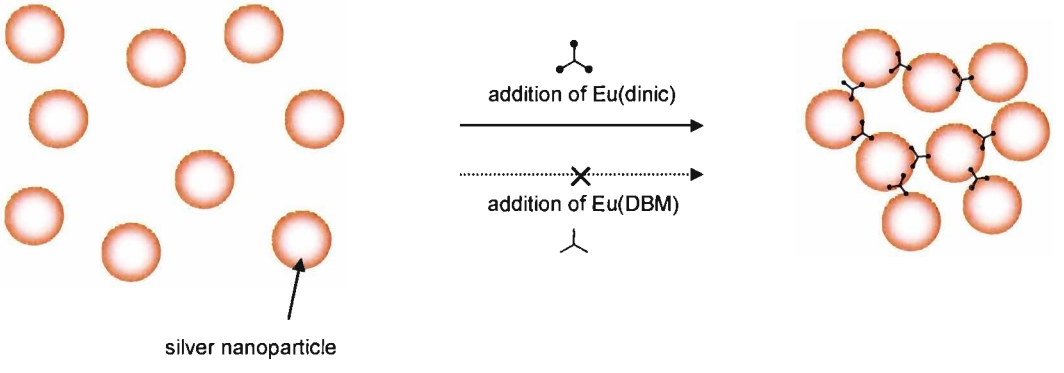

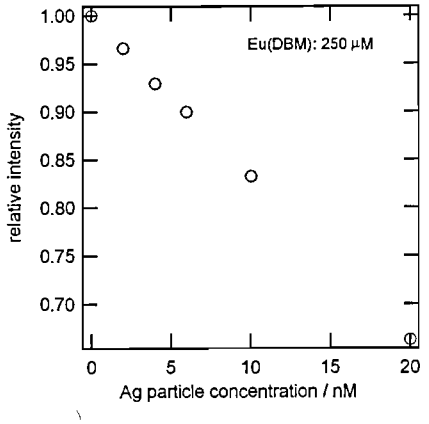

Figure 13. Silver nanoparticle concentration dependence of the luminescent intensity of Eu(DBM), in which the intensity is normalizedwith the intensity in the absence of silver nanoparticles (0 nM).

Eu(dinic) complex, is known to interact strongly with silver nanoparticle. It should be also noted that one Eu(dinic) complex has three pyridine rings (i.e., nitrogen atoms), and if two of them interact with two different silver nanoparticles, the presence of Eu(dinic) complex would results in the formation of the silver nanoparticle network.

Finally, the effect of silver nanoparticle addition on the emission properties of Eu(DBM) was examined in the same protocol with Eu(dinic) system. Figure 13 displays the relative luminescence intensity of Eu(DBM) as a function of the concentration of the added silver nanoparticles. As expected, the luminescence intensity decreased almost linearly with the concentration of silver nanoparticle, and any enhancement was not observed in the same concentration region with Eu(dinic) system. From these results, it can be concluded that the aggregate formation and the subsequent incorporation of the complex is essential to achieve SEF in the solution phase, and this is the first evident to demonstrate the enhancing ability of silver nanoparticles for emission properties in the solution system.

5.4 Conclusion

Fundamental aspects of the effects of Ag nanoparticles on the luminescent properties of europium complexes in solution phase were investigated in the present chapter. The luminescent intensity of Eu(dinic) increased in the early stage of the particle addition and then decreased by further addition. This behavior indicates the functions of the silver nanoparticles as both the surface-enhancer and the quencher in the solution phase. The observed luminescent intensity is thus regarded as the result of the delicate balance between these two functions of the silver nanoparticles, which is strongly dependent on the particle size and shape. Under our experimental conditions, smaller particles showed larger enhancement factor at higher particle concentration region, and the rod-shaped nanoparticles exhibited comparable effects with the spherical nanoparticles with a similar particle diameter. The ligand field and the refractive index around europium ions were

also altered due to the presence of the silver nanoparticles, which brought about the change in the AS value. Finally, we pointed out that the observed changes in the luminescent properties are attributable to the formation of the particle aggregates in the solution. It should be also noted that the enhanced luminescence was observed in spite of the off-resonant condition between the excitation wavelength (276 nm) and the surface plasmon (ca. 400 nm), and these findings suggest that the further luminescence enhancement of the europium complex is expected even in the solution phase by optimizing the design of both nanoparticles and complexes.

References

[1] McGehee, M. D.; Bergstedt, T.; Zhang, C.; Saab, A. P.; O'Regan, M. B.; Bazan, G. C.; Srdanov, V. I.; Heeger, A. J. *Adv. Mater.* **1999**, *11*, 1349.

[2] Sabbatine, N.; Guardigli, M.; Lehn, J. M. *Coord. Chem. Rev.* **1993**, *123*, 201.

[3] Piguet, C.; Bunzli, J. C. G..; Bernardinelli, G..; Hopfgartner, G.; Williams, A. F. *J. Am. Chem. Soc.* **1993**, *115*, 8197.

[4] Horrocks, W. DeW. Jr.; Collier, W. E. *J. Am. Chem. Soc.* **1981**, *103*, 2856.

[5] Richardson, F. S. *Chem. Rev.* **1982**, *82*, 541.

[6] Mukkala, V. M.; Helenius, M.; Hemmilä, I.; Kankare, J.; Takalo, H. *Helv. Chim. Acta* **1993**, *76*, 1361.

[7] Saha, A. K.; Kross, K.; Kloszewski, E. D.; Upson, D.A.; Toner, J. L.; Snow, R. A.; Black, C. D. V.; Desai, V. C. *J. Am. Chem. Soc.* **1993**, *115*, 11032.

[8] Selvin, P. R.; Rana, T. M.; Hearst. J. E. *J. Am. Chem. Soc.* **1994**, *116*, 6029

[9] Selvin, P. R. *IEEE J. Sel. Top. Quantum Electron.* **1996**, *2*, 1077.

[10]Selvin, P. R.; *Nature Struct. Biol.* **2000**, *7*, 730.

[11]Sueda, S.; Yuan, J.; Matsumoto, K. *Bioconj. Chem.* **2000**, *11*, 827.

[12]Galaup, C; Carrié, M.-C.; Tisnčs, P.; Picard, C. *Eur. J. Org. Chem* **2001**, 2165.

[13]Chang, R. K.; Furtak, T. E. In *Surface enhanced Raman scattering*; Plenum Press: New York, 1982.

[14]Nie, S.; Emory. S. R. *Science* **1997**, *275*, 1102

[15]Kneipp, K.; Wang, Y.; Kneipp, H.; Perelman, L. T.; Itzkan, I.; Dasari, R. R.; Feld, M. S. *Phys. Rev. Lett.* **1997**, *78*, 1667.

[16]Michaels, A. M.; Nirmal, M.; Brus, L. E. *J. Am. Chem. Soc.* **1999**, *121*, 9932.

[17]Lakowicz, J. R.; Shen, B.; Gryczynski, Z.; D'Auria, S.; Gryczynski, I. *Biochem. Biophys. Res. Commun.* **2001**, 286, 875.

[18]Drexhage, K. H. *J. Lumin.* **1970**, 1/2, 693.

[19]Drexhage, K. H. *Sci. Am.* **1970**, 222, 108.

[20]Amos, R. M.; Barnes, W. L. *Phys. Rev. B* **1999**, 59, 7708.

[21]Andrew, P.; Barnes, W. L. *Phys. Rev. B* **2001**, 125405.

[22]Pastoriza-Santos, I; Liz-Marzin, L. M. *Langmuir* **2002**, *18*, 2888.

[23]Jana, N. R.; Gearheart, L; Murphy, C. J. *Chem. Commun.* **2001**, 617.

[24]Chang, S. S.; Shih, C. W.; Chen, C. D.; Lai, W. C.; Wang, C. R. C. *Langmuir* **1999**, *15*, 701.

[25]Blatchford, C. G.; Campbell, J. R.; Creighton, J. A. *Surf. Sci.* **1982**, *120*, 435.

[26]Dexter, D. L. *Chem. Phys.* **1953**, *21*, 836.

[27]Förster, T. *Z. Naturforsch* **1949**, *4a*, 321.

[28]Aguila, A.; Murray, R. W. *Langmuir* **2000**, *16*, 5949.

[29]Wang, D. -S.; Kerker, M. *Phys. Rev. B* **1981**, *24*, 1777.

[30]Kirby, A. F.; Foster, D.; Richardson, F. S. *Chem. Phys. Lett.* **1983**, *95*, 507.

[31]Rikken, G. L. J. A., Kessener, Y. A. R. R. *Phys. Rev. Lett.* **1995**, *74*, 880.

[32]Schuurmans, F. J. P.; De Lang, D. T. N.; Wegdam, G. H.; Sprik, R.; Lagendijk, A. *Phys. Rev. Lett.* **1998**, *80*, 5077.

[33]Schuumans, F. J. P.; Lagendijk, A. *J. Appl. Phys.* **2000**, *113*, 3310.

[34]Maxwell-Garnett, J. C. *Philos. Trans. R. Soc. London* **1904**, *203*, 385.

[35]Khosravi, H.; Loudon, R. *Proc. R. Soc. Lond. A* **1991**, *433*, 337.

[36]Snoeks, E.; Lagendilk, A.; Polman, A. *Phys. Rev. Lett.* **1995**, *74*, 2459

[37]Chen, S.; Truax, L. A.; Sommers, J. M. *Chem. Mater.* **2000**, *12*, 3864.

[38]Gryczynski, I.; Malicka, J.; Holder, E.; DiCesare, N.; Lakowicz, J. R. *Chem. Phys. Lett.* **2003**, *372*, 409.

[39]Huang, T.; Murray, R. W. *Langmuir* **2002**, *18*, 7077.

Summary

In this thesis, the author has described his two investigations concerning novel characteristics of metal nanoparticles. The emphasis was put on the property that has not been achieved but has been predicted.

In Chapter 2, new protocol was described for the preparation of carbon thin films containing metal nanoparticles. In the present strategy, polyacrylonitrile (PAN), which is used industrially for the production of carbon fiber, were used as the precursor of carbon thin films. The starting materials were prepared by the successive evaporation of PAN and metal. IR measurements revealed that the vacuum evaporation of PAN had caused several structural changes; dominantly the decomposition of nitrile group and the consequent formation of heterocyclic structures. The following heat-treatment induced further structural changes of PAN layer above 200 ℃, and finally amorphous carbon thin films were obtained by the heat-treatment above 400 ℃. Along with the decomposition of PAN layer, heat-treatment also induced the penetration of metal nanoparticles into PAN layer, which was revealed by XPS depth profiles. The temperature at which the metal nanoparticle dispersed was 200 ℃ and was found to be synchronized with the temperature that the structural change of PAN was induced. These results suggest that the structural changes of PAN layer promoted the penetration of metal nanoparticles, presumably due to the activation of molecular motion that would offer the mobility for the embedded nanoparticles, similar to RAD process that is suggested by Deki's group. After all, the process for the preparation of amorphous carbon thin films (~ 100 nm thickness) homogeneously dispersing metal nanoparticles with a diameter below 10 nm has been established, and further control of the composition of the starting material and the heating condition would offer the possibility of obtain various kinds of nano-architectures consisting of metal nanoparticles and carbon thin films.

In Chapter 3, crystal structure of gold/cobalt alloy nanoparticles embedded in carbon thin films were examined by using of XPS, TEM and SAED analysis. The sample preparation was conducted roughly according to the way mentioned in Chapter 2, excepting that gold/cobalt alloy nanoparticles were obtained by simultaneous vacuum evaporation. Disordered solid solution was already formed in the as-deposited nanoparticles, although they were in thermodynamically metastable state, and the monometallic gold or cobalt nanoparticles were not observed in the detection limit in the present system. The crystal structure of as-deposited gold/cobalt alloy nanoparticles was face-centered-cubic for any composition examined in the present study; Au/Co=10/0, 80/20, 50/50, and 20/80. SAED analysis also provided the lattice parameter of these alloy nanoparticles, and the lattice parameter decreased with the increase in the cobalt atomic content, suggesting the substitution of smaller cobalt atoms for gold lattice sites. Nonetheless, the

lattice parameter was smaller that the expected value based on Vegard's rule, especially for the sample with higher cobalt content. On the other hand, heat-treatment induced gradual changes in the lattice parameters, and finally they reached the expected value by the heat-treatment at 600 ℃. In addition, ordered alloy with $L1_0$ or $L1_2$ structure also formed by the heat-treatment at 600 ℃. These results suggest that the co-evaporation of gold and cobalt has yielded thermodynamically metastable disordered solid-solution, and the following heat-treatment induced structural relaxation and finally led to the formation of thermodynamically stable alloy of both disordered and ordered crystal structures. All these alloy structures are not observed in the bulk phase diagrams, and the present study has demonstrated experimentally the modification of phase diagram for nanoscopic materials, which had theoretically been predicted.

In Chapter 4, the electron transport properties of gold/cobalt alloy nanoparticles prepared in Chapter 3 were explored. The most prominent aspect in this chapter is that gold/cobalt alloy nanoparticles exhibited spin-dependent tunneling behavior (i.e., TMR) even at room temperature. Although alloy nanoparticles with the atomic ratio of Au/Co=80/20 did not exhibit any dependence of magnetic field on the tunneling probability, increasing cobalt content resulted in the appearance of significant TMR effect. The present study revealed that the gold/cobalt alloy nanoparticles with Au/Co=20/80 atomic composition were capable of demonstrating the 80 % of TMR value even at room temperature.

In Chapter 5, the importance of the aggregation effect for an effective surface-enhanced fluorescence (SEF) was proven for the first time in solution phase, which has long been known in the field of surface-enhanced Raman scattering (SERS). This chapter started with the preparation and characterization of DMF-soluble spherical and rod-shaped silver nanoparticles. When the silver nanoparticles were added into Eu(dinic) complex solution, where dinic is dinicotinic acid, nanoparticle aggregates formed immediately, in which Eu(dinic) complexes behaved as linker molecules. Along with the formation of nanoparticle aggregates, the enhancement in the fluorescent intensity of Eu(dinic) was observed. To examine the effect of aggregates formation, Eu(DBM), where DBM is dibenzoylmethane, was used in place of Eu(dinic). Optical absorption spectrum revealed that the mixing of Eu(DBM) and silver nanoparticle did not result in the formation of aggregates. And in this case, fluorescence of Eu(DBM) was not enhanced, and only quenching function of silver nanoparticles appeared. Based on these results, the present study demonstrates that the effectiveness of aggregate formation and the consequent incorporation of the target molecules into the aggregates is not limited into SERS and is sufficiently valid for SEF.

List of Publications

[1] Preparation and Characterization of Metal Nanoparticles Dispersed in Polyacrylonitrile Thin Film

S. Deki, H. Nabika, K. Akamatsu, M. Mizuhata, A. Kajinami
Scripta Materialia **2001**, *44*, 1879.

[2] Fabrication and Characterization of PAN-Derived Carbon Thin Films Containing Au Nanoparticles

S. Deki, H. Nabika, K. Akamatsu, M. Mizuhata, A. Kajinami, S. Tomita, M. Fujii, S. Hayashi
Thin Solid Films **2002**, *408*, 59.

[3] Microstructure and Electron Transport Properties of Au_xCo_{1-x} Nano-Alloys Embedded in Polyacrylonitrile Thin Films

H. Nabika, K. Akamatsu, M. Mizuhata, A. Kajinami, S. Deki
Journal of Materials Chemistry **2002**, *12*, 2408.

[4] Preparation and Characterization of Au/Co Nano-Alloys

H. Nabika, M. Mizuhata, A. Kajinami, S. Deki, K. Akamatsu
Journal of Electroanalytical Chemistry **2003**, *559*, 99.

[5] Influence of Silver Nanoparticles on the Luninescent Properties of Europium Complex

H. Nabika, S. Deki
Trasactions of Materials Research Society of Japan **2003**, *28*, 907-910.

[6] Enhancing and Quenching Functions of Silver Nanoparticles on the Luminescent Properties of Europium Complex in the Solution Phase

H. Nabika, S. Deki
Journal of Physical Chemistry B **2003**, *107*, 9161.

[7] Surface-Enhanced Luminescence from Eu^{3+} Complex Nearby Ag Colloids

H. Nabika, S. Deki
European Physical Journal D **2003**, *24*, 369.

Acknowledgments

I would like to express my sincere gratitude to Professor Shigehito Deki for his continuous encouragement and discussions throughout this study.

I also would like to express deep acknowledgement to Dr. Kensuke Akamatsu (Konan University), Research Associate Akihiko Kajinami, and Dr. Minoru Mizuhata for their valuable discussions and helpful suggestions. I am also grateful to Dr. Hiroshi Yanagimoto (Mitsuboshi Belting Ltd.) for his precious comments, and to Dr. Satoshi Tomita (Riken) for his help and discussion on Raman measurement.

I am thankful to Dr. Koichi Sayo, Mr. Atsushi Yamada, Mr. Toshiyuki Fujita, Mr. Yoshinori Hatakenaka, Mr. Shodo Takei, Ms. Kinue Inoue, Mr. Nobuo Tsuboi, Mr. Shinjiro Noma, Mr. Shogo Hirai, Mr. Kentaro Kuratani, Mr. Sachihiko Iizuka, Mr. Takeshi Kawamura, Mr. Takashi Futaba, Mr. Shinsuke Tsubouchi, Mr. Yoshiyuki Otsubo, Mr. Hiroki Takahashi, Ms. Kayo Yoshida, and to all colleagues of the Laboratory of Applied Inorganic Chemistry, Department of Chemical Science and Engineering, Kobe University, for their indispensable comments and for giving me cheerful and lively life in the Lab.

I am indebted to Professor Franz Faupel, Dr. Vladimir Zaporojtchenko, Dr. Masahiro Iwamoto, Mr. Ulrich Schürmann, Mr. Jörn Kanzow, and colleagues of the Laboratory of Multicomponent Materials, Faculty of Engineering, Christian-Albrechts-University of Kiel, Germany, for their kindness and precious help during my stay at Kiel.

I wish to express my thanks to Professor Kei Murakoshi, Dr. Manabu Kiguchi, and colleagues of the Laboratory of Materials Chemistry, Graduate School of Science, Hokkaido University, for their support to get through this thesis.

Finally, I would like to express my greatest gratitude to my father, Tatsuro, to my mother, Nobuko, and to my brothers, Koji and Tomoyuki, for their hearty support and encouragement throughout these years, without which I would not be able to achieve this work.

August, 2004

Hideki Nabika